

# Biomedical flows at low Reynolds numbers

## Book of abstracts

**Conference Proceedings**

**Publication date:**

2011

**Permanent link:**

<https://doi.org/10.3929/ethz-a-006600372>

**Rights / license:**

[In Copyright - Non-Commercial Use Permitted](#)

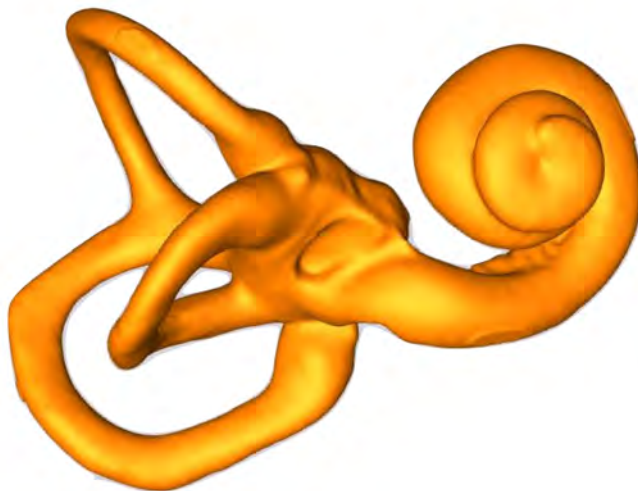
EUROMECH COLLOQUIUM 521

# Biomedical Flows at Low Reynolds Numbers

---

29–31 August 2011, ETH Zurich, Zurich, Switzerland

BOOK OF ABSTRACTS



Institute of Fluid Dynamics

**ETH**

Eidgenössische Technische Hochschule Zürich  
Swiss Federal Institute of Technology Zurich

---

# Contents

<b>General Information</b>	<b>1</b>
<b>Programme</b>	<b>5</b>
<b>Invited Talks</b>	<b>9</b>
MECHANICS OF BLOOD FLOW IN THE MICROCIRCULATION	
T. W. Secomb . . . . .	9
FULL DYNAMICS OF RED BLOOD CELLS IN A SHEAR FLOW: ROLLING, TUMBLING TANKTREADING	
A. Viallat, M. Socol, J. Dupire . . . . .	11
OPTIMALITY IN CELLULAR HYDRODYNAMICS	
E. Lauga . . . . .	15
MICROROBOTS: (ARTIFICIAL) LIFE AT LOW REYNOLDS NUMBERS	
B. J. Nelson . . . . .	16
INTERSTITIAL AND LYMPHATIC FLOW: MORE THAN JUST A DRAINAGE SYSTEM	
M. Swartz . . . . .	17
<b>Contributed Talks</b>	<b>19</b>
A MODEL OF TISSUE PERFUSION BASED ON HOMOGENIZATION OF DARCY FLOW IN DOUBLE-POROUS LAYERED MEDIUM	
E. Rohan, V. Lukes . . . . .	19
ERYTHROCYTE INFLUENCE ON BLOOD FLOW IN THE CEREBRAL VASCULATURE	
J. Reichold, A. Buck, D. Obrist, B. Weber, P. Jenny . . . . .	21
PARTICLES AND BLOOD CELLS AT BIFURCATIONS IN CAPILLARY NETWORKS	
G. Coupier, V. Doyeux, S. Peponas, M. Ismail, T. Podgorski . . . . .	23
FROM CEREBRAL BLOOD FLOW MODELING TO VASCULAR UNITS IN PRIMATE CORTEX	
R. Guibert, C. Fonta, F. Plouraboué . . . . .	25
FLOW AND TRANSPORT IN THE PLACENTA: HOMOGENIZING HAEMODYNAMICS IN A DISORDERED MEDIUM	
O.E. Jensen, I.L. Chernyavsky, W.R. Wan Abdullah, I.L. Dryden, A.A. Hill, L. Leach . . . . .	27
THREE-DIMENSIONAL EFFECTS IN THE FLOW OF BIOARTIFICIAL CAPSULES IN PORES	
D. Barthès-Biesel, X. Hu, A.-V. Salsac, T.-X. Chu . . . . .	29
A NOVEL COMPUTATIONAL APPROACH FOR MODELING HUMAN ERYTHROCYTES IN OSCILLATING SHEAR FLOW	
T. Klöppel, W. A. Wall . . . . .	31
	iii

FLUID DYNAMICS IN A MULTIPLE PARALLEL FLOW-CHAMBER FOR SHEAR-DEPENDENT CELLULAR ADHESION E. Bianchi, F. Boschetti, G. Dubini . . . . .	33
MICROBUBBLE DRIVEN MICROCIRCULATION INSIDE HUMAN CAPILLARIES AND ITS IMPACT ON THE ENDOTHELIUM W. Wiedemair, V. Kurtcuoglu, D. Poulikakos . . . . .	35
INSIGHT INTO THE DEVELOPING VITELLINE NETWORK WITH MICRO-PIV MEASUREMENTS A. Kloosterman, C. Poelma, B.P. Hierck, J. Westerweel . . . . .	37
NUMERICAL SIMULATIONS OF PUSHER AND PULLER SQUIRMER IN VISCOELASTIC FLUID L. Brandt, L. Zhu, E. Lauga . . . . .	39
NUMERICAL STUDY OF FREE MOVING CILIAR MICROORGANISMS AT LOW REYNOLDS NUMBERS R. A. Lambert, L. Brandt . . . . .	41
FLUID-STRUCTURE INTERACTION OF MICRO-SWIMMERS T. D. Johnson, D. Loghin, J. R. Blake, D. J. Smith . . . . .	43
BENDING MOMENT EFFICIENCY OF SPERM MOTILITY D. J. Smith, E. A. Gaffney, H. Gadêlha, J. Kirkman-Brown . . . . .	45
LEFT-RIGHT SYMMETRY BREAKING: VESICLE TRANSPORT DUE TO WHIRLING CILIA IN THE EMBRYONIC NODE A. A. Smith, T. D. Johnson, D. J. Smith, J. R. Blake . . . . .	47
BACTERIA-INSPIRED MICROROBOTS FOR NON-CONTACT MANIPULATION K. E. Peyer, L. Zhang, B. J. Nelson . . . . .	49
EXPERIMENTAL INVESTIGATION OF THE FLOW INDUCED BY ARTIFICIAL CILIA J. Hussong, N. Schorr, J. Belardi, O. Prucker, J. Rûhe, J. Westerweel . . . . .	51
LOW-REYNOLDS-NUMBER FLOW BETWEEN TWO VESSELS WITH A SHUNT BETWEEN THEM A. Setchi, J. Mestel, J. Siggers, K. Parker . . . . .	53
MATHEMATICAL MODELLING OF HIGH-FREQUENCY FLOW IN CURVED, COMPLIANT ARTERIES S. Payvandi, J. H. Siggers, K. H. Parker . . . . .	55
FLUID MOTION FOR MICRO-GRAVITY SIMULATIONS IN A RANDOM POSITIONING MACHINE C. A. D. Leguy, R. Delfos , M.J.B.M. Pourquie, C. Poelma , J. Vreeburg, J. Krooneman, J. Westerweel, J.J.W.A. van Loon . . . . .	57
A UNIFIED NUMERICAL METHOD FOR FLUID-STRUCTURE INTERACTION APPLIED TO HUMAN COCHLEAR MECHANICS F. Böhnke, D. Köster . . . . .	59
VISCOUS AND NONLINEAR PHENOMENA IN THE COCHLEA E. Edom, D. Obrist, L. Kleiser . . . . .	61
COMPARISON OF THE FLOW PATTERNS IN HEALTHY AND PATHOLOGICAL VESTIBULAR SYSTEMS F. Boselli, D. Obrist, L. Kleiser . . . . .	63
DYNAMICS OF THE VITREOUS HUMOUR AND STRESS ON THE RETINA GENERATED DURING EYE ROTATIONS J. Meskauskas, R. Repetto, J.H. Siggers . . . . .	65
EXPERIMENTAL INVESTIGATION OF PARTICLE-LADEN FLOW IN AN IN-VITRO MODEL OF A SINGLE ALVEOLU D. Borer, T. Rösigen . . . . .	67
UNSTEADY SURFACTANT-LADEN LIQUID PLUG PROPAGATION: A MODEL FOR SURFACTANT REPLACEMENT THERAPY U. Olgac, M. Muradoglu . . . . .	69

---

EFFECTS OF SURFACTANT ON MOTION OF A LARGE BUBBLE IN A CAPIL- LARY TUBE M. Muradoglu, G. Gursel, U. Olgac . . . . .	71
MULTISCALE ANALYSIS OF FLUID FLOW IN LYMPHATIC CAPILLARIES T. Roose, M. Swartz . . . . .	73
BLOOD FLOW AND DEFORMATION OF LIVER TISSUE DURING PORTAL HY- PERTENSION J. Siggers, A. Bonfiglio, K. Leunchavaphongse, R. Repetto . . . . .	75
MATHEMATICAL MODEL OF BLOOD AND INTERSTITIAL FLUID FLOW IN THE LIVER K. Leunchavaphongse, J. Siggers, R. Repetto . . . . .	77
<b>INDEX</b>	<b>79</b>

*CONTENTS*

---

# General Information

## Scientific Scope and Topics

The study of biological flows enjoys a rapidly increasing interest. Research on biomedical flow systems and animal locomotion has reached a high level of maturity and has become a well established topic within the larger field of fluid mechanics. While there are many research groups studying flow problems at moderate to large Reynolds numbers (e.g. cardiovascular fluid mechanics), academic research on biomedical flows at low Reynolds numbers is less commonly found.

This fact is unfortunate since low-Reynolds-number flows are highly relevant to medicine and biology in general, and to physiology in particular. In collaboration with medical scientists and biologists, the fluid dynamics community is able to make substantial contributions to these fields. Typical low-Reynolds-number biomedical and biological flow systems may include

- flow in the lower airways
- cerebrospinal fluid flow
- microcirculation and red blood cell transport
- flows in the eye and the inner ear (balance sense, hearing)
- biomedical microdevices (e.g. filters, pumps, drainages, microrobots)
- propulsion and collective behaviour of microorganisms.

This Colloquium brings together researchers from groups throughout Europe working on low-Reynolds-number biomedical and biological flows including theoretical, experimental and computational contributions.

## Organizing Committee

Prof. Leonhard Kleiser	ETH Zürich	Chair
Prof. Timothy Pedley	University of Cambridge	Co-chair
Prof. Dominique Barthès-Biesel	Université de Compiègne	
Prof. Thomas Rösgen	ETH Zürich	
Prof. Patrick Jenny	ETH Zürich	
Dr. Dominik Obrist	ETH Zürich	Scientific Secretary



## Scientific Programme

The EUROMECH Colloquium 521 on "Biomedical Flows at Low Reynolds Numbers" begins on Monday morning, August 29, 2011, and ends on Wednesday afternoon, August 31, 2011. The scientific programme consists of 30 contributed papers, and 5 invited lectures by

- Timothy W. Secomb (University of Arizona): Mechanics of blood flow in the microcirculation
- Annie Viallat (INSERM Marseille): Full dynamics of red blood cells in a shear flow: rolling, tumbling tanktreading
- Eric Lauga (UC San Diego): Optimality in cellular hydrodynamics
- Bradley J. Nelson (ETH Zurich): Microrobots: (Artificial) Life at low Reynolds numbers
- Melody Swartz (EPF Lausanne): Interstitial and lymphatic flow: More than just a drainage system

The contributed presentations are limited to 20 minutes (plus 5 minutes for questions). Presenters are expected to bring their own laptop. Beamer and pointers are available. All scientific presentations take place in the **lecture hall ML E12**.

## Sponsoring

The organizers would like to thank the sponsors of this Colloquium:

- EUROMECH — European Mechanics Society ([www.euromech.org](http://www.euromech.org))
- ERCOFTAC — European Research Community on Flow, Turbulence and Combustion ([www.ercoftac.org](http://www.ercoftac.org))
- Institute of Fluid Dynamics, ETH Zürich ([www.ifd.mavt.ethz.ch](http://www.ifd.mavt.ethz.ch))

## Venue

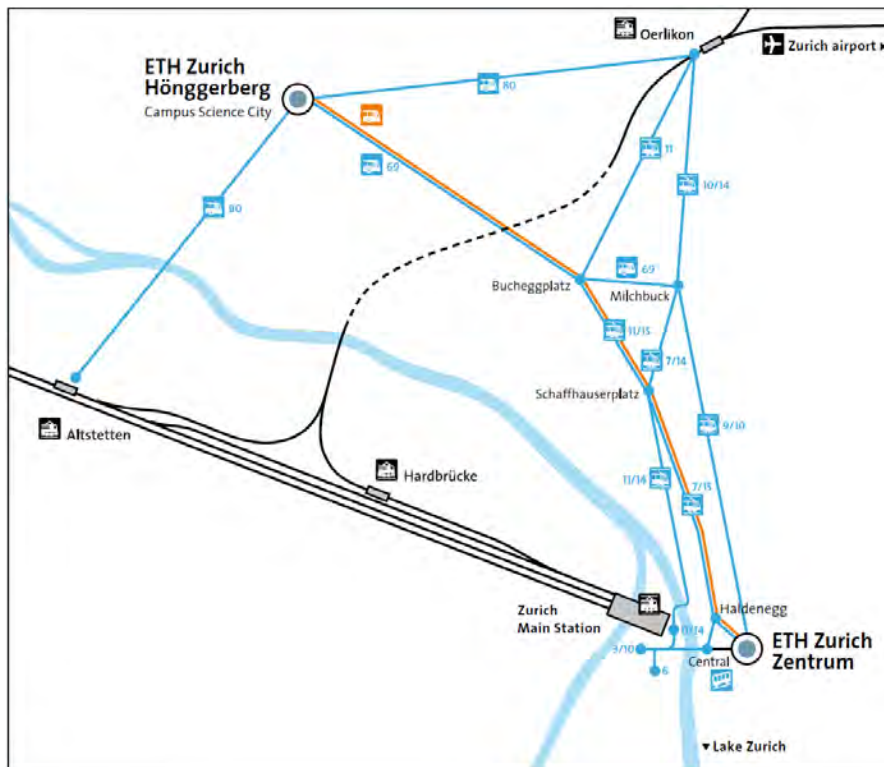
The **lecture hall ML E12** is located on the main floor of the ML building ("Maschinenlabor") on the central campus of ETHZ ("ETH Zürich Zentrum", see map on page 4). The ML building is next to the tram stations of the tram lines 6, 9, and 10, just north of the ETH main building (HG) across Tannenstrasse.





The **registration desk** is next to the lecture hall in the room **ML E13**. During the Colloquium this room will be open to all participants for individual work (wireless internet connection available).

The **coffee breaks** as well as the **Farewell Apéro** take place in the **lobby of the ML building** (just in front of the lecture hall).

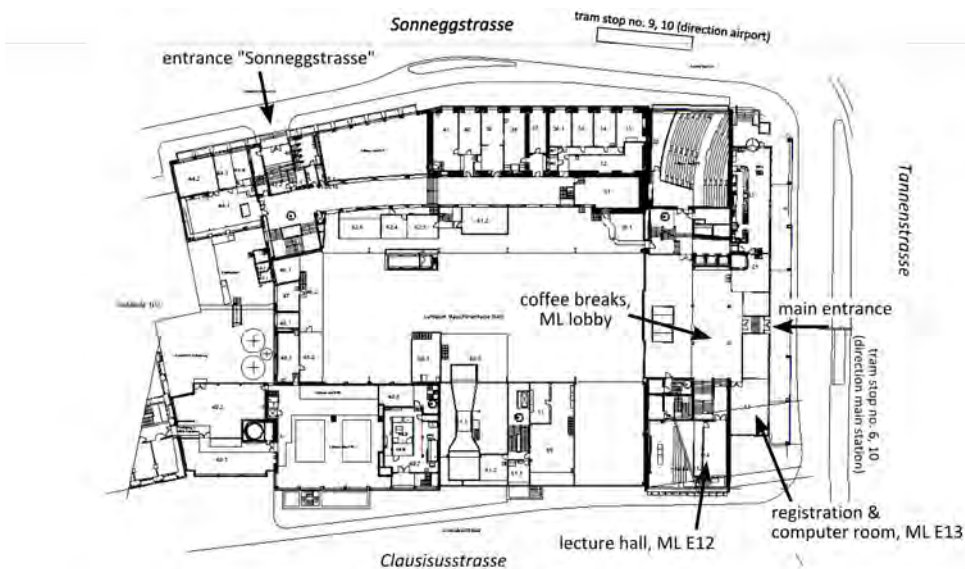
The *Conference Dinner* (Tuesday, 19:00 – 23:00) takes place in the "*Dozentenfoyer*" which is located on the top floor of the main building of ETHZ ("*Hauptgebäude*", HG, J-floor).

## Public Transport to ETH Zurich

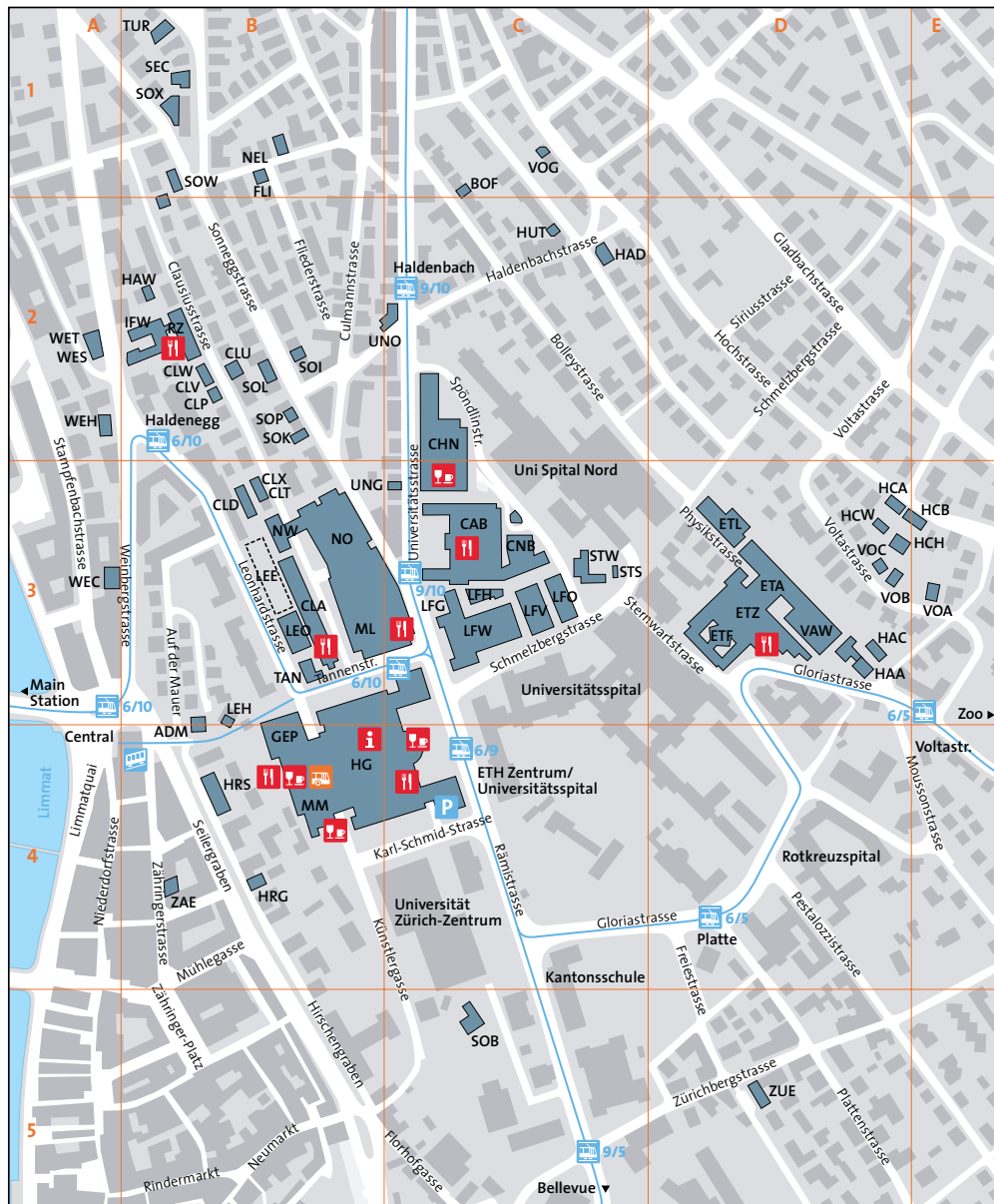








-  Railway station
-  Tram
-  Bus
-  Cable car "Polybahn"

## Floor Plan ML-building



## ETH Zurich – Campus Zentrum



- |   |   |
|---|---|
|  Tram stop                       |  Canteen                                   |
|  Cable Car "Polybahn"            |  Cafeteria                                 |
|  ETH-shuttle "Science City Link" |  Information desk (phone +41 44 632 25 50) |

Publisher: ETH Zürich, Corporate Communications, May 2011  
 Map: Institute of Cartography of ETH Zurich, edited by Immobilien,  
 Stab Portfoliomanagement, and Corporate Communications

# Programme

## Overview

	Mon, 29.8.11	Tue, 30.8.11	Wed, 31.8.11
8:00 - 8:45	Registration		
8:45 - 9:00	Welcome		
9:00 - 9:25	Invited Lecture	Invited Lecture	Session 3.1
9:25 - 9:50			
9:50 - 10:15	Session 1.1	Session 2.1	
10:15 - 10:40			
10:40 - 11:10	Coffee Break	Coffee Break	Coffee Break
11:10 - 11:35	Session 1.2	Session 2.2	Session 3.2
11:35 - 12:00			
12:00 - 12:25			
12:30 - 13:40	Lunch	Lunch	Lunch
13:40 - 14:05			Invited Lecture
14:05 - 14:30			
14:30 - 14:55	Invited Lecture	Invited Lecture	Session 3.3
14:55 - 15:20			
15:20 - 15:45	Session 1.3	Session 2.3	
15:45 - 16:10			15:45 - 15:50: Closing
16:10 - 16:40	Coffee Break	Coffee Break	15:50 - 16:30: Farewell Apéro
16:40 - 17:05	Session 1.4	Session 2.4	
17:05 - 17:30			
17:30 - 17:55			
	18:15-20:00 Welcome Reception		
		19:00 - 23:00 Conference Dinner	

---

## Detailed Programme

### Monday, 29 August 2011

---



---

8:00 – 8:45	<i>Registration</i>
8:45 – 8:50	<i>Welcome by Prof. L. Kleiser, Chair of EC521</i>
8:50 – 9:00	<i>Welcome address by Prof. Ch. Hierold, Deputy Head of the Department of Mechanical and Process Engineering</i>
9:00 – 9:50	<b>MECHANICS OF BLOOD FLOW IN THE MICROCIRCULATION</b> , <i>Timothy W. Secomb</i>
9:50 – 10:15	A MODEL OF TISSUE PERFUSION BASED ON HOMOGENIZATION OF DARCY FLOW IN DOUBLE-POROUS LAYERED MEDIUM, <i>E. Rohan, V. Lukes</i>
10:15 – 10:40	ERYTHROCYTE INFLUENCE ON BLOOD FLOW IN THE CEREBRAL VASCULATURE, <i>J. Reichold, A. Buck, D. Obrist, B. Weber, P. Jenny</i>
10:40 – 11:10	<i>Coffee Break</i>
11:10 – 11:35	PARTICLES AND BLOOD CELLS AT BIFURCATIONS IN CAPILLARY NETWORKS, <i>G. Couplier, V. Doyeux, S. Peponas, M. Ismail, T. Podgorski</i>
11:35 – 12:00	FROM CEREBRAL BLOOD FLOW MODELING TO VASCULAR UNITS IN PRIMATE CORTEX, <i>R. Guibert, C. Fonta, F. Plouraboué</i>
12:00 – 12:25	FLOW AND TRANSPORT IN THE PLACENTA: HOMOGENIZING HAEMODYNAMICS IN A DISORDERED MEDIUM, <i>O.E. Jensen, I.L. Chernyavsky, W.R. Wan Abdullah, I.L. Dryden, A.A. Hill, L. Leach</i>
12:30 – 14:30	<i>Lunch</i>
14:30 – 15:20	<b>FULL DYNAMICS OF RED BLOOD CELLS IN A SHEAR FLOW: ROLLING, TUMBLING TANKTREADING</b> , <i>Annie Viallat</i>
15:20 – 15:45	THREE-DIMENSIONAL EFFECTS IN THE FLOW OF BIOARTIFICIAL CAPSULES IN PORES, <i>D. Barthès-Biesel, X. Hu, A.-V. Salsac, T.-X. Chu</i>
15:45 – 16:10	A NOVEL COMPUTATIONAL APPROACH FOR MODELING HUMAN ERYTHROCYTES IN OSCILLATING SHEAR FLOW, <i>T. Klöppel, W. A. Wall</i>
16:10 – 16:40	<i>Coffee Break</i>
16:40 – 17:05	FLUID DYNAMICS IN A MULTIPLE PARALLEL FLOW-CHAMBER FOR SHEAR-DEPENDENT CELLULAR ADHESION, <i>E. Bianchi, F. Boschetti, G. Dubini</i>
17:05 – 17:30	MICROBUBBLE DRIVEN MICROCIRCULATION INSIDE HUMAN CAPILLARIES AND ITS IMPACT ON THE ENDOTHELIUM, <i>W. Wiedemair, V. Kurtcuoglu, D. Poulidakos</i>
17:30 – 17:55	INSIGHT INTO THE DEVELOPING VITELLINE NETWORK WITH MICROPIV MEASUREMENTS, <i>A. Kloosterman, C. Poelma, B.P. Hierck, J. Westerweel</i>
18:15 – 20:00	<i>Welcome Reception</i>

---



---

---

**Tuesday, 30 August 2011**


---

9:00 - 9:50	<b>OPTIMALITY IN CELLULAR HYDRODYNAMICS</b> , <i>Eric Lauga</i>
9:50 - 10:15	NUMERICAL SIMULATIONS OF PUSHER AND PULLER SQUIRMER IN VISCOELASTIC FLUID, <i>L. Brandt, L. Zhu, E. Lauga</i>
10:15 - 10:40	NUMERICAL STUDY OF FREE MOVING CILIAR MICROORGANISMS AT LOW REYNOLDS NUMBERS, <i>R. A. Lambert, L. Brandt</i>
10:40 - 11:10	<i>Coffee Break</i>
11:10 - 11:35	FLUID-STRUCTURE INTERACTION OF MICRO-SWIMMERS, <i>T. D. Johnson, D. Loghin, J. R. Blake, D. J. Smith</i>
11:35 - 12:00	BENDING MOMENT EFFICIENCY OF SPERM MOTILITY, <i>D. J. Smith, E. A. Gaffney, H. Gadêlha, J. Kirkman-Brown</i>
12:00 - 12:25	LEFT-RIGHT SYMMETRY BREAKING: VESICLE TRANSPORT DUE TO WHIRLING CILIA IN THE EMBRYONIC NODE, <i>A. A. Smith, T. D. Johnson, D. J. Smith, J. R. Blake</i>
12:30 - 14:30	<i>Lunch</i>
14:30 - 15:20	<b>MICROROBOTS: (ARTIFICIAL) LIFE AT LOW REYNOLDS NUMBERS</b> , <i>Bradley J. Nelson</i>
15:20 - 15:45	BACTERIA-INSPIRED MICROROBOTS FOR NON-CONTACT MANIPULATION, <i>K. E. Peyer, L. Zhang, B. J. Nelson</i>
15:45 - 16:10	EXPERIMENTAL INVESTIGATION OF THE FLOW INDUCED BY ARTIFICIAL CILIA, <i>J. Hussong, N. Schorr, J. Belardi, O. Prucker, J. Rûhe, J. Westerweel</i>
16:10 - 16:40	<i>Coffee Break</i>
16:40 - 17:05	LOW-REYNOLDS-NUMBER FLOW BETWEEN TWO VESSELS WITH A SHUNT BETWEEN THEM, <i>A. Setchi, J. Mestel, J. Siggers, K. Parker</i>
17:05 - 17:30	MATHEMATICAL MODELLING OF HIGH-FREQUENCY FLOW IN CURVED, COMPLIANT ARTERIES, <i>S. Payvandi, J. H. Siggers, K. H. Parker</i>
17:30 - 17:55	FLUID MOTION FOR MICRO-GRAVITY SIMULATIONS IN A RANDOM POSITIONING MACHINE, <i>C. A. D. Leguy, R. Delfos, M.J.B.M. Pourquie, C. Poelma, J. Vreeburg, J. Krooneman, J. Westerweel, J.J.W.A. van Loon</i>
19:30 - 23:30	<i>Conference Dinner</i>

---

**Wednesday, 31 August 2011**

---

---

9:00 - 9:25	A UNIFIED NUMERICAL METHOD FOR FLUID-STRUCTURE INTERACTION APPLIED TO HUMAN COCHLEAR MECHANICS, <i>F. Böhnke, D. Köster</i>
9:25 - 9:50	VISCOUS AND NONLINEAR PHENOMENA IN THE COCHLEA, <i>E. Edom, D. Obrist, L. Kleiser</i>
9:50 - 10:15	COMPARISON OF THE FLOW PATTERNS IN HEALTHY AND PATHOLOGICAL VESTIBULAR SYSTEMS, <i>F. Boselli, D. Obrist, L. Kleiser</i>
10:15 - 10:40	DYNAMICS OF THE VITREOUS HUMOUR AND STRESS ON THE RETINA GENERATED DURING EYE ROTATIONS, <i>J. Meskauskas, R. Repetto, J.H. Siggers</i>

---

10:40 - 11:10	<i>Coffee Break</i>
---------------	---------------------

---

11:10 - 11:35	EXPERIMENTAL INVESTIGATION OF PARTICLE-LADEN FLOW IN AN IN-VITRO MODEL OF A SINGLE ALVEOLUS, <i>D. Borer, T. Rösger</i>
11:35 - 12:00	UNSTEADY SURFACTANT-LADEN LIQUID PLUG PROPAGATION: A MODEL FOR SURFACTANT REPLACEMENT THERAPY, <i>U. Olgac, M. Muradoglu</i>
12:00 - 12:25	EFFECTS OF SURFACTANT ON MOTION OF A LARGE BUBBLE IN A CAPILLARY TUBE, <i>M. Muradoglu, G. Gursel, U. Olgac</i>

---

12:30 - 13:40	<i>Lunch</i>
---------------	--------------

---

13:40 - 14:30	<b>INTERSTITIAL AND LYMPHATIC FLOW: MORE THAN JUST A DRAINAGE SYSTEM</b> , <i>Melody Swartz</i>
---------------	---

---

14:30 - 14:55	MULTISCALE ANALYSIS OF FLUID FLOW IN LYMPHATIC CAPILLARIES, <i>T. Roose, M. Swartz</i>
14:55 - 15:20	MATHEMATICAL MODEL OF BLOOD AND INTERSTITIAL FLUID FLOW IN THE LIVER, <i>K. Leunchavaphongse, J. Siggers, R. Repetto</i>
15:20 - 15:45	BLOOD FLOW AND DEFORMATION OF LIVER TISSUE DURING PORTAL HYPERTENSION, <i>J. Siggers, A. Bonfiglio, K. Leunchavaphongse, R. Repetto</i>

---

15:45 - 15:50	<i>Closing</i>
---------------	----------------

---

15:50 - 16:30	<i>Farewell Apéro</i>
---------------	-----------------------

---

## MECHANICS OF BLOOD FLOW IN THE MICROCIRCULATION

Timothy W. Secomb<sup>1</sup>

<sup>1</sup>*Department of Physiology, University of Arizona, Tucson AZ 85724, USA*

The term ‘microcirculation’ refers to the terminal branches of the circulatory system, with diameters ranging from a few hundred  $\mu\text{m}$  down to a few  $\mu\text{m}$ . Blood is a concentrated suspension of cells, mainly red blood cells (RBCs), in plasma. The hematocrit (volume fraction of red blood cells) is normally 40% to 45%. The unstressed shape of a normal human RBC is a biconcave disc with a diameter of 8  $\mu\text{m}$  and a thickness of 2  $\mu\text{m}$ . The interior is a concentrated hemoglobin solution, which behaves as an incompressible viscous fluid. The cell membrane is viscoelastic, with low resistance to bending and in-plane shear deformations. As a consequence of these physical properties, RBCs are highly deformable, allowing blood to flow readily through microvessels despite being a concentrated suspension.

Resistance to flow in blood vessels has been studied since the time of Poiseuille in the mid nineteenth century. Flow resistance can be expressed in terms of the apparent viscosity, i.e., the viscosity of a Newtonian fluid that would result in the same flow rate for a given driving pressure. Observations in narrow glass tubes show a marked decrease in the apparent viscosity with decreasing diameter below 1000  $\mu\text{m}$ , a phenomenon known as the Fåhræus-Lindqvist effect. This reflects non-continuum behavior of blood near the vessel wall, leading to the formation of a cell-free or cell-depleted layer. A simple two-layer model, in which the RBCs are contained within a concentric cylindrical core region with relative diameter  $\lambda$  and with uniform viscosity  $\mu_{core}$ , and the surrounding cell-free annular wall layer has viscosity  $\mu_p$ , predicts apparent viscosity as  $\mu_{app} = \mu_p / (1 - \lambda^4(1 - \mu_p/\mu_{core}))$ . Even a relatively narrow plasma layer causes a substantial reduction in apparent viscosity, because it decreases the viscosity in the region near the wall where viscous energy dissipation would otherwise be concentrated.

In capillaries with diameters up to about 8  $\mu\text{m}$ , RBCs frequently flow in single file. In such vessels, RBCs are compressed into narrow bullet-like shapes, and their mechanics can be analyzed by assuming that the RBC has axisymmetric geometry. A further simplification is the use of lubrication theory to describe the motion of the suspending fluid in the layer between the cell and the vessel wall. Under these assumptions, the fluid-solid interaction problem can be expressed as a coupled nonlinear system of ordinary differential equations, which can be solved numerically to predict cell shapes and apparent viscosity [10]. Predictions of this theory agree well with experimental measurements of apparent viscosity in capillary-sized glass tubes.

For tube diameters above 30  $\mu\text{m}$ , a good fit to experimental results is obtained from the two-layer model, by assuming a cell-free layer width of 1.8  $\mu\text{m}$  and  $\mu_{core}/\mu_p = 3.3$  [8]. The width of the cell-depleted layer is determined by two opposing effects. Individual flexible particles tend to migrate away from solid boundaries, but particle-particle interactions result in ‘shear-induced diffusion’ down the concentration gradient toward the wall [9]. For blood flow in tubes with diameters between 8 and 30  $\mu\text{m}$ , continuum models are not appropriate. Theoretical models must consider multiple interacting RBCs. This is a challenging computational problem, particularly if fully three-dimensional geometries are considered. Increasing computing power in recent years has led to an upsurge of interest in this area [2,3,4,5].

We developed a two-dimensional approach for simulating the motion and interaction of RBCs in narrow channels [1,11]. The cross-sectional shape of each RBC is represented by a set of viscoelastic elements on the perimeter and in the interior of the cell. The internal elements represent the internal viscosity of the cell and the cell membrane’s viscous resistance to three-dimensional out-of-plane deformations. Membrane bending elasticity is represented by an elastic resistance at the nodes. The strong resistance of RBCs to area change is represented in the model by assigning an internal pressure that depends on the cell area. The suspending medium is a viscous incompressible fluid. A finite element method was used to solve the resulting system of coupled equations. In order to calibrate the model, we compared predictions with experimental



data on the cyclic ‘tank-treading’ motion of the membrane around the cell interior that is observed when a RBC is placed in simple shear flow of a high-viscosity fluid. In this motion, a band of membrane around the cell is alternately lengthened and shortened. This continuous deformation results in viscous energy dissipation in the membrane. The internal viscous elements represent resistance to this motion. With suitably chosen parameters, this model closely approximates tank-treading frequencies and cell elongations observed in high-viscosity shear flow.

The model was used to simulate the motion of RBCs in microvessels [11]. When placed in off-axis positions, the cells assume asymmetric shapes and migrate towards the center-line. Trajectories and shapes of RBCs computed by this method agree well with observations in living tissues. This method can also be used to study the motion of RBCs in diverging bifurcations. Observations of such bifurcations show the phenomenon of non-uniform hematocrit partition or ‘phase separation’ [6]. Typically, the branch with higher flow rate receives a larger hematocrit, due to the presence of a cell-free or cell-depleted layer near the wall. A branch with low flow rate tends to receive fluid mainly from this layer. The model was used to analyze RBC motion and deformation in capillary bifurcations, and to predict the migration of RBCs across streamlines of the underlying flow [1]. The motion of a single cell, initially positioned near the wall of a flowing parallel-sided channel, was studied. In the first phase of the motion, the initially circular cell develops an asymmetric teardrop shape. As a result of this asymmetry in shape, the cell migrates away from the wall towards the center-line. The subsequent motion involves a complex combination of cell deformation, tank-treading, and tumbling.

Experimental studies of blood flow in microvascular networks reveal major differences from predictions based on *in vitro* observations of apparent viscosity [7]. The main cause of these differences is the presence of a relatively thick layer, about 1  $\mu\text{m}$  wide, of macromolecules bound to the endothelial cells lining microvessel walls. This endothelial surface layer substantially increases flow resistance in microvessels, reduces hematocrit, and affects interactions of blood cells with vessel walls. With regard to RBC motion, this layer may play an important role by shielding RBCs from large stresses generated when the cells traverse irregular microvessel geometries during multiple passages through the microcirculation. Using our two-dimensional model, we examined the effect of such a layer on transverse migration of RBCs. As the layer is made more permeable to plasma flow, the localized forces acting on edge of the cell nearest to the wall are decreased, resulting in less shape change and slower migration. These results suggest that the endothelial surface layer may slow the development of a cell-free or cell-depleted layer when blood enters a microvessel *in vivo*.

## References

- [1] Barber J.O., Alberding J.P., Restrepo J.M., Secomb T.W. Simulated two-dimensional red blood cell motion, deformation, and partitioning in microvessel bifurcations. *Ann Biomed Eng* **36**: 1690-1698, 2008.
- [2] Doddi S.K., Bagchi P. Three-dimensional computational modeling of multiple deformable cells flowing in microvessels. *Physical Review E* **79**, 046318, 2009.
- [3] Dupin M.M., Halliday I., Care C.M., Alboul L., Munn L.L. Modeling the flow of dense suspensions of deformable particles in three dimensions. *Physical Review E* **75**, 066707, 2007.
- [4] McWhirter J.L., Noguchi H., Gompper G. Flow-induced clustering and alignment of vesicles and red blood cells in microcapillaries. *Proc. Natl. Acad. Sci. USA* **106**, 6039-6043, 2009.
- [5] Pivkin I.V., Karniadakis G.E. Accurate coarse-grained modeling of red blood cells. *Physical Review Letters* **101**, 118105, 2008.
- [6] Pries A.R., Secomb T.W., Gaehtgens P. Biophysical aspects of blood flow in the microvasculature. *Cardiovasc Res* **32**: 654-667, 1996.
- [7] Pries A.R., Secomb T.W., Gessner T., Sperandio M.B., Gross J.F., Gaehtgens P. Resistance to blood flow in microvessels in vivo. *Circ Res* **75**: 904-915, 1994.
- [8] Secomb T.W. Mechanics of blood flow in the microcirculation. *Symp Soc Exp Biol* **49**: 305-321, 1995.
- [9] Secomb T.W. Mechanics of red blood cells and blood flow in narrow tubes. In: *Hydrodynamics of Capsules and Cells*, edited by Pozrikidis C. Boca Raton, Florida, Chapman & Hall/CRC, p. 163-196, 2003.
- [10] Secomb T.W., Skalak R., Ozkaya N., Gross J.F. Flow of axisymmetric red blood cells in narrow capillaries. *Journal of Fluid Mechanics* **163**: 405-423, 1986.
- [11] Secomb T.W., Styp-Rekowska B., Pries A.R. Two-dimensional simulation of red blood cell deformation and lateral migration in microvessels. *Ann Biomed Eng* **35**: 755-765, 2007.

***FULL DYNAMICS OF RED BLOOD CELLS IN A SHEAR FLOW:  
ROLLING, TUMBLING TANKTREADING***

*Annie Viallat, Marius Socol & Jules Dupire*

*Lab. Adhesion and Inflammation, INSERM UMR 600, CNRS UMR 62 12, Aix  
Marseille University, Luminy, 13288 Marseille, France*

**INTRODUCTION**

The shape and the mechanical properties of red blood cells (RBCs) are key factors for their transport in the vasculature, from capillary networks to arteries. However, even under a simple shear flow, the cell mechanical response to the hydrodynamic constraint generates complex RBC motions that are still not well understood. The structure of the RBC is one of the simplest among cells but it nevertheless involves several mechanical parameters: viscosity of the internal fluid that governs cell fluidization, membrane shear and bending elasticities, membrane incompressibility that help to preserve a smooth cell shape. Moreover, the non-spherical shape of the cell combined with shear elasticity generates a shape memory effect, which induces an energy threshold for membrane flow. Depending on the amplitude of the external constraint, the dynamics of the cell is controlled by one or a combination of these parameters and its behavior may then be similar to that of a solid, of a fluid or of a complex viscoelastic capsule. Pioneering studies [1, 2, 3] revealed different regimes of motions: flipping, tumbling (T) (often referred as a particular case of flipping when the cell axis of symmetry rotates in the shear plane) and tanktreading with a stationary orientation (TT). They provided data, often qualitative, on the variations of the cell orbit and on the dependence of the (T)-(TT) transition to the viscosity of the suspending fluid and to the shear rate. For many years, modeling accounted only for viscosity and described the RBC as a fluid ellipsoid [4]. It allowed to qualitatively predict the existence of (T) and (TT) but not the shear-rate dependence nor any orbit variation. More recently, new features were found like cell shape memory [5], swinging (S) motion superimposed to (TT), intermittent motion [6, 7] and chaotic motion in a time-periodic shear flow [8]. These motions were semi-quantitatively described by including membrane viscosity, elasticity and shape memory in an ellipsoid model. A large number of numerical approaches were then developed [9], which accounted for viscosity, elasticity, shape memory, bending and allowed cell deformation. These approaches qualitatively retrieve (T), (TT) and (S), but they still ignore orbit variations, are controversial on intermittency and predict strong cell deformations at the (T)-(TT) transition and during (TT) that are not seen experimentally. A full quantitative understanding of RBCs motion in shear flow is still obviously experimentally and theoretically lacking.

Here, we carefully study the full dynamics of individual red blood cells in a shear flow for two viscosities of the suspending fluid and various shear rates. RBCs are observed both parallel and perpendicularly to the shear plane and the cell membrane is marked to follow its movement. We show that RBCs do not flip stably upon increasing the shear rate. We measure the progressive rotation of their axis of symmetry and the final cell rolling and spinning in the shear plane. This behaviour is due to the elastic contribution of the membrane. We show that the rolling - (TT) transition and the (TT) - flipping transition observed upon increasing and decreasing the shear rate respectively display a strong hysteresis and different mechanisms. Cell deformation is small: RBC shape remains biconcave during both (T) and (TT), contrarily to predictions of numerical simulations. This result suggests that the shape memory has a low energy barrier and that bending energy plays a significant role to maintain the biconcave cell shape.

**MATERIALS AND METHODS**

Direct observations of the cells are provided from side-view microscopic imaging in a vertical plane parallel to the shear plane [6] and from bottom view in an horizontal plane perpendicular to the shear plane. RBCs are diluted in a solution of dextran of concentration 9% w/w with PBS at 290 mOsm and pH=7.4 ( $M_w = 2 \cdot 10^6$  g/Mol,  $\eta_o = 34$  mPa.s or  $M_w = 10^5$  g/Mol,  $\eta_o =$

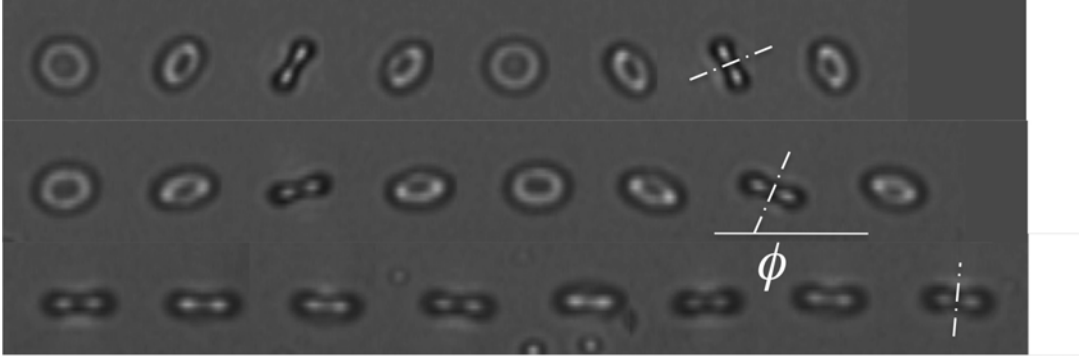


**Figure 1.** Tumbling to rolling: time sequence of the projection of a RBC in a plane perpendicular to the shear plane. The flow is from right to left. external viscosity= $10^{-2}$  Pa.s ; Top series:  $\dot{\gamma} = 2s^{-1}$ , middle series:  $\dot{\gamma} = 6s^{-1}$ , bottom series:  $\dot{\gamma} = 12s^{-1}$ .

10 mPa.s). RBCs are almost non-buoyant in the solution and can flow without sinking. Small carboxylated beads stuck to the cell membrane allow the observation of its movement.

## RESULTS

It is generally considered that the major parameter that determines the cell regime of motion is the ratio of the internal to external liquid viscosities. For a given cell shape there exists a threshold for the viscosity ratio above which the cell should always flip. Below this threshold, the cell is expected to flip at low shear rate and to swing and tanktread at high shear rate. The nature of the flipping motion (when a particle flips it may tanktread or not) and its stability are not experimentally known. The role of the second important mechanical parameter, the elastic energy, on flipping is also not well documented. Little is known on the mechanisms of the flipping- swinging and swinging-flipping transitions and on the cell deformation. Most studies have been limited to the particular case of tumbling.

### From flipping to rolling

We follow the movement of RBCs, which present various initial orientations with respect to the flow direction for two external solutions of viscosities equal to  $10^{-2}$  Pa.s and  $3.410^{-2}$  Pa.s respectively . We give a particular attention to the cells for which the angle  $\phi$  between their axis of symmetry measured when it lies in the plane of observation and the flow direction is initially less than  $10^\circ$  (tumbling motion). When the shear rate  $\dot{\gamma}$  slowly increases by step, the orbit of the cell changes,  $\phi$  increases and reaches a limiting value for each step value of the shear rate, as seen in Figure 1. The cell axis has a precession movement. Upon further  $\dot{\gamma}$ -increase, the cell lies in the shear plane and rolls ( $\phi = 90^\circ$ ). The deformation (elongation/compression) of the cell remains small (less than 10%). This result shows that flipping (and tumbling) is not a stable motion for RBCs upon increasing the shear rate and that the stable orbit of the cell depends on the shear rate. The origin of this phenomenon is studied by stiffening RBCs by incubation in a solution of glutaraldehyde (crosslinking of the proteins of the cell membrane). In this case, the tumbling motion is stable and the angle  $\phi$  never increases above  $40^\circ$ , even for the largest shear rates. Finite membrane elasticity promotes a rolling motion, while stiffening of the cell stabilizes a tumbling motion.

The role of the elastic contribution to the membrane motion is also explored. Clearly the membrane does not fully tanktread about the cell shape as seen by the observation of latex beads stuck on the membrane (Figure 2). The fit of the time variations of the cell inclination angle with respect to the flow direction,  $\theta$ , shows that for low shear stresses, the membrane does not move: the cell motion is very similar to that of a rigid particle. When the shear stress increases,

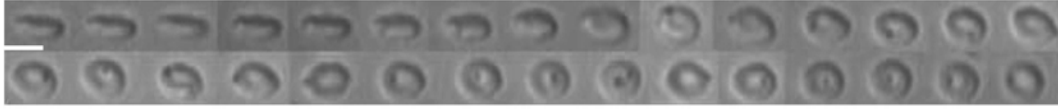


**Figure 2.** transition from rolling to tanktreading. The flow is from right to left RBCs. top series:  $\dot{\gamma} = 3s^{-1}$ , rolling of the cell (images 1-7), followed by a cell position change (images 8 and 9) with spinning (images 10-19) and finally TT (images 20-30)

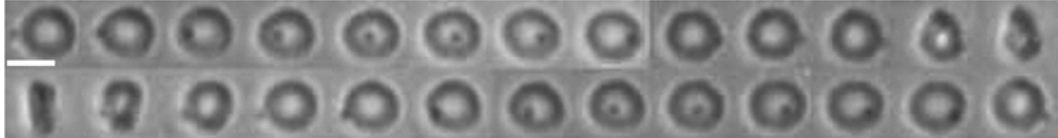


**Figure 3.** TT -flipping transition: intermittence  $\dot{\gamma} = 0.8s^{-1}$ , At the beginning one can observe one half-TT (images 1-10), followed by one tumbling (images 11-17) and another half-TT (images 18-26).

the time variation of  $\theta$  is better described by a model of an elastic ellipsoidal capsule enclosing a viscous fluid. The materials points on the membrane oscillate about their equilibrium positions but the energy barrier due to the shape memory is too high to allow the membrane to fully tanktread.

At higher shear stresses, the energy barrier of the shape memory can be overcome by the energy of the flow. However, we never observe the tumbling motion of a fluid ellipsoid with membrane tanktreading, as described by Keller and Skalak, since the cell's orbit has changed and the cell rolls in the shear plane. We believe that rolling allows the cell to avoid local deformation that costs energy. Indeed, a rolling cell can rotate about its axis of symmetry like a rigid body without internal dissipation.

### Rolling to tanktreading and tanktreading to flipping

Below the threshold of the viscosity ratio and above a critical value of the shear rate, RBCs present a swinging (S) orientation around a mean value while the membrane and cell contents perform a tanktread (T) motion. We explore the rolling - (S)(T) transition induced by increasing the shear rate. It is illustrated in Figure 2. Starting from rolling in the shear plane, the cell tilts and hovers in the flow while its membrane spins about the axis of symmetry. The axis of symmetry does not precess. When the cell finally lies horizontally (the axis of symmetry is then vertical) the streamlines on the membrane change from spinning about the symmetry axis to tanktreading. Local deformations (bumps) sometimes appear on the cell surface. Upon increasing the shear rate, the local deformations disappear and the cell presents a nice biconcave shape. It is striking that, contrarily to most simulations, the biconcave shape is maintained even if the energy barrier due to the shape memory is overcome so that the membrane can rotate about the cellular shape due to the bending energy.

The (T) - flipping transition is observed by decreasing the shear rate (Figure 3). Close to the transition the cell tanktreads and presents a biconcave shape. At the transition the cell exhibits a transient intermittent regime. Several swinging/tanktreading periods are followed by one tumbling. The intermittent regime finally stops and the cell flips continuously. The cell final orientation is close to that of rolling. At this stage, increasing the shear rate leads to the progressive orbit change of the cell, which finally fully rolls. A striking point concerns cell deformation, which never exceeds 10 %. The cell remains biconcave.

The transition presents a strong hysteresis: the critical shear rate for the rolling - (TT) transition is higher than the critical shear rate for the (TT) - flipping transition. There is a shear rate range where both flipping with a definite  $\phi$  angle and (S) (TT) are possible stable motions for the cells.

## CONCLUDING REMARKS

We have explored the regimes of motion of RBCs in a shear flow. We have revealed that the orientation of flipping RBCs depends on the shear rate. At high shear rate, RBCs roll in the shear plane. This behaviour is due to the elastic contribution of the cell membrane. For the first time the transition from rolling to swinging-tanktreading have been carefully observed. It shows cell hovering and a spectacular change of the membrane motion. The transition from swinging-tanktreading to flipping is also observed and discloses a transient intermittent regime. A striking point is that the cell does not deform much, even if the elastic energy due to the shape memory is overcome by the external flow energy. In particular, the biconcave shape is always preserved in the explored range of shear rates. When the membrane tanktreads, the following question then rises: when a material point initially at the rim of the membrane reaches the position which was initially at the cell dimple, what is the mechanical parameter that still imposes the existence of a dimple at this local position? We suggest that this may be due to the bending energy, which could be higher than the elastic energy barrier due to the shape memory. A low energy barrier due to shape memory would imply that the resting shape for the RBC, i. e. the shape that stores no elastic energy is not a biconcave disk but is closer to a sphere. We hope that these new features will stimulate new experiments and theoretical approaches.

## References

- [1] H. Goldsmith and J. Marlow, Proc. R. Soc. Lond. B. **182**, 351 (1972).
- [2] T. Fischer and H. Schmid-Schonbein, Blood Cells **3**, 351 (1977).
- [3] M. Bitbol, Biophys J. **49**,1055 (1986)
- [4] S. Keller and R. Skalak, J. Fluid Mech. **120**, 27 (1982).
- [5] T. Fischer, Biophys. J. **86**, 3304 (2004).
- [6] M. Abkarian, M. Faivre, and A. Viallat, Phys. Rev. Lett., **98**, 188302 (2007)
- [7] M. Abkarian and A. Viallat, Soft Matter, **4**, 653 (2008)
- [8] J. Dupire, M. Abkarian , A. Viallat, Phys. Rev. Lett., **104**, 168101 (2010)
- [9] Finken R, Kessler S, Seifert U, J. Phys.: Condens. Matter **23**, 184113 (2011) and references therein

**OPTIMALITY IN CELLULAR HYDRODYNAMICS**

Eric Lauga

*University of California, San Diego, USA*

Fluid mechanics plays a crucial role in many cellular processes [1]. One example is the external fluid mechanics of motile cells such as bacteria, spermatozoa, algae, and essentially half of the microorganisms on earth [2]. The most commonly-studied organisms exploit the bending or rotation of a small number of flagella (short whip-like organelles, length scale from a few to tens of microns) to create fluid-based propulsion. Ciliated microorganisms swim by exploiting the coordinated surface beating of many cilia (which are short flagella) distributed along their surface [3].

After a short introduction to the fundamentals of fluid-based locomotion on small scales, we pose separate optimization problems addressing the optimal geometries and locomotion gaits of low-Reynolds-number swimmers. First, we characterize the optimal dynamics of simple flapping swimmers with two degrees of freedom. Second, we derive analytically and computationally the optimal waveform of an elastic flagellum [4], such as the one employed by eukaryotic cells for propulsion. Third, we investigate the optimal shapes of helical propellers, and use our results to help rationalize the shape selection mechanism in bacterial flagella [5]. Finally, we characterize the optimal locomotion by surface distortions of blunt swimmers, and demonstrate the appearance of waves, reminiscent of the metachronal waves displayed by ciliated organisms [6].

**References**

- [1] R.D. Kamm, *Annu Rev Fluid Mech* **34** 211-32 (2002).
- [2] C. Brennen and H. Winet, *Annu Rev Fluid Mech* **9** 339-398 (1977).
- [3] J. R. Blake and M. Sleigh, *Biol. Rev.* **49** 85-125 (1974).
- [4] S. E. Spagnolie and E. Lauga, *Phys. Fluids* **22** 031901 (2010).
- [5] S. E. Spagnolie and E. Lauga, *Phys. Rev. Lett.* **106** 058103 (2011).
- [6] S. Michelin and E. Lauga, *Phys. Fluids* **22** 111901 (2010).

## MICROROBOTS: (ARTIFICIAL) LIFE AT LOW REYNOLDS NUMBERS

Bradley J. Nelson

*Institute of Robotics and Intelligent Systems, ETH Zurich, 8092 Zurich, Switzerland*

Fluid Microrobotics has recently entered the phase in which sub-mm sized autonomous robots are being realized. While the potential impact of these devices on society is high, particularly for biomedical applications [1], many challenges remain in developing genuine microrobots that will be useful to society. This talk will focus on approaches to the locomotion of microrobots in liquid [2]. Issues in the design of external systems for providing energy and control of microrobots must be considered, and the use of externally generated magnetic fields in particular appears to be a promising strategy [3]. Theoretical and experimental issues will be discussed [4], functionalization of the devices, and efforts to scale microrobots to the nanodomain will be presented.

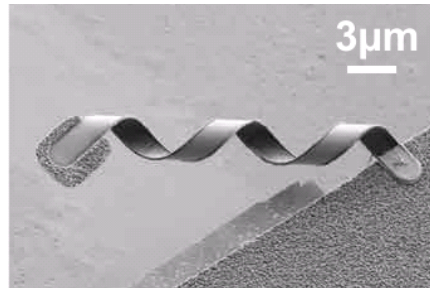


**Figure 1.** An artificial bacterial flagellum (ABF)

### References

- [1] B. J. Nelson, I. K. Kaliakatsos, J. J. Abbott, *Annual Review of Biomedical Engineering* **12**, June 2010.
- [2] J.J. Abbott, K.E. Peyer, M.C. Lagomarsino, L. Zhang, L.X. Dong, I.K. Kaliakatsos, B.J. Nelson, *International Journal of Robotics Research*, July 2009.
- [3] M. Kummer, J.J. Abbott, B.E. Kratochvil, R. Borer, A. Sengul, B.J. Nelson, *IEEE Transaction on Robotics* **26** 6, September 2010.
- [4] L. Zhang, J. J. Abbott, L.X. Dong, K.E. Peyer, B.E. Kratochvil, H.X. Zhang, C. Bergeles, and B.J. Nelson, *ACS Nano Letters* **9** 10, 3663-3667, October 2009.

## INTERSTITIAL AND LYMPHATIC FLOW: MORE THAN JUST A DRAINAGE SYSTEM

Melody A. Swartz

*Institute of Bioengineering, École Polytechnique Fédérale de Lausanne, Switzerland*

In most tissues, slow flow through the 3D extracellular environment – interstitial flow – is always directed towards draining lymphatic vessel. Increased flow occurs in healing wounds, and one of the first responses to tissue insult, injury, or infection is increased lymph flow from the affected site due to vascular hyperpermeability and immune cell influx.

Our lab is interested in understanding the mechanobiology of interstitial and lymphatic flow, both in terms of what it does to cells and its implications for immunology as well as how it is sensed and regulated by lymphatic vessels. Using *in vivo*, *in vitro*, and *in silico* systems, we investigate the role of interstitial fluid flow on lymphangiogenesis, lymphatic fluid drainage function, immune cell trafficking towards and into lymphatics, and other immunological function of lymphatic endothelium, as well as the underlying mechanical and mechano-chemical mechanisms of such phenomena.

First, we have shown how flow can organize lymphatic capillaries during vasculogenesis-like lymphangiogenesis, in 3D tissue culture models [1-3] and *in vivo* dermal wound healing [4]. Then, we demonstrate how draining fluid flow (slow basal to apical flow, across a lymphatic monolayer) is an important mechanical signal to both immune cells and lymphatic endothelium, which can sense and respond to draining flow in ways that affect overall fluid transport, solute transport, and immune cell trafficking [5]. Upon antigen uptake, immune cells can use fluid flow as a signal to direct the cells to the nearest draining lymphatic vessel from the tissue [6,7]. Furthermore, lymphatic endothelium differentially responds to transmural flow vs luminal shear stress to upregulate immune cell adhesion molecules basally, for transmigration into the lymphatics, but downregulate them on the luminal side for efficient trafficking to lymph nodes. Lymphatic endothelial sensitivity to flow conditions reflects a fine-tuned system optimally primed to communicate with the lymph node by responding on a much faster time scale than lymphocyte-based communication (such as the classical events of the adaptive immune response, namely where dendritic cells pick up antigen, travel to the draining lymph node (on the order of 6-12 hours), and induce a cognate T cell response). Under flow conditions, the endothelium also differentially responds to different types of danger and inflammatory signals, including bacterial lipopolysaccharide (LPS) and tumor necrosis factor (TNF)-alpha, and these immune functions of lymphatic endothelium are greatly changed during lymphedema or fluid stagnation.

In summary, the lymphatic system senses and actively regulates flow, in turn regulating interstitial flow, which affects many aspects of interstitial cell function and immune response.

### References

- [1] Helm, C.L., Fleury, M.E., Zisch, A.H., Boschetti, F., & Swartz, M.A., *Proc Natl Acad Sci USA* **102** (44), 15779-15784 (2005).
- [2] Helm, C.L., Zisch, A., & Swartz, M.A., *Biotechnol Bioeng* **96** (1), 167-176 (2007).
- [3] Ng, C.P., Helm, C.L., & Swartz, M.A., *Microvasc Res* **68** (3), 258-264 (2004).
- [4] Boardman, K.C., & Swartz, M.A., *Circ Res* **92** (7), 801-808 (2003).
- [5] Miteva, D.O. et al., *Circulation Research* **106** (5), 920-U181 (2010).
- [6] Fleury, M.E., Boardman, K.C., & Swartz, M.A., *Biophys J* **91** (1), 113-121 (2006).
- [7] Shields, J.D. et al., *Cancer Cell* **11** (6), 526-538 (2007).





## A MODEL OF TISSUE PERFUSION BASED ON HOMOGENIZATION OF DARCY FLOW IN DOUBLE-POROUS LAYERED MEDIUM

Eduard Rohan & Vladimír Lukeš

*Department of Mechanics, Faculty of Applied Sciences, University of West Bohemia, Univerzitní 8, 30614 Pilsen, Czech Republic*

### INTRODUCTION

Our aim is to develop a microstructurally-oriented and computationally efficient modeling tool which will allow for simulations of tissue perfusion. The difficulty of this task originates in structural arrangement of the so-called perfusion tree, bridging several scales, the blood flow descriptions, depending on the scale, and fluid-structure interactions. We focus on modeling the perfusion of tissue parenchym, being motivated by medical applications: a) the assessment of the local cerebral blood flow and b) the liver segmentation (to associate given a point within the liver with one of the hepatic and portal veins). At the level of small vessels and microvessels, the perfusion can be described using the Darcy flow in double porous structure consisting of 3 compartments: two mutually disconnected channels (small arteries and veins) and the matrix (microvessels and capillaries), represented as the dual porosity, where the permeability is decreasing with the scale parameter - the size of the microstructure.

### HOMOGENIZED MODEL AND 3D-TO-2D REDUCTION

We developed a model of homogenized perfusion in the 3-compartment medium constituted by several transversely periodic layers, which enable us to approximate flow through different hierarchies of the porosity. A 3D layered structure in occupying domain  $\Omega_H \subset \mathbb{R}^3$  can be replaced by a finite number of 2D "homogenized layers"  $\Gamma_0 \subset \mathbb{R}^2$  coupled by conditions governing the fluid exchange between them. Each layer is assumed to have a locally periodic structure generated by the reference periodic cell, see Fig. 1. Using this cell, homogenized coefficients relevant to the macroscopic level can be calculated.

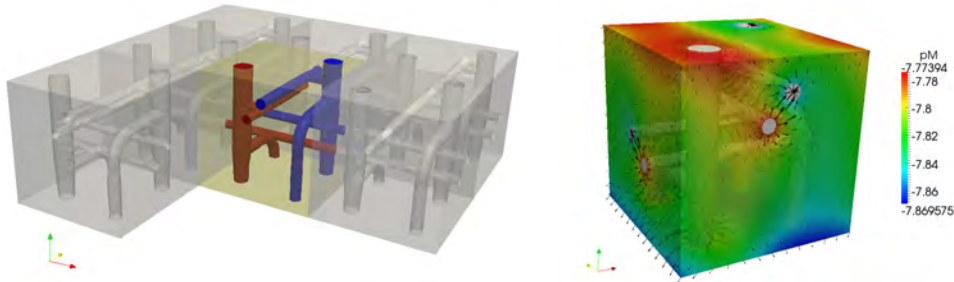


**Fig. 1:** The periodic structure of the layer comprising two channel systems A and B (left) and the postprocessing of micro-flows through the dual porosity; evaluated in the periodic cell for a given macroscopic position  $x \in \Gamma_0$  (right).

#### Macroscopic equation for single layer

The homogenized problem for pressures  $p^A$  and  $p^B$ , associated with the channels A and B, describes 2D parallel flows, cf. [3], in homogenized layer  $\Gamma_0 \subset \mathbb{R}^2$ . Each channel system forms a connected domain (so, we assume at least a small co-lateralization of vessels in the perfusion tree). Two coupled "macroscopic" equations (one for A and one for B) involve the homogenized coefficients: permeabilities  $(\mathcal{K}_{\alpha\beta})^{A,B}$  of the channels, the transmission  $\mathcal{G}$  and drainage  $(\mathcal{S}_\alpha)^{A,B,k}$

(for channel branches  $k \in J_D$ ) coefficients. They govern the fluid redistribution between the two channel systems A and B: for A we have the following equation which is coupled with the similar equation for channel B (i.e. the role of indices A and B is exchanged):

$$-\frac{\partial}{\partial x_\alpha} \left[ \mathcal{K}_{\alpha\beta}^A \frac{\partial}{\partial x_\beta} p^A + \sum_{k \in J_A} \mathcal{S}_{\alpha}^{A,k} \tilde{g}_A^k \right] + \mathcal{G}(p^A - p^B) = c_{hA} \bar{G}_A - \mathcal{F}^{A+} \hat{g}^+ - \mathcal{F}^{A-} \hat{g}^- ,$$

where  $\mathcal{F}^{A+/-}$ ,  $c_{hA}$  are constants (the summation w.r.t. repeated indices  $\alpha, \beta$  applies). Fluxes  $\hat{g}^{+/-}$ ,  $\bar{G}_D$  and  $\tilde{g}_D^k$ ,  $k \in J_D$ ,  $D = A, B$  are given, such that the solvability conditions hold. The term  $\mathcal{G}(p^A - p^B)$ , evaluated at point  $x \in \Gamma_0$ , expresses the amount of fluid (blood) perfused through the matrix (the dual porosity) between sectors A and B. The details are reported in [1].

### Model of N-coupled layers

We consider N layers; in each the perfusion is described by the homogenized model involving macroscopic pressures. Flows between the layers are respected by coupling conditions. In the simplest case, we assume perfect-matching microscopic cells of two attached layers, so that, at the microscopic level, the pressures at the “channel junctions” must equal and the fluxes must be opposite. Analogous conditions express coupling for the pressures and fluxes at the interface in the dual porosity.

This approach allows us to approximate the hierarchical structure of the perfusion tree: in each layer the periodic microstructure can be different.

### Further improvements

To treat real geometries (e.g. perfusion in grey matter of the brain), we consider thick curved layers  $\tilde{\Omega}_H$  that can be mapped onto “flat” layers  $\Omega_H$  which are decomposed into N layers and homogenization is applied for each, as described above. The curvature of the layers and the associated transformation between  $\tilde{\Omega}_H$  and  $\Omega_H$  modifies the homogenized model; the microstructure is only locally periodic, therefore the homogenized coefficients must be computed for “each element” of the macroscopic domain  $\Gamma_0$ .

The model can be extended for microstructures involving more mutually separated channels. Then the number of macroscopic pressures increases correspondingly. We also intend to account for non-steady flows and to include the effect of deforming tissue, see [2].

## CONCLUDING REMARKS

The model has been developed for an approximate description of blood perfusion in brain and liver tissues. Due to the 3D-to-2D reduction and the two-scale decomposition it leads to computationally feasible problem which is now implemented in our in-house developed code *Sfepy* [4]. The solution of the macroscopic problem can be used for the flow reconstruction at the microscopic level. Using the computed velocities we can solve a transport equation describing redistribution of a contrast fluid, to mimic the output of enhanced CT perfusion investigation.

*Acknowledgment:* The research supported by projects MSM 49777513 03 and GACR 106/09/0740 of the Czech Republic.

### References

- [1] Rohan, E.: Homogenization of the perfusion problem in a layered double-porous medium with hierarchical structure. *SIAM, MMS*, 2010. Submitted.
- [2] Rohan, E., Cimrman, R.: Two-scale modelling of tissue perfusion problem using homogenization of dual porous media. *Int. Jour. for Multiscale Comput. Engrg.*, **8**:81–102, 2010.
- [3] Showalter, R.E., Visarraga, D.B.: *Double-diffusion models from a highly heterogeneous medium*, Jour. of Math. Anal. and Appl., **295**:191–210, 2004.
- [4] Cimrman, R. and et al: Software, finite element code and applications, *SfePy* home page. <http://sfepy.kme.zcu.cz>, <http://sfepy.org>, 2009.

## ERYTHROCYTE INFLUENCE ON BLOOD FLOW IN THE CEREBRAL VASCULATURE

J. Reichold<sup>1</sup>, A. Buck<sup>2</sup>, D. Obrist<sup>1</sup>, B. Weber<sup>3</sup> & P. Jenny<sup>1</sup>

<sup>1</sup> *Institute of Fluid Dynamics, ETH Zurich, Zurich, Switzerland*

<sup>2</sup> *Division of Nuclear Medicine, University Hospital Zurich, Zurich, Switzerland*

<sup>3</sup> *Institute of Pharmacology and Toxicology, University of Zurich, Zurich, Switzerland*

### INTRODUCTION

The viscoelastic and oxygen-transport related properties of red blood cells (RBCs) have been subject to extensive study. The effects of shear flow on the erythrocytes include swinging, tumbling and tank treading motion [1-4]. The asymmetrical deformation of the red cells explains their tendency to move towards the midline of a blood vessel [5-6].

It has been shown experimentally, theoretically and in simulation [7-11] that also the inverse is true - that the RBCs in turn have significant impact on the blood flow. In this work, we provide an extension of previously presented modeling frameworks by Obrist and coworkers [11], such that they can be applied to large, realistic vascular networks. The simulations illustrate the influence of the erythrocytes on blood flow in the cortical vasculature.

### METHODS

Obrist et al. have devised two approaches to simulate the blood flow in capillary networks. One in which the red cells are resolved, and another in which the hematocrit is assumed a continuous real number. Both models assume two main RBC-based effects. First, the resistance to flow increases with increasing numbers of red cells in a vessel. Second, the distribution of erythrocytes is governed by a bifurcation rule - stating that the RBCs at a vascular bifurcation follow the path of the steepest local pressure gradient.

Both, discrete and continuum methods, are extended to work with physiological angiography data, containing a mixture of capillary and non-capillary vessels. In non-capillary vessels the bifurcation rule cannot be applied, since it relies on the assumption that RBCs approach the vascular junction along the midline of the vessel. Therefore, the vertices of the vascular graph (bifurcations) are either classified as capillary or non-capillary, depending on the diameter of the vessels that transport blood toward the vertex. If all feeding vessels are capillaries, the vertex qualifies as a capillary vertex and the bifurcation rule can be applied. If not, the red cells are distributed according to the empirical data provided by Pries and coworkers [10].

### RESULTS

The extended discrete and continuum models are applied to realistic vascular networks of the rat somatosensory cortex. The angiography data are obtained by synchrotron radiation based X-Ray tomographic microscopy (srXTM), which fully resolve the blood vessels down to capillary size (isotropic 700 nanometer voxels).

The self-consistency of the simulation-framework is demonstrated by comparing the results of both models. Moreover, the results are compared with the empirical model of Pries et al. [10]. The differences between flow seeded with red blood cells and pure plasma flow are shown for both baseline and stimulus conditions.

Finally, the influence of red cell elasticity on blood flow and RBC distribution is investigated.

### References

- [1] Skotheim, J. M. & Secomb, T. W.: Red blood cells and other nonspherical capsules in shear flow: oscillatory dynamics and the tank-treading-to-tumbling transition. *Phys Rev Lett*, **98**: 078301, 2007.
- [2] Abkarian, M.; Faivre, M. & Viallat, A.: Swinging of red blood cells under shear flow. *Phys Rev Lett*, **98**:

- 188302, 2007.
- [3] Fischer, T. M.: Tank-tread frequency of the red cell membrane: dependence on the viscosity of the suspending medium. *Biophys J*, **93**: 2553-61, 2007.
  - [4] Korin, N.; Bransky, A. & Dinnar, U.: Theoretical model and experimental study of red blood cell (RBC) deformation in microchannels. *Journal of biomechanics*, **40**: 2088-95, 2007.
  - [5] Carr, R. T.: Estimation of hematocrit profile symmetry recovery length downstream from a bifurcation. *Biorheology*, **26**: 907-20, 1989.
  - [6] Secomb, T. W.; Styp-Rekowska, B. & Pries, A. R.: Two-dimensional simulation of red blood cell deformation and lateral migration in microvessels. *Annals of biomedical engineering*, **35**: 755-65, 2007.
  - [7] PapenfuB HD, Gross JF: Microhemodynamics of capillary networks. *Biorheology* **18**:673-692, 1981.
  - [8] PapenfuB HD, Gross JF: Mathematical simulation of blood flow in microcirculatory networks, in Popel AS, Johnson PC (eds): *Microvascular Networks: Experimental and Theoretical Studies*. Basel, Switzerland, S Karger, AG, pp 168-181, 1986.
  - [9] Secomb TW, Pries AR, Gaehtgens P, Gross JF: Theoretical and experimental analysis of hematocrit distribution in micro- circulatory networks, in Lee JS, Skalak TC (eds): *Microvascu- lar Mechanics: Hemodynamics of Systemic and Pulmonary Microcirculation*. New York, Springer-Verlag, pp 39-49, 1989.
  - [10] Pries, A. R., Secomb, T. W., Gaehtgens, P. & Gross, J. F.: Blood flow in microvascular networks. Experiments and simulation. *Circ Res*, **67**: 826-34, 1990.
  - [11] Obrist D, Weber B, Buck A, Jenny P.: Red blood cell distribution in simplified capillary networks. *Philos Transact A Math Phys Eng Sci.*, **368**: 2897-918, 2010.

## PARTICLES AND BLOOD CELLS AT BIFURCATIONS IN CAPILLARY NETWORKS

Gwennou Coupier<sup>1</sup>, Vincent Doyeux<sup>1</sup>, Sarah Peponas<sup>1</sup>, Mourad Ismail<sup>1</sup> & Thomas Podgorski<sup>1</sup>

<sup>1</sup> *Laboratoire Interdisciplinaire de Physique (LIPhy), CNRS - Université Joseph Fourier - Grenoble, 140 rue de la Physique, 38402 Saint-Martin d'Hères, France*

### INTRODUCTION

When blood flow reaches an asymmetric bifurcation in the microcirculation, it is well known that blood cells split in such a way that the hematocrit typically increases in the high flow rate branch and decreases in the other one. This phenomenon is sometimes called the Zweifach-Fung effect [1, 2] and is partly responsible for large hematocrit fluctuations observed in capillary networks. Many in-vivo studies on blood flow (see [3] for a review), or in-vitro studies [4, 5, 6] have been devoted to this effect, including to design sorting or purification devices based on this principle. As proposed in many papers, focusing on rigid spheres can already give some keys to understand or control this phenomenon [7, 5, 8].

An important factor is the spatial distribution of particles in the inlet channel. The existence of a particle/cell free layer near the walls, known as plasma skimming, favours the high flow rate branch.

In addition, the final distribution is influenced by hydrodynamic phenomena that seem to occur at the bifurcation, that can make particles or cells follow a different path than streamlines.

To study these specific phenomena, we consider rigid spheres as a model system, for which no transverse migration in the upstream channel is expected. We experimentally and numerically investigate their behaviour through symmetric T-shaped bifurcations (figure 1) in the dilute regime. We show that an attraction toward the low flow rate branch partly balances the tendency to concentrate particles in the high flow rate branch due to depletion near the walls in the inlet channel [9].

### METHOD AND RESULTS

The experimental set-up is a standard microfluidic device allowing to control separately the flow rate ratio in the two daughter branches and the transverse position of the flowing sphere in the inlet branch. This is done by adding a flow focusing section before the bifurcation, as

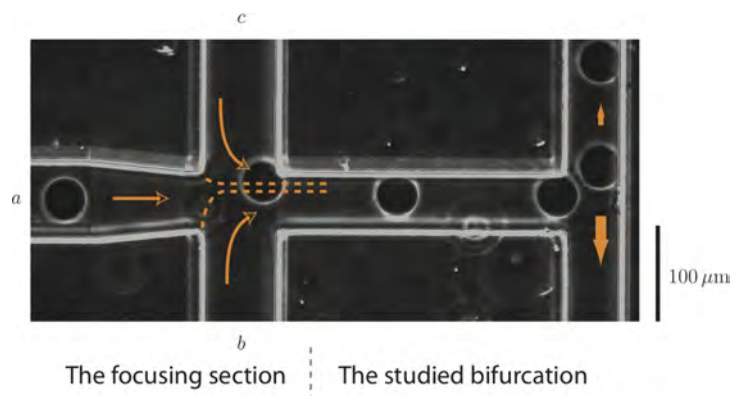


**Figure 1.** Picture of the experimental set-up: a focusing section precedes the studied bifurcation.

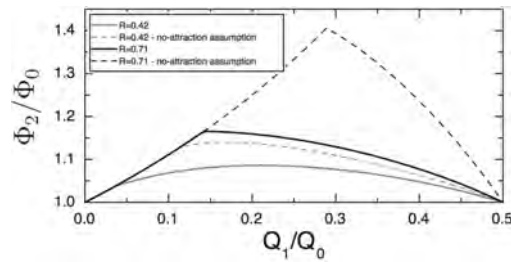


**Figure 2.** Full lines: volume fraction of beads  $\Phi_2/\Phi_0$  as a function of flow rate distribution  $Q_1/Q_0$  for two particle radii  $R = 0.42$  and  $R = 0.71$  (the half-width of the channels is 1). The results are compared with the hypothesis where the particles would follow the streamlines (dashed lines).  $\Phi_i$  and  $Q_i$  denote respectively the particle volume fraction in branch  $i$  and the fluid flow rate in branch  $i$  (0 : inlet branch, 1 and 2: outlets)

seen in figure 1. The different initial transverse positions for a particle can be scanned, and the chosen daughter branch compared with the one a fluid particle would have entered. In addition, 2D-simulations based on a penalty method were run.

Our study shows an attraction of particles towards the low flow rate branch: in the immediate vicinity of the separating streamline of the particle-free fluid, all particles flow towards the low flow rate branch, as soon as they are large enough (typically, a ratio of at least 0.5 between the particle diameter and the channel width is required). The discrepancy between the fluid and the particle behaviour increases with the particle size and with the flow rate ratio between the high flow rate branch and the low flow rate branch.

Simulations show that the net effect is always an enrichment in particles of the high flow rate branch due to the distribution effect, even assuming a homogeneous distribution in the inlet channel (figure 2). However, these two antagonistic phenomena are of comparable importance, and none can be neglected: the particle volume fraction increase in the high flow rate branch is typically divided by two because of the attraction effect, in particular for large particles: while, in case the particles follow their underlying fluid streamline, the maximum enrichment in the high flow rate branch would be around 40% for  $R = 0.71$ , it drops down to less than 17% in reality.

For deformable particles like blood cells, initial lateral migration can induce a narrowing of their distribution, which eventually favours the high flow rate branch.

## References

- [1] K. Svanes and B. W. Zweifach. Variations in small blood vessel hematocrits produced in hypothermic rats by micro-occlusion. *Microvasc. Res.*, 1:210–220, 1968.
- [2] Y. C. Fung. Stochastic flow in capillary blood vessels. *Microvasc. Res.*, 5:34–48, 1973.
- [3] A. R. Pries, T. W. Secomb, and P. Gaethgens. Biophysical aspects of blood flow in the microvasculature. *Cardiovasc. Res.*, 32:654–667, 1996.
- [4] J. W. Dellimore, M. J. Dunlop, and P. B. Canham. Ratio of cells and plasma in blood flowing past branches in small plastic channels. *Am. J. Physiol. Heart Circ. Physiol.*, 244:H635–H643, 1983.
- [5] S. Yang, A. Ündar, and J. D. Zahn. A microfluidic device for continuous, real time blood plasma separation. *Lab on a Chip*, 6:871–880, 2006.
- [6] R. D. Jäggi, R. Sandoz, and C. S. Effenhauser. Microfluidic depletion of red blood cells from whole blood in high-aspect-ratio microchannels. *Microfluid Nanofluid*, 3:47–53, 2007.
- [7] D. M. Audet and W. L. Olbricht. The motion of model cells at capillary bifurcations. *Microvasc. Res.*, 33:377–396, 1987.
- [8] J. O. Barber, J. P. Alberding, J. M. Restrepo, and T. W. Secomb. Simulated two-dimensional red blood cell motion, deformation, and partitioning in microvessel bifurcations. *Ann. Biomech. Eng.*, 36:1690–1698, 2008.
- [9] V. Doyeux, T. Podgorski, S. Peponas, M. Ismail, and G. Couplier. Spheres in the vicinity of a bifurcation: elucidating the Zweifach-Fung effect. *Accepted for publication in J. Fluid Mech.*, 2010.

## FROM CEREBRAL BLOOD FLOW MODELING TO VASCULAR UNITS IN PRIMATE CORTEX

Romain Guibert<sup>1,2</sup>, Caroline Fonta<sup>2</sup> & Franck Plouraboué<sup>1</sup>

<sup>1</sup> *Université de Toulouse ; INPT, UPS ; IMFT (Institut de Mécanique des Fluides de Toulouse) ; Allée Camille Soula, F-31400 Toulouse, France*

<sup>2</sup> *Université de Toulouse; UPS; Centre de Recherche Cerveau et Cognition; France*

### INTRODUCTION

The amazing topological and geometrical complexity of micro-vascular networks in the brain, and in other organs, has challenged many researchers for decades. Since the brain's vascular system is structured by a highly reticulated pial surface network which plunges down into a set of penetrating vessels, it is tempting to attribute a vascular unit to each penetrating arteriole. Recent experimental analysis have led to a breakthrough on the properties of the blood supply in the brain [1]. Penetrating arterioles have been identified as the bottleneck of brain perfusion [2]. Furthermore, it has also been realized that targeted clots of penetrating arterioles are not compensated by active changes in the diameter of their neighbor arteries [3]. This observation suggests passive compensatory mechanisms resulting from the couplings between arteriolar territories consistent with other recent observations of active blood flow reorganization via collateral vessels (inter-arterial connections) [4]. A systematic investigation of the three-dimensional extent of compensation is not possible with experimental measurements but in silico simulations permit a systematic investigation of the spatial distribution of the brain perfusion. The direct computation of blood flow considering a complete mechanical description of its components interactions (red blood cells, plasma, vessel shape, Endothelial Surface Layer – ESL –) over several cubic millimeters of tissue is a more than challenging task for any computer at present. Approximate methods are needed to provide a realistic picture of blood distribution inside tissues [5]. Such approximate network method have permitted to realize that vessel shape, realistic boundary conditions, and in vivo (ESL included) effective apparent viscosity are important ingredient for the pressure and blood flux distributions [5]. We analyze here the functional topological and spatial couplings of arteriolar and venous inputs/outputs.

### VASCULAR TERRITORIES ANALYSIS

#### Definition

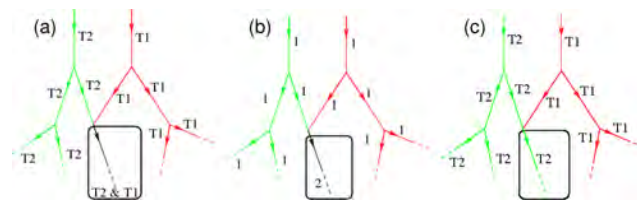


**Figure 1.** (a) Illustration of Perfusion/Drainage Territory and (b) Robustness Index (RI).

- *Perfusion-Drainage Territory* (PDT) is defined as the entire region either spanned through perfusion (Arterial PDT), or drained by perfusion (Venular PDT) (see Figure 1a) which are possibly overlapping.
- *Arterial/Venular Robustness Map* (ARM, VRM) quantifies the redundancy of the perfusion at one point (see Figure 1b). Arterial Robustness Map (ARM) provides, for each segment, the number of input penetrating arteries which contribute to its perfusion, a number called Arterial Robustness Index (ARI).



### Vascular territories evaluation

We analyze the territories of 37 penetrating arterioles and 24 draining venules resulting from the analysis of 18 cubic millimeters of monkey cerebral cortex where the blood perfusion has been previously evaluated [5]. Figures 2a,c and Figures 2b,d illustrate the arterial and venous Perfusion/Drainage Territories (PDT) respectively.

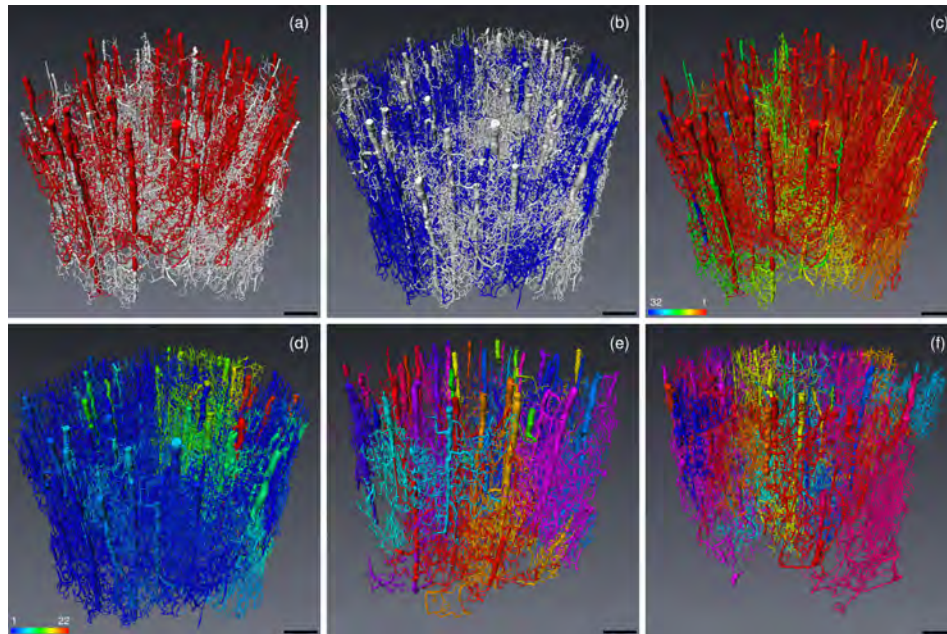


**Figure 2.** (a) Non overlapping Arterial Preferential Drainage Territory regions are displayed in red whilst overlapping one are represented in white, (b) same convention as (a) for Venous Preferential Drainage Territory with blue instead of red, (c) Arteriolar Robustness Map (ARM) and (d) Venular Robustness Map (VRM). (e) Arteriolar PT (APT), (f) Venular PT (VPT).

### CONCLUDING REMARKS

These estimations support the classical picture of preferential neighbors hemodynamics interactions of vascular territories, either inside the network, or between pial input/output penetrating vessels. Although we found very localized functional couplings between preferential arterio/venular partners, we also brought to the fore important potential collateral supplies which can be distributed over a surprisingly large spatial extent.

### References

- [1] Schaffer CB, et al. (2006) Two-photon imaging of cortical surface microvessels reveals a robust redistribution in blood flow after vascular occlusion. *PLoS Biol.* 4:258–270.
- [2] Nishimura N, Schaffer CB, Friedman B, Lyden PD, Kleinfeld D (2006) Penetrating arterioles are a bottleneck in the perfusion of neocortex. *P. Natl. Acad. Sci. USA* 104:365–370.
- [3] Nishimura N, Rosidi NL, Iadecola C, Schaffer CB (2010) Limitations of collateral flow after occlusion of a single cortical penetrating arteriole. *J. Cerebr. Blood F. Met.* p doi:10.1038/jcbfm.2010.157.
- [4] C. C. Lay, M. F. Davis CHCB, Frostig RD (1981) Mild sensory stimulation completely protects the adult rodent cortex from ischemic stroke. *Plos one* 7:519–579.
- [5] Guibert R, Fonta C, Plouraboué F (2010) Cerebral blood flow modeling in primate cortex. *J. Cerebr. Blood F. Met.* 30:1860–1873.

## FLOW AND TRANSPORT IN THE PLACENTA: HOMOGENIZING HAEMODYNAMICS IN A DISORDERED MEDIUM

O.E. Jensen<sup>1</sup>, I.L. Chernyavsky<sup>1</sup>, W.R. Wan Abdullah<sup>1</sup>, I.L. Dryden<sup>2</sup>, A.A. Hill<sup>1</sup> &  
L. Leach<sup>3</sup>

<sup>1</sup> *School of Mathematical Sciences, University of Nottingham, University Park,  
Nottingham NG7 2RD, UK*

<sup>2</sup> *Department of Statistics, LeConte College, University of South Carolina, Columbia,  
SC 29208, USA,*

<sup>3</sup> *School of Biomedical Sciences, University of Nottingham, University Park,  
Nottingham NG7 2RD, UK*

### INTRODUCTION

The placenta is an essential element of the life-support system for the developing fetus, enabling nutrients and waste to be exchanged between the fetal and maternal circulations. Unlike most microcirculatory networks, in which blood is confined to narrow capillaries, maternal blood in the human placenta flows freely in the space between the branches of villous trees, within which are fetal vessels. Placental development is vulnerable to maternal diseases such as pre-eclampsia and diabetes, and damage to the fetus due to placental insufficiency can have immediate consequences as well as effects that last into adulthood. It is therefore valuable to understand how blood flow and nutrient exchange are influenced by the complex geometric arrangement of villous branches.

### METHODS

The functional placental unit is a ‘placentone,’ which comprises a spiral artery in the uterine wall (the decidua), a single villous tree and nearby decidual veins. In a first approximation, the movement of maternal blood from the spiral artery into the intervillous space can be modelled as a flow in a homogeneous porous medium, using Darcy’s law [1] or its variants [2] to describe velocity and pressure fields averaged over many villous branches; an advection/diffusion/reaction equation may also be used to model the macroscopic transport of nutrients such as glucose or oxygen. Formally, both models can be derived using a homogenization approximation that assumes a spatially periodic or uniformly random microstructure.

Numerous refinements to this relatively crude approximation may be considered.

- (i) The rheology of blood in networks of capillaries (treated as bifurcating cylindrical tubes) is reasonably well characterised. Nonlinearities in viscosity and hematocrit transport properties can lead to complex hematocrit dynamics even in simple networks [3,4]; we examine this using coupled nonlinear hyperbolic PDEs distributed over networks. In contrast, blood rheology in the tortuous intervillous space is much less well understood, as are the implications for hematocrit distributions in the placenta.
- (ii) Villous branches have a complex spatial distribution that requires careful statistical characterisation. We apply two measures to histological images (sampling villous area fraction as a function of window size; and estimating Ripley’s  $K$ -function for spatial point processes) to establish the minimum distance over which the distribution of villous branches appears statistically homogeneous.
- (iii) Given the statistical properties of the distribution of villous branches, we assess the accuracy of the leading-order homogenization approximation for nutrient transport. We do so using a simplified model problem (steady solute transport by a unidirectional flow past a distribution of point sinks) which incorporates the influence of two key transport parameters (Péclet and Damköhler numbers,  $Pe$  and  $Da$ ).

## RESULTS

Modelling maternal blood flow in a placentone using Darcy's law reveals the importance of the calibre of the spiral artery and decidual veins in determining the overall flow resistance of the unit [1]. This may be offset by the presence of a cavity in the villous tree near the exit of the spiral artery. This leading-order model also suggests how the efficiency of nutrient transport can be optimized at a suitable villous-branch volume fraction.

Analysis of histological data shows that the villous branches appear to have a statistically homogeneous distribution over sufficiently large distances, but a so-called 'hard-core' distribution over shorter distances.

For physiologically relevant parameter values, and using periodic and stochastic sink distributions in the model solute transport problem, we find that the difference between the leading-order homogenization approximation and the exact nutrient distribution (the 'homogenization residue') is characterized by large spatial gradients at the scale of individual villi: the leading-order approximation converges only weakly to the true concentration distribution. Furthermore, using both Monte Carlo simulations and a multiple-scales analysis, we find that the residue exhibits substantial spatial fluctuations that can be correlated over lengthscales comparable to the whole domain. In contrast to transport problems with periodic microstructure, disorder in the spatial distribution of villous branches substantially reduces the size of the regime in  $(Pe, Da)$ -space in which the homogenization approximation is valid.

Simulations accounting for nonlinear rheology in simple capillary networks point to the prevalence of temporal fluctuations in hematocrit; such effects can be expected to further enrich transport phenomena in the placenta.

## CONCLUSIONS

Our results highlight the importance of quantifying errors due to spatial and temporal disorder in multiscale approximations of transport processes in physiological systems. Leading-order homogenization approximations provide valuable insights of overall function but fail to resolve fine-scale structures which may be of physiological significance.

## References

- [1] Chernyavsky, I.L., Jensen, O.E., Leach, L.: A mathematical model of intervillous blood flow in the human placentone. *Placenta* **31**:69–76, 2010.
- [2] Erian, F.F., Corrsin, S., Davis, S.H.: Maternal placental blood flow: a model with velocity-dependent permeability. *J. Biomech.* **10**:807–814, 1977.
- [3] Kiani, M.F., Pries, A.R., Hsu, L.L., Sarelius, I.R., Cokelet, G.R.: Fluctuations in microvascular blood flow parameters caused by hemodynamics mechanisms. *Am. J. Physiol.* **266**:65–73, 1994.
- [4] Pop, S.R., Richardson, G.W., Waters, S.L., Jensen, O.E.: Shock formation and nonlinear dispersion in a microvascular capillary network. *Math. Med. Biol.* **24**:379–400, 2007.

### **THREE-DIMENSIONAL EFFECTS IN THE FLOW OF BIOARTIFICIAL CAPSULES IN PORES**

Dominique Barthès-Biesel<sup>1</sup>, Xuqu Hu<sup>1</sup>, Anne-Virginie Salsac<sup>1</sup> & Thi-Xuan Chu<sup>1</sup>

<sup>1</sup>*Biomécanique Bioingénierie UMR CNRS 6600, Université de Technologie de  
Compiègne, BP 20529 60205 Compiègne France*

#### **INTRODUCTION**

Encapsulation consists in protecting a substance with a solid envelope to avoid its dispersion in the ambient environment or its degradation in contact with it. Capsules are common in nature (red blood cells, phospholipid vesicles) and in different applications such as pharmacology, cosmetics or biomedical engineering. A fine control of the membrane properties is necessary to control the capsule deformation or possible breakup (to be induced or prevented depending on the application). However, measuring the mechanical properties of the membrane is difficult because capsules are small (from a few microns to a few millimeters) and fragile particles. A way to do this is to flow them in pores with comparable dimensions [1]. The hydrodynamic stresses and the constraints of the channel walls cause large deformation of the capsule that depends on the flow strength and on the particle intrinsic physical properties such as relative size compared with the channel section and membrane constitutive behavior. A sophisticated model for the flow and deformation of a capsule in a pore is necessary to analyze the experimental results. The aim of this presentation is to describe such models and to discuss specifically three-dimensional effects on the flow of an initially spherical capsule flowing into a cylindrical pore or into a square section microfluidic channel.

#### **FLOW OF A SPHERICAL CAPSULE IN A CYLINDRICAL PORE**



**Figure 1.** Pore flow of capsules with ovalbumine membrane: (a) parachute; (b) slug shape and folds in the azimuth direction.

#### **Experimental evidence**

When cross-linked ovalbumin initially spherical microcapsules are flowed into a cylindrical microchannel (radius  $R$ ) of comparable size, they deform and can take parachute or slug shapes as shown in figure 1. The experiments provide values of the capsule velocity  $v$  and the analysis of the capsule profiles yields the initial capsule radius  $a$  (assuming an axisymmetric shape) and the corresponding deformation. As shown in figure 1b, folds may appear on the membrane.

#### **Model of the flow of a capsule in a pore**

An initially spherical capsule is filled with an incompressible Newtonian liquid and enclosed by an infinitely thin elastic membrane. The capsule is freely suspended in another incompressible Newtonian liquid of viscosity  $\mu$ , flowing with mean velocity  $U$  in a cylindrical channel. The flow Reynolds number is supposed to be small so that the internal and external fluid motion obeys the Stokes equations. The membrane is assumed to consist of an infinitely thin sheet of hyperelastic isotropic material with surface shear modulus  $G_s$  and area dilation modulus  $K_s$ .

Different membrane constitutive laws have been proposed to model thin membranes, but we consider here a neo-Hookean law that assumes that the membrane is an infinitely thin sheet of a three-dimensional isotropic volume incompressible material. The model input are the capillary number  $Ca = \mu U/G_s$  that measures the ratio between the viscous and elastic forces and the size ratio  $a/R$ . The model output are the capsule deformed profile at steady state, the velocity ratio  $v/U$  and the elastic tension distribution in the membrane.

### Axisymmetric model

The problem is first integrated in the azimuth direction and solved in a meridian plane by means of a boundary integral technique coupled to a Lagrangian tracking of the capsule interface [2]. This model has been used to determine the shear modulus of capsules with different membranes by means of inverse analysis [1]. The technique basically consists of finding the value of  $Ca$  for which the numerical deformed profile is identical to the experimentally measured one, for a given membrane constitutive law. The value of  $Ca$  then provides the value of the membrane shear elastic modulus  $G_s$ . However, when folds occur as in figure 1b, the deformation becomes three-dimensional. This questions the validity of an axisymmetric model to analyze the experimental results.

### Three-dimensional model

A recent coupling between the boundary integral (BI) method for the fluids and the finite element (FE) method for the membrane has been proposed by [3]. It has the advantage to use the same discretization for the fluids and capsule wall, which allows a Lagrangian tracking of the membrane position with high accuracy. The numerical stability and accuracy of the method have been demonstrated on a spherical capsule placed in different linear unbounded shear flows. We have modified the BI-FE model to treat confined flows such as pore flow. The first results show the occurrence of folds on the surface of the capsule as shown in figure 2. For such moderate deformation of the capsule, the meridional folding does not affect significantly the meridian profile as compared to the results of the axisymmetric model. However, for large deformation the 3D and axisymmetric results deviate from one another.

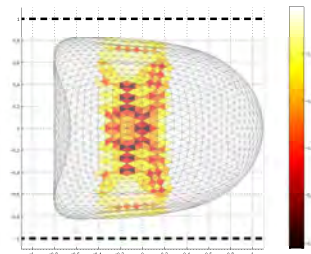


**Figure 2.** 3D computation of a spherical capsule in a cylindrical tube. The color code shows oscillations of compressive tensions on the membrane that lead to folds.

## CONCLUSION

Three-dimensionnal effects are important for the flow of capsules in pores and must be taken into account in cylindrical as well as square section channels.

## References

- [1] Lefebvre, Y., Leclerc, E., Barthès-Biesel, D., Walter, J. & Edwards-Lévy, F. 2008. *Phys. Fluids* **20**, 1-10.
- [2] Lefebvre, Y. & Barthès-Biesel, D. 2007. *J. Fluid Mech.* **589**, 157-181.
- [3] Walter, J., Salsac, A.-V., Barthès-Biesel, D. & Le Tallec, P. 2010. *Int. J. Num. Meth. Engng* **83**, 829–850.

## A NOVEL COMPUTATIONAL APPROACH FOR MODELING HUMAN ERYTHROCYTES IN OSCILLATING SHEAR FLOW

Thomas Klöppel, Wolfgang A. Wall

*Institute for Computational Mechanics, Technische Universität München,  
Boltzmannstr. 15, 85747 Garching b. München, Germany*

### INTRODUCTION

Human red blood cells (RBC, erythrocyte) have been the topic of intensive research during the past decades. Being the main constituent of human blood, this cell governs the rheological behavior, especially when the flow through narrow capillaries is considered. Therefore, a comprehensive model for the human erythrocyte and its interaction with the blood plasma is necessary in order to address the non-Newtonian behavior of human blood numerically. More importantly, such a model will provide an insight into the origin of hemolysis, the limiting factor for the application of artificial blood pumps.

We propose a novel finite element based model that takes the two-layered setup of the cell membrane as well as different fluid properties of cytoplasm and blood plasma into account and present results for a single cell deformed by fluid flow.

### FINITE ELEMENT MODEL

From a numerical point of view the modelling of erythrocytes subjected to fluid flow leads to two major challenges. First, a comprehensive model for the erythrocyte membrane is needed to account for the particular structure of this membrane and its rather remarkable properties. We propose a two-layered continuum-based membrane model [1]. For the very thin outer layer a discretization with incompressible solid shell finite elements, an anisotropic visco-elastic material and an algebraic area constraint are employed, the combination of which ensures a realistic representation of the fluid-like lipid-bilayer and its characteristics, such as bending rigidity, viscosity and resistance against area dilatation. The characteristics of the spectrin network are accounted for by solid shell finite elements and a third-order hyperelastic Yeoh material.

Second, a reliable fluid-structure interaction (FSI) framework has to be formulated that allows for the interaction between membrane and cytoplasm as well as for the interaction between membrane and outer blood plasma. The balloon-like problem emerging from the membrane and the enclosed incompressible cytoplasm necessitates the application of monolithic FSI coupling schemes. Different resolution requirements demands independent mesh generation for blood plasma and RBC membrane. To efficiently deal with the resulting nonconforming FSI interface, we developed a novel dual mortar based monolithic FSI scheme [2]. Additionally, if subjected to shear flow the cell undergoes large rotations, which is also to be dealt with by the FSI framework. Owing to its generality and flexibility the proposed approach can be easily extended to allow for the simulation of rotating structures. In this paper we will present this extension and discuss its application to erythrocyte simulations.

To the authors' knowledge the proposed model is the first model that captures all of the above mentioned properties of the erythrocyte membrane and its interaction with surrounding and enclosed fluid. In addition the number of needed model parameters is kept as low as possible and the same set of parameters, which is consistent with literature, is used for all simulations. Although the presented model accounts for the required properties of healthy RBC, it can easily be adapted to interpret altered RBC mechanics in terms of possible damaging scenarios.

### NUMERICAL EXAMPLES

The cell model is validated with static and dynamic laser trap experiments. We will show that the proposed model is able to accurately predict the response of a human erythrocyte. The

necessity of realistic boundary conditions are briefly discussed and deduced material parameters are compared with literature values.

Experimental results are reported for the behavior of RBC in cyclically reversing shear flow [3]. This experiment has not been addressed in a numerical study, yet. In this paper the proposed FSI approach is shown to provide a suitable framework for the simulation of this experimental setup. The effect of different frequencies is studied and the resulting ratio between major and minor axes of the RBC are evaluate and compared to experimental results.

## References

- [1] Klöppel T., Wall W.A.: A novel two-layer, coupled finite element approach for modeling the nonlinear elastic and viscoelastic behavior of human erythrocytes. *Biomech. Model. Mechanobiol.* DOI: 10.1007/s10237-010-0246-2, 2010.
- [2] Klöppel T., Popp A., Küttler U., Wall W.A.: Fluid-structure interaction for non-conforming interfaces based on a dual mortar formulation. submitted to *Comput. Methods Appl. Mech. Engrg.*, 2010
- [3] Watanabe N, Kataoka H., Yasuda T., Takatani Y.: Dynamic deformation and recovery response of red blood cells to a cyclically reversing shear flow: effects of frequency of cyclically reversing shear flow and shear stress level, *Biophys. J.*, **91**:1984–1998, 2006

## **FLUID DYNAMICS IN A MULTIPLE PARALLEL FLOW-CHAMBER FOR SHEAR-DEPENDENT CELLULAR ADHESION**

Bianchi Elena<sup>1</sup>, Federica Boschetti<sup>1</sup> & Gabriele Dubini<sup>1</sup>

<sup>1</sup> *Structural Engineering Department, Politecnico di Milano,  
Piazza Leonardo Da Vinci 32, 20133 Milano Italy*

### INTRODUCTION

The essential role of leukocytes in inflammation and the knowledge of their adhesion cascade are crucial study areas in developing methods to control inflammation by modulating or blocking leukocyte adhesion to the endothelium. A high-throughput approach can improve results in this field, enabling very rapid and smart parallel experimentations, and increasing productivity by orders of magnitude over traditional approach. To perform a consistent adhesion assay under flow condition knowledge and control over the fluid dynamics inside the test chamber are compulsory: the mechanical stress on the cell induces and rules the leukocyte adhesion to the endothelial membrane. A glass prototype of a micro-device for leukocytes adhesion assays, under flow condition and in multiple chambers, was here characterized from the fluid dynamic point of view. This device includes three groups of chambers: different flow rates reach these groups so that cells face different conditions of wall shear stress. Each group includes three identical chambers in order to get a triplicated result.

Each chamber has a thickness of 50  $\mu\text{m}$ , 1.5 mm of width and 3 mm of length. One of the planar side is made of a polymeric porous membrane. CFD simulations, micro-PIV analyses and pressure-flow rate measurements were performed. Multi-step adhesion behavior of a leukocyte is in fact ruled by a coupled effect of the wall shear stress  $\tau_w$  and the detaching force  $F_D$  exerted by the fluid on the cells.

### COMPUTATIONAL FLUID DYNAMIC SIMULATIONS

Computational fluid dynamics simulations (Fluent Ansys Inc.) were carried out to evaluate the fluid dynamics inside the test chambers and in the distributor structures, located upstream and downstream from the test chambers. Flow field and wall shear stress distribution on the membrane are the main investigated parameters, in order to describe the fluid dynamic conditions faced by leukocytes during the rolling and the adhesion (Fig.1). The establishment length, proportionally increasing with the increase of flow-rate, is about 900  $\mu\text{m}$ , for a low flow-rate of 0.046 mm<sup>3</sup>/s ( $\tau_w = 0.075$  Pa), and increases to about 1100  $\mu\text{m}$ , for the higher flow-rate of 1.848 mm<sup>3</sup>/s ( $\tau_w = 3$  Pa).

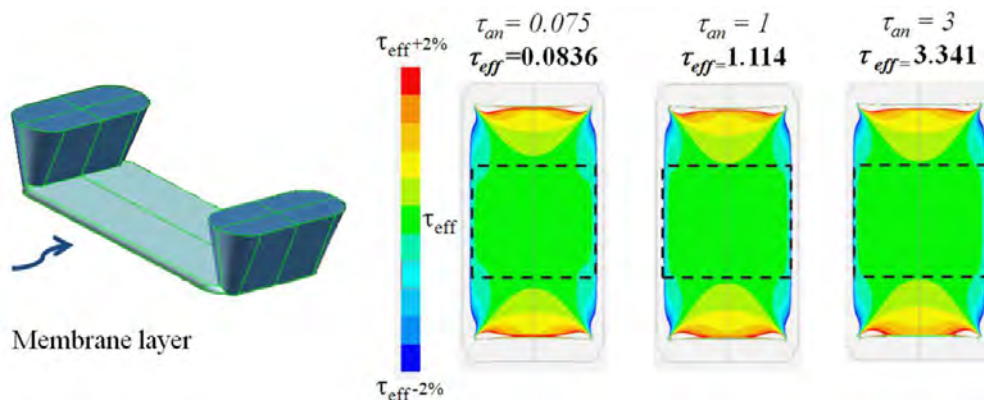
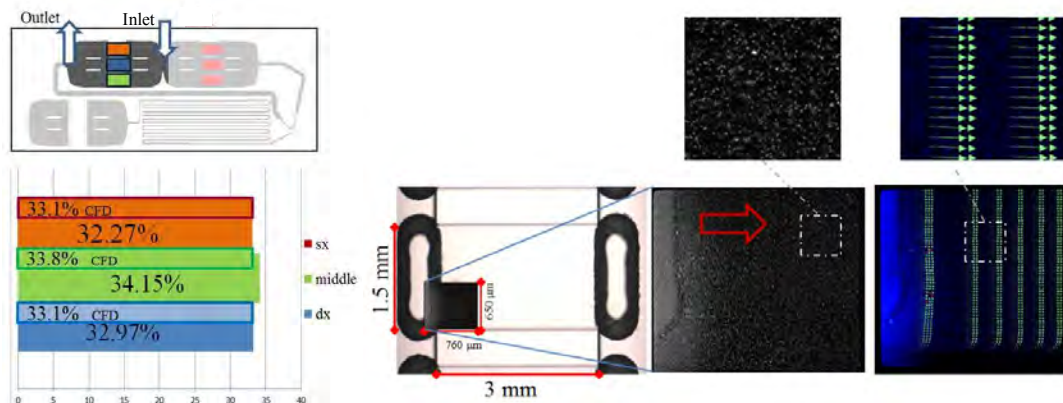


Figure 1. Wall shear stress distribution on the functionalized membrane, target of the cellular adhesion.  $\tau_{an}$  is the analytical prediction and  $\tau_{eff}$  is the value from the CFD simulations.





**Figure 2.** Left: flow-rate distribution among the chambers of a group. Right: micro-PIV images of test chamber.

### MICRO-PIV ANALYSES AND PRESSURE/FLOW RATE MEASUREMENTS

An experimental fluid-dynamic characterization was performed by acquiring the pressure drop of fluid pathways inside the chip, as functions of the flow rate. The experimental data were then compared with the predictions of the analytical model used for the design of the device.

Experimental micro-PIV (Particles Image Velocimetry) analyses were performed (PIV System, TSI) to get information about the local fluid-dynamics inside the test chambers. Velocity maps of the flow field inside the chambers were processed to describe the 2D velocity profile, parallel to the membrane. Sets of vectors delineate the velocity profile. Distortion due to the shape of the inlet channel seems to exhaust its effect in proximity of the connection: velocity is homogeneous in more than the 60% of the length chamber and decrease to zero in proximity of the side round walls. The velocity flow field map of the central area of the chambers gave us the opportunity to estimate the flow-rate flowing in each of the three groups and to estimate the actual distribution of volume flow among two shear stress pathways.

### CONCLUDING REMARKS

CFD and micro-PIV analyses show a uniform distribution of shear stress for more than the 70% of the membrane exposed to the cells. Micro-PIV analyses and pressure-flow rate measurements led to the definition of a new ratio between the values of wall shear stress generated in the different groups, compared with the analytical predictions (from 1:13:40 to 1:~11:~29). Cellular assays are ongoing to evaluate adhesion behavior in the different flow conditions offered by the device.

### Acknowledgements

The authors are grateful to Micronit Microfluidics BV, in particular to Dr.Ir. Marko Blom and Dr. Elwin Vrouwe, for the contribution to the design and for the fabrication of the microfluidic device.

### References

- [1] Alon R. and Ley K.: Cells on the run: shear-regulated integrin activation in leukocyte rolling and arrest on endothelial cells. *Current Opinion in Cell Biology* 20:1-8, 2008.
- [2] Dong C. and Lei X.X.: Biomechanics of cell rolling: shear flow, cell-surface adhesion, and cell deformability. *Journal of Biomechanics*, 33:3543,2000.
- [3] Toesch S.: The evolution of chemotaxis assays from static models to physiologically relevant platforms. *Integrative Biology*, 1:170-181,2009.

## MICROBUBBLE DRIVEN MICROCIRCULATION INSIDE HUMAN CAPILLARIES AND ITS IMPACT ON THE ENDOTHELIUM

W. Wiedemair, V. Kurtcuoglu & D. Poulikakos

*Laboratory of Thermodynamics in Emerging Technologies, Department of Mechanical and Process Engineering, ETH Zurich, Sonneggstrasse 3, 8092 Zurich, Switzerland*

### INTRODUCTION

Blood flow at the vascular endothelium has been shown to influence function and organization of the endothelial cells. Flow induced shear stresses and their temporal variation on the cell surface may trigger a range of reactions reaching from activation of ion transport channels and shift in pH to changes in the cell membrane and structure [1].

The blood-brain barrier (BBB) is formed by a monolayer of endothelial cells linked together by protein sealing strands forming so-called tight junctions. This cell layer lines the luminal surface of capillaries in the brain and constitutes a virtually impermeable barrier for most macromolecular substances. A temporary increase in permeability of the BBB can be achieved by exposing the endothelium to elevated pressure and shear conditions [2]. Even though the exact mechanisms and signal pathways involved remain to be fully elucidated, this approach can readily be used to transiently and locally open the BBB for the transfer of drugs from the vascular system to the brain [3].

The desired mechanical conditions for BBB opening may be attained by administering encapsulated gas-filled microbubbles to the vascular system and exposing them to a high intensity ultrasound field. The resulting forced cavitation of these microbubbles induces local microflow patterns which will impact the vessel walls of capillaries, causing a variation in both pressure and shear stress conditions.

### MATERIALS AND METHODS

We are interested in the micro-scale flow dynamics induced by ultrasound driven microbubble oscillation in the confined environment of a capillary, paying special attention to the conditions close to the wall of the vessel. CFD methods are employed to simulate this transient process in a small section of a capillary containing a single microbubble.

#### Model

In this approach, the bubble is treated as an actuator described by a modified Rayleigh-Plesset equation. The vessel wall is modeled as a compliant elastic solid [4]. Coupling of the fluid and the solid domain is accomplished by using a fluid-structure interaction scheme.

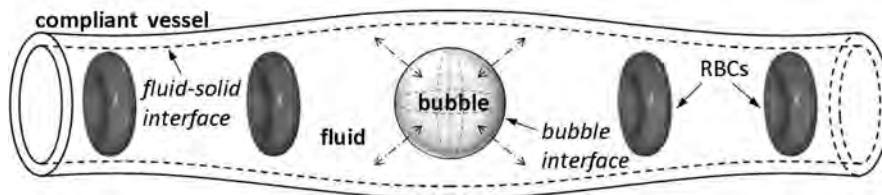


**Figure 1.** Model configuration comprising bubble, fluid with RBCs and compliant vessel region.

The capillary geometry is approximated as a right circular cylindrical tube with the bubble located at its center, rendering the problem axi-symmetric. The vessel is filled by blood plasma with a viscosity close to that of water and treated as an incompressible Newtonian fluid. Solid constitutive blood bodies such as red blood cells (RBCs) are modeled as rigid obstacles partly obstructing the tube inlets to both sides of the bubble (Fig. 1).

### Numerical treatment

The transient simulation of the solid and the fluid domains as well as the coupling algorithm are implemented in the open source CFD environment OpenFOAM. An incompressible, laminar isothermal flow solver and the PISO algorithm for pressure-velocity-coupling [5] constitute elements of the solution methodology for the transient Navier-Stokes and continuity equations.

## RESULTS

Our current model setup comprises a single microbubble of  $2\ \mu\text{m}$  equilibrium diameter embedded between two RBCs at a distance of  $6\ \mu\text{m}$  from its center to both sides inside a tube of  $8\ \mu\text{m}$  diameter. The RBCs obstruct 75% of the inflow cross-section. At these scales and bubble oscillation frequencies around 550 kHz, the Reynolds number with respect to the gap between bubble and vessel wall is in the range between 3 and 9, while with respect to the bubble diameter it ranges from 3.5 to 12.

We observe peak flow velocities of up to 3 m/s near the bubble surface during the contraction phase of the bubble while velocities near the wall stay below 0.5 m/s during the whole cycle. A flow stagnation point is located at the axial center of the RBCs.

We see a homogeneous flow field during bubble expansion. During the rapid bubble contraction phase, the flow being driven by the compliant wall splits into a component following the bubble motion and a second component moving towards the outlet region across the annular channel defined by the vessel lumen and the RBC. The separation line between the two flow domains is located in the vicinity of the RBC and shifts from the central region of the capillary towards the vessel outlet region while the bubble contracts. No vortex formation is observed.

The presence of obstacles like RBCs, usually located around the central axis of the tube and partially obstructing the tube cross section, leads to steep pressure gradients due to the increased flow resistance in their vicinity. This results in a sudden drop in transmural pressure at those locations. At the same time, the wall shear stress (WSS) shows pronounced peaks coinciding with the location of the obstacles. Thus we see the appearance of strong transmural pressure gradients and large WSS in the same location due to the presence of blood cells.

With flow and pressure conditions changing at the frequency of the microbubble oscillation of 550 kHz, very high temporal pressure and shear stress gradients occur as well.

## CONCLUSIONS

The mechanical conditions at the endothelium of vessel walls are considered to play a crucial role in the control of endothelial cell shape and function. Under specific flow conditions, even the permeability of the BBB, which itself is a specialized endothelial layer, can be altered.

Results indicate a strong influence of solid blood particles adjacent to the microbubble on the shear stress and pressure distribution at the endothelial cell layer.

We kindly acknowledge the financial support of the Swiss National Science Foundation through NCCR Co-Me.

### References

- [1] Mazzag B.M. et al.: A Model for Shear Stress Sensing and Transmission in Vascular Endothelial Cells. *Biophys. J.* **84**: 4087–4101, 2003.
- [2] Sheikov N. et al.: Cellular Mechanisms of the Blood-Brain Barrier Opening induced by Ultrasound in Presence of Microbubbles. *Ultrasound Med. Biol.* **30**: 979–989, 2004.
- [3] Vykhotseva N. et al.: Progress and problems in the application of focused ultrasound for blood-brain barrier disruption. *Ultrasonics*, **48**(4): 279–296, 2008.
- [4] Tukovic Z., Jasak H.: Updated Lagrangian finite volume solver for large deformation dynamic response of elastic body. *Transactions of FAMENA* **31**(1): 55–70, 2007.
- [5] Issa R.I.: Solution of the Implicitly Discretised Fluid Flow Equations by Operator-Splitting. *J. Comput. Phys.* **62**: 40–65, 1985.

## INSIGHT INTO THE DEVELOPING VITELLINE NETWORK WITH MICRO-PIV MEASUREMENTS

A. Kloosterman<sup>1</sup>, C. Poelma<sup>1</sup>, B.P. Hierck<sup>2</sup> & J. Westerweel<sup>1</sup>

<sup>1</sup> *Laboratory for Aero & Hydrodynamics, Faculty of Mechanical, Maritime & Materials Engineering, Process & Energy Department*

*Delft University of Technology, Mekelweg 2, 2628 CD Delft, The Netherlands*

<sup>2</sup> *Department of Anatomy & Embryology, Leiden University Medical Center, Postzone S-1-P, PO Box 9600, 2300 RC Leiden, The Netherlands*  
*a.kloosterman@tudelft.com*

### INTRODUCTION

Since fluid dynamics plays a critical role in the development of vascular networks, quantitative information about e.g. wall shear stress, flow rate and velocity profiles is essential. From the velocity profile of the flow, the wall shear stress and flow rate can be derived. When during the development the network's topology and velocity field are obtained consecutively, the insights in the relation between development and flow can be improved ([1]). The vitelline network (extraembryonic vessels) of a chicken embryo is used as a model for investigation.

### IN VIVO MICRO-PIV MEASUREMENTS

#### Measurement depth

Instantaneous velocity profiles can be obtained in vivo by micro Particle Image Velocimetry (micro-PIV). In PIV, the fluid is seeded with tracer particles, which are expected to follow the fluid motions. The velocity of these particles is calculated from their displacement. This technique has successfully been applied in both the embryonic chicken heart ([2],[3]) and in the chicken vitelline network [4]. In these studies, artificial fluorescent tracer particles were used. Using red blood cells (RBCs) as tracer particles will cause an underestimation of the measured velocity due to the large measurement depth (depth-of-correlation). With the method described in [5], a correct interpretation of the measured flow velocities can be made.

#### Consecutive measurements

Accurate velocity information of the blood flow in the vascular network is needed at different stages. To accomplish this for one chicken embryo, it is favourable to use RBCs as tracer ([6]). Some time after injection of the artificial tracer particles, the amount of particles in the circulation diminishes. A low particle seeding concentration or particles stuck on the wall, especially when clots begin to form, make it more difficult to get reliable velocity results. Since RBCs are already present, performing consecutive PIV-measurements at different stages becomes realizable. Characteristic parameters for the network, e.g. vessel diameter, flow rate and wall shear stress, are extracted from the obtained velocity fields. Variation of these parameters and the topology in the different stages of development will be studied in the vitelline network of the chicken embryo. This network is observed during developmental stages (Hamburger & Hamilton) 14-18 (2-3 days old). In these stages, significant changes in the network structure takes place while it is also suitable for PIV-measurements.

#### References

- [1] Reneman, R.S., Arts, T., Hoeks, A.P.G.: Wall shear stress - an important determinant of endothelial cell function and structure - in the arterial system in vivo. *J Vasc Res*, **43(3)**:251-269, 2006.
- [2] Vennemann P., Kiger K., Lindken R., Groenendijk B., Stekelenburg-de Vos S., Ten Hagen T., Ursem N., Poelmann R., Westerweel J., Hierck B.P.: In vivo micro particle image velocimetry measurements of blood-plasma in the embryonic avian heart. *J Biomech* **39(7)**:1191-1200, 2006.
- [3] Poelma C., Van der Heiden K., Hierck B.P., Poelmann R.E., Westerweel J.: Measurements of the wall shear

- stress distribution in the outflow tract of an embryonic chicken heart. *J R Soc Interface* **7(42)**:91–103, 2010.
- [4] Poelma C., Vennemann P., Lindken R., Westerweel J.: In vivo blood flow and wall shear stress measurements in the vitelline network. *Exp Fluids* **45(4)**:703–713, 2008.
- [5] Kloosterman A., Poelma C., Westerweel J.: Flow rate estimation in large depth-of-field micro-PIV. *Exp Fluids* **50(6)**:1587–1599, 2011.
- [6] Lee J.Y., Lee, S.J.: Hemodynamics of the omphalo-mesenteric arteries in stage 18 chicken embryos and 'flow structure' relations for the microcirculation. *Microvasc Res* **80(3)**:402–411, 2010.

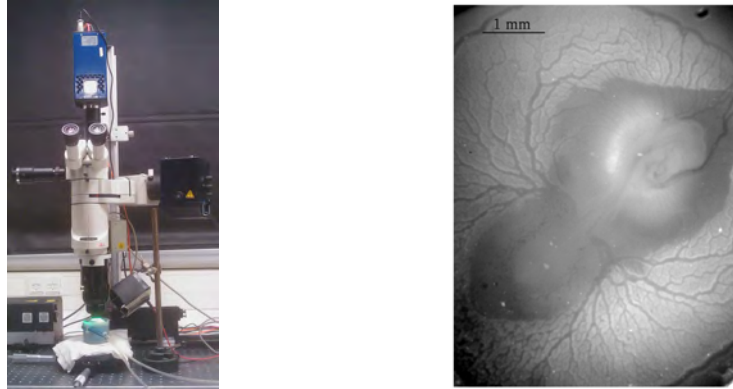


**Figure 1.** The left figure shows the measurement setup with the egg placed under the microscope and the camera (blue) on top. The right figure shows a chicken embryo (56 hours after incubation) with on the top right the head and the tail on the bottom left. The embryo is connected to the yolk sac vasculature.

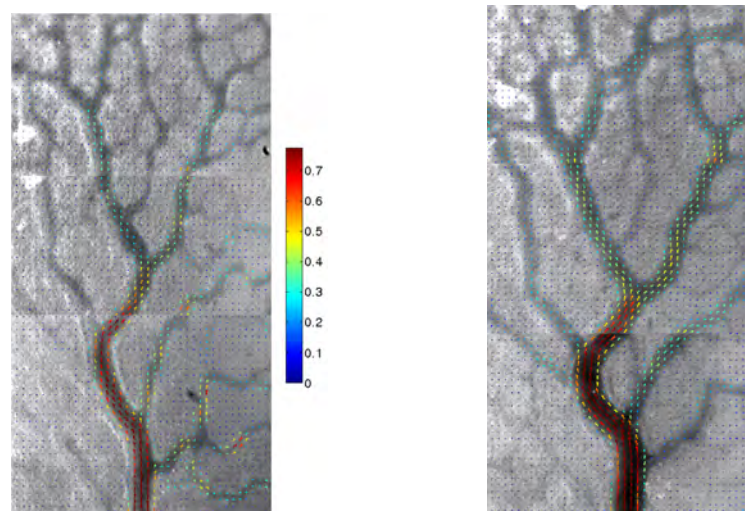


**Figure 2.** Velocity fields obtained by PIV during systole in the same part of the vitelline network of a chicken embryo at two different moments. The left figure shows the velocity field corresponding to the embryo in developmental stage HH15. The right figure shows the velocity field 3 hours later and the measured maximum velocity in this part of the vitelline network has increased 2.5 times in 3 hours. The field-of-view is 1.6 by 3 mm in the left figure and the velocity is given in mm/s in both figures.

## NUMERICAL SIMULATIONS OF PUSHER AND PULLER SQUIRMER IN VISCOELASTIC FLUID

Luca Brandt<sup>1</sup>, Lailai Zhu<sup>1</sup> & Eric Lauga<sup>2</sup>

<sup>1</sup> *Linné Flow Centre, KTH Mechanics, S-100 44 Stockholm, Sweden*

<sup>2</sup> *Department of Mechanical and Aerospace Engineering, University of California San Diego, 9500 Gilman Drive, La Jolla CA 92093-0411, USA*

### INTRODUCTION

Small organisms displaying the ability to move usually do so in the presence of a viscous fluid. This is the case, in particular, for swimming cells such as bacteria, protozoa, or spermatozoa, which exploit the viscous forces induced by the movement of appendages such as flagella or cilia in order to propel themselves in a fluid environment. Although significant progress has been made in the study of motion in Newtonian fluids, many biological cells often encounter viscous environments with suspended microstructures or macromolecules. The physics of micro-propulsion in such a non-Newtonian viscoelastic fluid has only recently started to be addressed [1].

Here we present results of three-dimensional numerical simulations for the steady locomotion of a self-propelled body in a model polymeric (Giesekus) fluid at low Reynolds number. Locomotion is driven by steady tangential deformation at the surface of the body (so-called squirming motion). This is expected to be a good approximation for high density of cilia; in this so-called envelope method [2], the motion of the cilia tips is modeled by the deformation of the body surface.

The surface velocity of a squirmer  $\mathbf{u}_S$  in the co-moving frame, is that considered by Blake [2]

$$\mathbf{u}_S(\mathbf{r}) = \sum_{n \geq 1} \frac{2}{n(n+1)} B_n P'_n \left( \frac{\mathbf{e} \cdot \mathbf{r}}{r} \right) \left( \frac{\mathbf{e} \cdot \mathbf{r}}{r} \frac{\mathbf{r}}{r} - \mathbf{e} \right). \quad (1)$$

Here,  $\mathbf{e}$  is the orientation vector of the squirmer,  $B_n$  is the  $n$ th mode of the surface squirming velocity,  $P_n$  is the  $n$ th Legendre polynomial,  $\mathbf{r}$  is the position vector, and  $r = |\mathbf{r}|$ . In a Newtonian fluid, the swimming speed of the squirmer is  $2B_1/3$  and thus only dictated by the first mode. As in many previous studies, we assume  $B_n = 0$  for  $n > 2$ . Consequently, the tangential velocity on the sphere in the co-moving frame is expressed as  $u_\theta(\theta) = B_1 \sin \theta + (B_2/2) \sin 2\theta$ , where  $\theta = \arccos(\mathbf{e} \cdot \mathbf{r}/r)$  and an additional parameter  $\alpha$ , representing the ratio of the second to the first squirming mode, is introduced. When  $\alpha$  is positive, the swimmer get impetus from its front part, and it is regared as a puller. As  $\alpha$  is negative, the thrust comes from the rear part of the body and the microorganism is a pusher. In our simulations,  $\alpha$  ranges from  $-5$  to  $5$ .

Simulations of an axisymmetric squirmer with  $B_2 = 0$  have been recently performed [3]. In the latter work, we show that in viscoelastic fluid the power consumption decreases and efficiency increases. This implies an increment of the swimming speed at constant power. The present work therefore extends our previous investigation to consider the dynamics of pusher and puller squirmers.

Our results are obtained by finite-element discretization of the governing equations, where the Giesekus model with mobility factor 0.2 is used for the polymeric stress. A numerical stable and accurate model is built using the Discrete Elastic-Viscous Split Stress (DEVSS-G) algorithm introduced in [4, 5]. Galerkin approximation is used to discretize the momentum equations, continuity equation and the equation for the additional unknown  $\nabla \mathbf{u}$  with quadratic elements for  $\mathbf{u}$ , linear elements for  $p$  and  $\nabla \mathbf{u}$ . The streamline-upwind/Petrov-Galerkin method is used to discretize the constitutive equation for the polymeric stress. The finite-element framework is provided by the commercial software COMSOL.

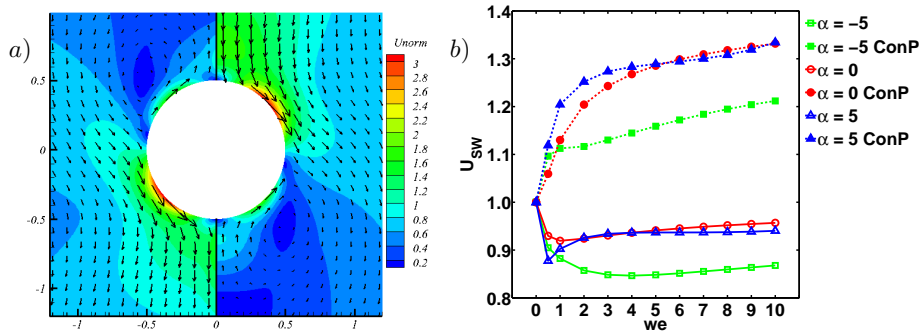


**Figure 1.** a) Typical flow field generated by a  $\alpha = -5$  pusher (Left) and a  $\alpha = 5$  puller (Right), in the co-moving frame. b) Swimming speed scaled to ensure constant power consumption versus the Weissenberg number,  $We$ , for viscosity ratio  $\beta = 0.5$ . Empty symbols represent the values of swimming speed at constant gait.

## RESULTS

A typical flow field generated by a pusher and a puller is shown in figure 1a), where the pusher is displayed on the left and the puller on the right half plane (note that we assume axisymmetric flow). A clear ring vortex appears in the front side of the pusher and in the back side of the puller. The swimming speed of squirmers with different gait is displayed in figure 1b) versus the Weissenberg number  $We$ . This adimensional parameter is proportional to the polymer relaxation time and to the elasticity of the suspension. The solid lines (empty symbols) indicate values obtained at fixed amplitude of the tangential deformation velocity. A decrease of the swimming speed is clear in this case, with pusher swimmers being the slowest. In all cases, however, we find a monotonic reduction of the power consumed with  $We$  and an increase in efficiency. It is therefore illustrative to display the swimming speed at fixed power (dashed lines and full symbols in 1b). All squirmers have now a velocity larger than that of their Newtonian counterpart. Swimmers with  $\alpha = 0$  and 5 are about 20% faster than pushers. Pullers are the fastest when  $We \approx 1$ .

## CONCLUDING REMARKS

Numerical simulations of spherical squirmers in viscoelastic fluid reveal that pullers are faster and more efficient than pushers. This is explained by the velocity induced by the body deformation: while pullers are able to push aside stretched polymers, they accumulate on the rear of the body in the case of pushers. In the final contribution, results will be presented for prolate swimmers; indeed most ciliated microorganisms have an elongated body.

## References

- [1] Lauga E., Powers T.R.: The hydrodynamics of swimming microorganisms. *Rep. Prog. Phys.* **72**:096601, 2009.
- [2] Blake J.R.: A spherical envelope approach to ciliary propulsion. *J. Fluid Mech* **46**:199–208, 1971.
- [3] Zhu L., Do-Quang M., Lauga E., Brandt L.: Locomotion by tangential deformation in a polymeric fluid. *Phys. Rev. E* **83**:011901, 2011.
- [4] Gunette R., Fortin M.: A new mixed finite element method for computing viscoelastic flows. *J. Non-Newtonian Fluid Mech.*, 60(1):27–52, 1995.
- [5] Liu A.W., Bornside, D.A., Armstrong R.C., Brown R.A.: Viscoelastic flow of polymer solutions around a periodic, linear array of cylinders: comparisons of predictions for microstructure and flow fields. *J. Non-Newtonian Fluid Mech.*, 77(3):153–190, 1998.

## **NUMERICAL STUDY OF FREE MOVING MICROORGANISMS WITH TWO FLAGELLA AT LOW REYNOLDS NUMBERS**

Ruth A. Lambert<sup>1</sup>, Luca Brandt<sup>1</sup>

*Linné Flow Centre, KTH Mechanics, S-100 44 Stockholm, Sweden*

### **INTRODUCTION**

A two-dimensional fluid and solid interaction (FSI) model of a microorganism with flagella that includes structural elasticity and fluid inertia has been developed. The flagella are treated as thin elastic filaments which are actuated by an internal strain mechanism. The fluid flow is solved using the Navier-Stokes' equations in order to address the role of inertia on the propulsion mechanism. The Reynolds number used to characterize the flow,  $Re = \omega_c l^2 / \nu$ , is based upon the characteristic length of the filament,  $l$ , and the forcing frequency  $\omega_c$ . A second important variable that characterizes the flow field is a dimensionless rigidity force,  $Sp = l(8\pi^2 \mu \omega_c / EI)^{0.25}$ , where  $\mu$  is the fluid viscosity,  $E$  is the modulus of elasticity, and  $I$  is the moment of inertia [1]. The  $Sp$  number relates the viscous drag to the elastic bending of the filaments. The numerical model is used to study the motion of a puller microorganism, such as *Chlamydomonas Reinhardtii*, with two flagella on the front of the body in the direction of motion. In the analysis, wall effects are included by considering confined motion in a narrow channel. Both experimental and numerical studies of unconstrained swimming of microorganisms with two flagella have been conducted [2, 3].

Numerical investigations of motion with flagella are generally limited to Stokes flow regime, since due to the small size, the Reynolds number based on the swimming speed is much less than unity. In addition to flow inertia, the elasticity of the filaments are also neglected since the elastic bending force in comparison to the actuation force is of higher order [4]. In spite of the small scale, a parametric analysis shows that localized inertial effects near the endpoints of the flagella may have an influence on locomotion. To illustrate, an increase in ciliar length from 10 to 300 microns results in an increase in the frequency  $Re$  number from 0.01–10 for an oscillation period of 10 ms and a fluid viscosity of order  $10^{-6}$  m<sup>2</sup>/s. The role of inertia is also an important factor in the development of artificial swimmers. The inertial effect can be determined by examining the swimming efficiency,  $\eta$ , and the swimming velocity,  $U$ , of a microorganism within this range of  $Re$ . The swimming efficiency,  $\eta$ , is the ratio of the power required to drag the body in the fluid with velocity  $U$  to the power generated by the swimmer [5]. The role of the elastic force in the solid equation satisfies the incompressibility constraint and restores the filament to the initial configuration when the actuation strain tends toward zero.

### **NUMERICAL METHODOLOGY**

The motion of the microorganism is modelled using the distributed Lagrange multiplier (DLM) method for solid body motion and thin elastic structures. The details of the method can be found in previous numerical studies for sedimenting particles and motion of moving elastic flaps [6, 7]. In the numerical method, the momentum equations for the fluid are solved using the finite volume method on a stationary grid. The motion of the body of the microorganism, represented in this case by a circular particle, is enforced by a rigidity constraint that conserves momentum. For the thin filaments, the continuous beam equations are solved on Lagrangian grid points using the finite difference method. The beam equations, used to solve for the surface velocity,  $\mathbf{u}$ , and displacement,  $\mathbf{x}$ , along the filament length, are described as,

$$\rho_s h \frac{d\mathbf{u}}{dt} = \mathbf{f}_e + \mathbf{f}_h + \mathbf{b} \quad (1)$$

$$\frac{d\mathbf{x}}{dt} = \mathbf{u} \quad (2)$$



where  $h$  is the filament thickness,  $\mathbf{f}_e$  is the force of elasticity,  $\mathbf{f}_h$  is the hydrodynamic force, and  $\mathbf{b}$  is an actuation force. The actuation force is generated by an internal strain, defined as  $\epsilon_a$ , which varies linearly across the filament cross section,  $h$ . The actuation strain has an axial variation along the length of the cilia,  $s$ , which is described by a function  $f(s)$ . The linear and axial variation of the strain results in bending moments that drive the motion of the cilia. The equation for the axial strain variation used in this study is  $f(s) = \sin(\pi/2s)$  where  $s$  varies from 0 to 1.

In the initial configuration, a circular body with diameter  $d$  is positioned in an open domain with height  $H = 16d$  and length  $L = 16d$  while the flagella length, taken from experimental data, is  $l = 1.6d$ . The actuation strain is independent of time and is reversed when the filaments open past a critical angle or are restored to a closed position. The horizontal velocity contours and streamlines for motion with two flagella in an open domain are shown in Fig. 1 at  $\text{Re} = 10^{-2}$  during one oscillation cycle. The flow field is axisymmetric with a squeeze flow visible between the two flagella. An analysis of the swimming speed for the moving objects in the figure shows a mean swimming speed of  $U/\omega_c l = -0.90$  for a dimensionless frequency of 0.92 and a maximum to minimum swimming velocity ratio of 1.4.

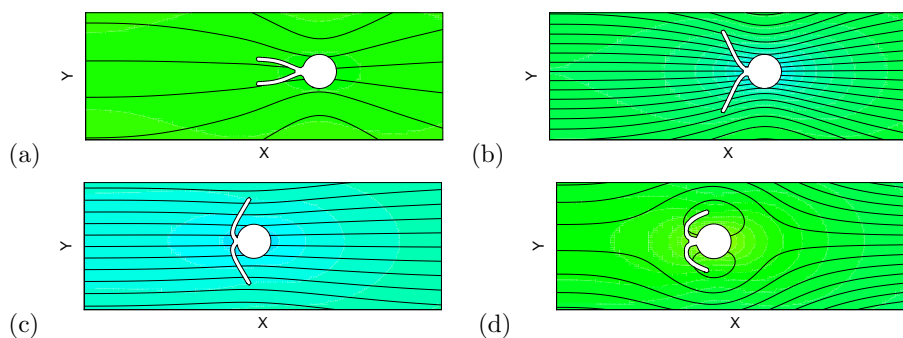


**Figure 1.** Horizontal velocity contours and streamlines for motion in an open domain at  $\text{Re} = 10^{-2}$  at (a)  $t^* = 0.2$ , (b)  $t^* = 0.4$ , (c)  $t^* = 0.6$ , and (d)  $t^* = 0.8$  where  $t^* = t\omega_c$ .

## CONCLUDING REMARKS

The initial results show that the FSI model developed in this study can be used to effectively describe the motion of swimmers with two cilia. For motion in an open channel, the influence of the walls reduce the average swimming speed in comparison to motion in an open domain. The influence of the Reynolds number on swimming efficiency and swimming speed ranging from  $10^{-2}$ –10 is also addressed.

## References

- [1] Alexeev A., Yeomans J.M., Balazs A.C.: Designing Synthetic, Pumping Cilia That Switch the Flow Direction in Microchannels. *Langmuir* **24**:12102–12106, 2008.
- [2] Guasto J.S., Johnson K.A., Gollub J.P.: Oscillatory Flows Induced by Microorganisms Swimming in Two Dimensions. *PRL* **105**:168102, 2010.
- [3] Tam D., Hosoi A.E.: Optimal Feeding and Swimming Gaits of Biflagellated Organisms. *PNAS* **108**:1001–1006, 2011.
- [4] Smith D.J.: A Boundary Element Regularized Stokeslet Method Applied to Cilia- and Flagella- Driven Flow. *Proc. R. Soc. A* **465**:3605–3626, 2009.
- [5] Spagnolie S.E., Lauga E.: The Optimal Elastic Flagellum. *Phys. Fluids* **22**:031901, 2010.
- [6] Ardekani A.M., Dabiri S., Rangel R.H.: Collision of Multi-particle and General Shape Objects in a Viscous Fluid. *J. Comp. Phys.* **227**:10094–10107, 2008.
- [7] Lambert R.A., Rangel R.H.: The Role of Elastic Flap Deformation on Fluid Mixing in a Microchannel. *Phys. Fluids* **22**:052003, 2010.

## FLUID-STRUCTURE INTERACTION OF MICRO-SWIMMERS

Thomas D. Johnson<sup>1</sup>, Daniel Loghin<sup>1</sup>, John R. Blake<sup>1</sup>, & David J. Smith<sup>1,2</sup>

<sup>1</sup> *School of Mathematics, University of Birmingham, Edgbaston, Birmingham, B15 2TT, United Kingdom*

<sup>2</sup> *School of Engineering, Centre for Scientific Computing, University of Warwick, Coventry, CV4 7AL, United Kingdom*

The study of eukaryotic flagellar motion has been a benchmark problem in low-Reynolds number flow for the past 60 years. It prompted the development of resistive force theory [2], as well as powerful singularity methods based upon the Stokeslet [3]. The Eukaryotic flagellum is one of the most evolutionarily robust structures in all of nature. Indeed, the motor apparatus of eukaryotic flagella, the axoneme, is almost identical in all organisms that possess it. Aside from being present in flagellated and ciliated microorganisms, it helps clear mucus from our lungs and is responsible for the breaking of left-right symmetry in the developing embryo [4]. The dysfunction of this organelle is the cause of a wide variety of medical conditions, from respiratory problems to *Situs Inversus* [1]. While much work until recently has focussed on flagella in Newtonian fluids, this focus has now shifted towards understanding their complex interaction with non-Newtonian fluids which, in certain cases, more accurately represent the environment of interest; for instance, the female reproductive tract for spermatozoa. These studies have shown that we need to revise our Newtonian intuition substantially in the presence of viscoelasticity. For instance, Purcell's famous 'Scallop Theorem' is invalidated [5], and recent work with mammalian sperm suggests that there may be an optimal Deborah number for efficient swimming [7].

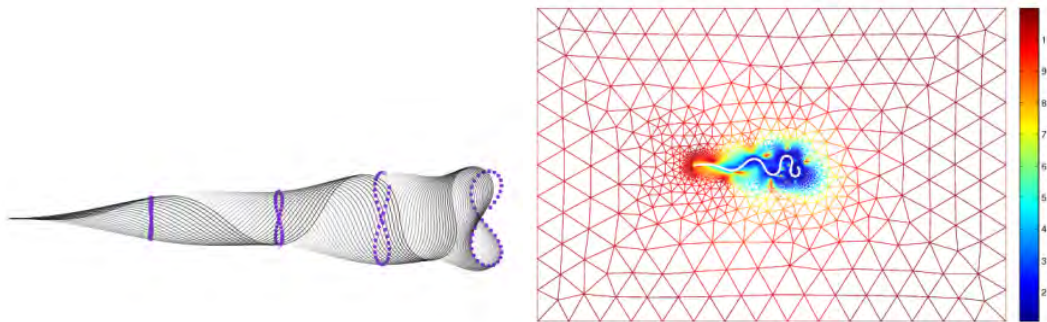


**Figure 1.** A time-lapse image of an experimentally observed high-viscosity flagellar waveform (left), and its corresponding effect on the viscosity of a regularised Bingham fluid (right), clearly showing a thin, liquified region around the swimmer with a solid outer-region due to the presence of a 'yield stress'. Adaptive mesh refinement, based on gradients of the viscosity, is used to accurately capture details of the flow. These include the solid 'pikes' in the liquified region, which result from the the interaction of the waveform with the fluid's rheology.

In our current model, results of which are shown in figure 1, experimental data are used to prescribe the flagellar waveform. These data are inputted into a custom mixed finite element code, and the resultant flow analysed for different generalised Newtonian rheologies, including Shear-thinning and regularised Bingham fluids. The code may be run in two or three dimensions, with adaptive mesh refinement utility available in two dimensions. We are currently working to extend the code to include viscoelastic rheologies.

A mixed finite element model of an active, free-swimming one-dimensional leaflet immersed in generalised Newtonian fluid is also in development. The flow will be assumed to be two-dimensional at zero Reynolds number. The leaflet will be modelled as a thin-walled elastic Kirchoff-Love beam, with its deformation governed by the principle of virtual displacements.

The discretisation will be realised using  $\mathcal{C}^1$ -continuous Cubic Hermite finite elements. The fluid flow will be solved on an adaptive ALE (arbitrary Lagrangian-Eulerian) moving mesh using the standard P2 elements for the velocity and P1 elements for the pressure. The fluid tractions on the leaflet will be given by a stress-jump across the wall, and the free-swimming constraints of zero net force and torque enforced with Lagrange multipliers.

Following the methodology of [6], beat analysis of human spermatozoa will be performed using custom software to capture and smooth the flagellar beat cycle. This experimental data will be inputted into the finite element code, and the resultant fluid flow, swimming velocity and beam stress analysed. Finally, an active bending wave will be specified in the beam, and the resultant waveform analysed for different rheologies.

This methodology will be applied to investigate the internal forces in the flagellum and associated theories of beat control. Furthermore, it is hoped that the work will be extended into three-dimensions, incorporating visco-elastic rheologies in the future. The inherent flexibility of this finite element framework will also admit applications in other areas of biofluid-structure interaction, such as lymphatic peristalsis, transport in the colon and microcirculation of blood.

## References

- [1] B. A. Afzelius. A human syndrome caused by immotile cilia. *Science (New York, NY)*, 193(4250):317–319, 1976.
- [2] J. Gray and G. J. Hancock. The propulsion of sea-urchin spermatazoa. *J. of Experimental Biology*, 1955.
- [3] R.E. Johnson and C.J. Brokaw. Flagellar hydrodynamics. a comparison between resistive-force theory and slender-body theory. *Biophys. J.*, 25(1), 1979.
- [4] S. Nonaka, H. Shiratori, Y. Saijoh, and H. Hamada. Determination of left–right patterning of the mouse embryo by artificial nodal flow. *Nature*, 418(6893):96–99, 2002.
- [5] T. Normand and E. Lauga. Flapping motion and force generation in a viscoelastic fluid. *Phys. Rev. E*, 78(6):061907, Dec 2008.
- [6] D.J. Smith, E.A. Gaffney, H. Gad elha, N. Kapur, and J. C. Kirkman-Brown. Bend propagation in the flagella of migrating human sperm, and its modulation by viscosity. *Cell Motil. Cytoskel.*, 66:220–236, 2009.
- [7] J. Teran, L. Fauci, and M. Shelley. Viscoelastic fluid response can increase the speed and efficiency of a free swimmer. *Phys. Rev. Lett.*, 104, 2010.

## BENDING MOMENT EFFICIENCY OF SPERM MOTILITY

David J. Smith<sup>13</sup>, Eamonn A. Gaffney<sup>23</sup>, Hermes Gadêlha<sup>235</sup> & Jackson Kirkman-Brown<sup>34</sup>

<sup>1</sup> School of Mathematics, University of Birmingham, U.K.

<sup>2</sup> Centre for Mathematical Biology, Mathematical Institute, University of Oxford, U.K.

<sup>3</sup> Centre for Human Reproductive Science, Birmingham Women's NHS Foundation Trust, Birmingham, U.K.

<sup>4</sup> Clinical and Experimental Medicine, University of Birmingham, U.K.

<sup>5</sup> The CAPES Foundation, Ministry of Education of Brazil, Brasilia, Brazil

A wide array of cells, from single-celled eukaryotes, to the gametes of higher animals and plants, achieve motility through fluids by means of propagating bending waves along a single flagellum. Cell motility generally takes place in the very low Reynolds number regime, in which inertia is negligible compared with viscosity. In Newtonian liquids such as saline, the flow can be modelled mathematically by the Stokes flow equations,

$$\mu \nabla^2 \mathbf{u} = \nabla p, \quad \nabla \cdot \mathbf{u} = 0, \quad (1)$$

where  $p$  is pressure,  $\mathbf{u}$  is velocity and  $\mu$  is dynamic viscosity. The first equation corresponds to momentum balance, the second to mass conservation and incompressibility.

The issue of kinematic optimality of very low Reynolds number swimming has been addressed by a number of authors, notably Lighthill [4], with a recent resurgence of interest in the field ([9, 8, 1, 10] to give just a sample). This topic was recently reviewed by Lauga & Powers [3]; advances in the optimization problem which take into account flagellar elasticity have been made by Spagnolie & Lauga [7]. We focus on the unflagellate case, which describes the mammalian, and specifically human sperm [2]. These cells have evolved to swim through highly viscous fluids such as cervical mucus, and in order to do this, perform a characteristic form of flagellar beating which is not exhibited by evolutionary marine ancestors. The change in flagellar beating subject to under physiological high viscosity is shown in Figure 1(a,b). Sperm swimming is likely to impose a competitive pressure for cells to progress rapidly, subject to the constraints imposed by the female reproductive tract.

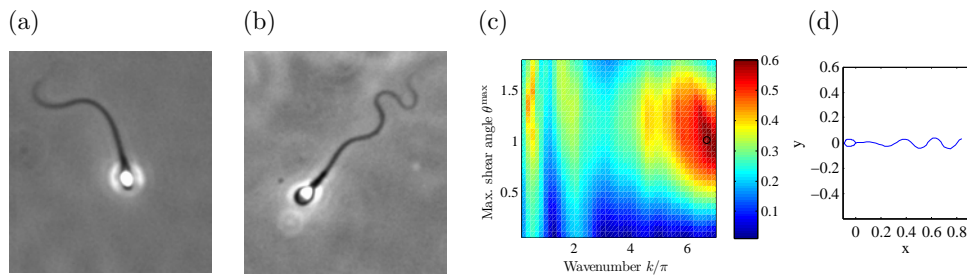


**Fig. 1.** Micrographs of migratory human sperm in (a) laboratory saline, (b) medium with increased viscosity (0.14 Pa.s, from oscillatory rheometry data), showing the modulation of curvature resulting in a characteristic ‘meandering’ waveform. (c) Fitness space and (d) optimal solution for velocity scaled with respect to squared bending moment for our parameter set and search space, suggesting that ‘meandering’ beating may have competitive advantages.

Most studies have searched spaces of kinematic wavforms, optimising the ‘inverse efficiency’ considered by Lighthill, essentially the square of mean swimming speed divided by mean rate of working,  $\eta = \frac{\bar{U}^2}{P}$ . We shall consider a different optimum: what is the fastest a cell can swim, subject to a maximum magnitude of internal actuation? This corresponds to the fact that the

dynein motors in the evolutionary-conserved axoneme structure have a fixed density and will be limited in the sliding force they can product.

Sperm swimming is modelled using the boundary integral/slender body theory method [6].

$$\begin{aligned}\mathbf{u}(\mathbf{x}) &= \mathbf{u}_{\text{head}}(\mathbf{x}) + \mathbf{u}_{\text{tail}}(\mathbf{x}) \\ &= \iint_{\partial H} \mathbf{S}(\mathbf{x}, \mathbf{Y}) \cdot \boldsymbol{\phi}(\mathbf{Y}) \, d\mathbf{Y} + \int_0^L \mathbf{G}(\mathbf{x}, \mathbf{X}(s)) \cdot \mathbf{f}(s) \, ds,\end{aligned}\quad (2)$$

where  $\mathbf{S}$  is the Stokeslet velocity tensor, and  $\mathbf{G}$  is a combined Stokeslet–potential dipole singularity used to improve the accuracy of the slender body theory. The flagellar motion is prescribed with respect to the cell body,  $\mathbf{X} = \mathbf{X}^H + \mathbf{M} \cdot \mathbf{X}'$ ,  $\mathbf{U} = \mathbf{U}^H + \boldsymbol{\Omega} \wedge (\mathbf{X} - \mathbf{X}^H) + \mathbf{M} \cdot \mathbf{U}'$ , where  $\mathbf{X}^H$  is head centroid,  $\mathbf{X}'$  is flagellar position with respect to the head, with analogous velocities  $\mathbf{U}$  and  $\mathbf{U}'$ , the angular velocity of the cell is  $\boldsymbol{\Omega}$  and  $\mathbf{M}$  is a rotation matrix defining the cell orientation. This forms a system of equations for the unknowns  $\mathbf{U}^H$ ,  $\boldsymbol{\Omega}$  and the force density/tractions  $\boldsymbol{\phi}(\mathbf{Y})$ ,  $\mathbf{f}(s)$ . These equations are solved numerically over 100 timesteps defining a flagellar beat to determine the mean swimming velocity and peak viscous bending moment density.

The prescribed space of flagellar motions is parameterised by wavelength and maximum ‘shear angle’ with respect to the head of the cell. Both bending and shear elasticity are taken into account. The viscous bending moment density at arclength  $s$ , denoted  $m^{\text{hyd}}(s)$ , is calculated from the equations,  $\mathbf{F} = \int_s^L \mathbf{f}(s) \, ds$  and  $m^{\text{hyd}}(s) = \mathbf{n}(s) \cdot \mathbf{F}$ , where  $\mathbf{n}(s)$  is unit normal in the beat plane. The active shear moment  $\hat{m}^{\text{act}}$  is estimated from its balance with viscous, elastic bending and passive shear moments. Using this relation combined with the hydrodynamic calculations, and estimates for bending and shear stiffness [5] we can then calculate the bending moment ‘fitness’,

$$\phi = \frac{\bar{U}}{\max_{0 < s < L, 0 < t < T} |\hat{m}^{\text{act}}|}.\quad (3)$$

The optimal solution shown in Figure 1(c,d) suggests that for characteristic viscosity and elastic parameters, ‘meandering’ waves may confer competitive advantages. We are currently working on modelling approaches that will allow consideration of viscoelastic effects and the internal flagellar structure. The fluid dynamic propulsion of the sperm cell continues to be a stimulating subject for fluid dynamicists and mathematicians.

## References

- [1] H.C. Fu, C.W. Wolgemuth, and T.R. Powers. Swimming speeds of filaments in nonlinearly viscoelastic fluids. *Phys. Fluids*, 21:033102, 2009.
- [2] E.A. Gaffney, H. Gad elha, D.J. Smith, J.R. Blake, and J. Kirkman-Brown. Mammalian sperm motility: observation and theory. *Annu. Rev. Fluid Mech.*, In press: doi:10.1146/annurev-fluid-121108-145442, 2011.
- [3] E. Lauga and T. R. Powers. The hydrodynamics of swimming microorganisms. *Rep. Prog. Phys.*, 72:096601, 2009.
- [4] M.J. Lighthill. *Mathematical biofluidynamics*. SIAM, 1975.
- [5] D.W. Pelle, C.J. Brokaw, K.A. Lesich, and C.B. Lindemann. Mechanical properties of the passive sea urchin sperm flagellum. *Cell Motil. Cytoskel.*, 66:721–735, 2009.
- [6] D.J. Smith, E.A. Gaffney, J.R. Blake, and J.C. Kirkman-Brown. Human sperm accumulation near surfaces: a simulation study. *J. Fluid Mech.*, 621:220–236, 2009.
- [7] S.E. Spagnolie and E. Lauga. The optimal elastic flagellum. *Phys. Fluids*, 22:031901, 2010.
- [8] D. Tam. *Motion at low Reynolds number*. PhD thesis, Massachusetts Institute of Technology, 2008.
- [9] D. Tam and A.E. Hosoi. Optimal stroke patterns for Purcells three-link swimmer. *Phys. Rev. Lett.*, 98(6):68105, 2007.
- [10] J. Teran, L. Fauci, and M. Shelley. Viscoelastic fluid response can increase the speed and efficiency of a free swimmer. *Phys. Rev. Lett.*, 104:38101, 2010.

## LEFT-RIGHT SYMMETRY BREAKING: VESICLE TRANSPORT DUE TO WHIRLING CILIA IN THE EMBRYONIC NODE

Andrew A. Smith<sup>1</sup>, Thomas D. Johnson<sup>1</sup>, David J. Smith<sup>1,2</sup> & John R. Blake<sup>1</sup>

<sup>1</sup> School of Mathematics, University of Birmingham, Edgbaston, Birmingham, B15 2TT, United Kingdom

<sup>2</sup> School of Engineering, Centre for Scientific Computing, University of Warwick, Coventry, CV4 7AL, United Kingdom

Left-right symmetry breaking is crucial to vertebrate embryonic development. This is because in many species the egg upon fertilisation is symmetric yet the resulting internal body plan is asymmetric [4], for example in humans the heart is on the left and the liver is on the right. See figure 1. The symmetry breaking event is a result of a left directional fluid flow, termed a ‘nodal flow’, generated by whirling cilia at early stages of development.

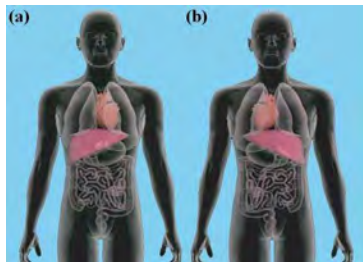


Figure 1. (a) Normal *situs*. (b) *Situs inversus*, affects < 1% of humans [4].

In many species this event begins in a region of the embryo termed the ‘node’ in the mouse and the ‘Kupffer’s vesicle’ in the zebrafish. The node develops at approximately 7–9 days post-fertilisation for the mouse.

An initial model was developed based on the geometry of the mouse node, an approximately triangular region that forms on the ventral side of the developing embryo. See figures 2(a) and 2(b). The mouse node contains a single ciliated surface on the dorsal wall that are tilted towards the posterior [1, 2]. These cilia are rotating clockwise, when viewed from tip to base, generating a flow field that transports vesicle particles. See figure 2(b) and 2(c).

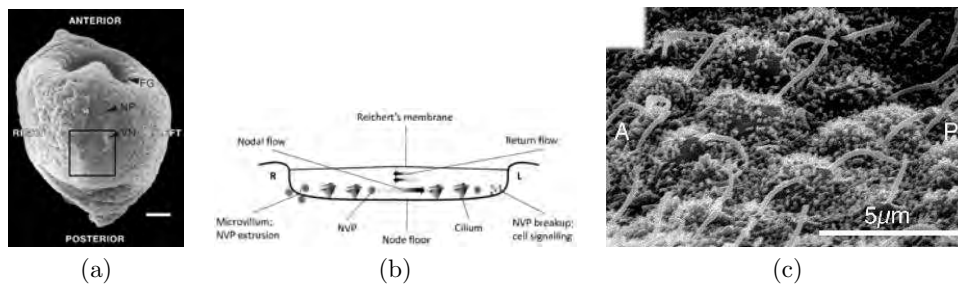


Figure 2. (a) Low-magnification view of a mouse embryo at 7.5 days post-fertilisation, node indicated by ‘VN’ [4]. (b) Schematic section of the node cavity viewed from the posterior [8]. (c) Scanning electron micrograph of the wild-type node [6].

The mouse node is a low Reynolds number system allowing the use of singularities of Stokes flow, slender body theory and the single layer boundary element method to explain how rotation and posterior tilt contribute to a directional fluid flow. This method is highly efficient allowing the simulation of a three-dimensional flow field for tens of thousands of time steps. Simulations of the mouse node predict a range of fluid flow characteristics depending on the proximity to cilia and bounding surfaces and the configuration of the cilia. See figure 3(a). Particles take a ‘loopy’ drift motion to the ‘left’. ‘Loopy’ near the cilia with a leftward drift in between before joining the upper return flow. It is likely that the motion is chaotic.

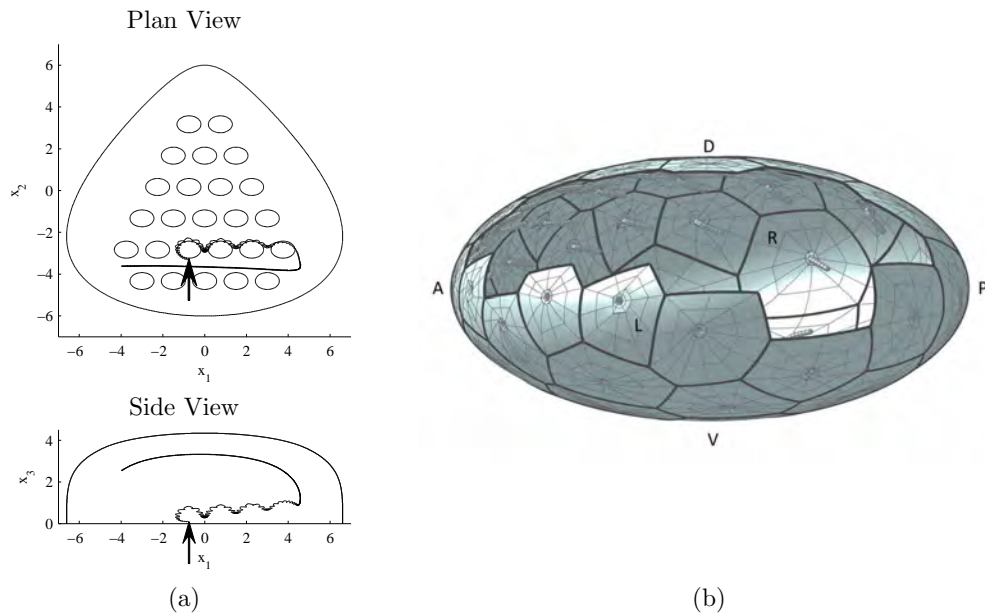


Figure 3. (a) Particle started at  $(-0.75, -3.25, 0.10)$ . A leftward fluid flow is observed across the cilia and a rightward return flow close to the roof of the node [8]. (b) Three-dimensional mesh used to model the cilia as part of the boundary mesh in the zebrafish, axis notation A, anterior; P, posterior; D, dorsal; V, ventral; L, left and R, right.

We are currently developing a model to analyze the zebrafish Kupffer's vesicle. The Kupffer's vesicle has cilia lining the dorsal roof and the ventral floor [3, 5, 7]. The Kupffer's vesicle is modelled again using regularised singularities of Stokes flow and the single layer boundary element method. The cilia in the Kupffer's vesicle are modelled using a three-dimensional mesh incorporated into the boundary mesh that takes into account cell curvature for the first time. See figure 3(b). Flow fields in the Kupffer's vesicle depend upon the number of cilia and their distribution in the vesicle giving rise to different flow types [9]. These new results will be presented at the meeting.

## References

- [1] J. H. E. Cartwright, N. Piro, O. Piro, and I. Tuval, *Embryonic nodal flow and the dynamics of nodal vesicular parcels*, *Journal of The Royal Society Interface* **4** (2007), no. 12, 49–55.
- [2] J. H. E. Cartwright, O. Piro, and I. Tuval, *Fluid-dynamical basis of the embryonic development of left-right asymmetry in vertebrates*, *Proceedings of the National Academy of Sciences* **101** (2004), no. 19, 7234–7239.
- [3] J.J. Essner, J.D. Amack, M.K. Nyholm, E.B. Harris, and H.J. Yost, *Kupffer's vesicle is a ciliated organ of asymmetry in the zebrafish embryo that initiates left-right development of the brain, heart and gut*, *Development* **132** (2005), no. 6, 1247.
- [4] N. Hirokawa, Y. Okada, and Y. Tanaka, *Fluid Dynamic Mechanism Responsible for Breaking the Left-Right Symmetry of the Human Body: The Nodal Flow*, *Annual Review of Fluid Mechanics* **41** (2009), 53–72.
- [5] A. G. Kramer-Zucker, F. Olale, C. J. Haycraft, B. K. Yoder, A. F. Schier, and I. A. Drummond, *Cilia-driven fluid flow in the zebrafish pronephros, brain and Kupffer's vesicle is required for normal organogenesis*, *Development* **132** (2005), no. 8, 1907–1921.
- [6] S. Nonaka, S. Yoshida, D. Watanabe, S. Ikeuchi, T. Goto, W. F. Marshall, and H. Hamada, *De novo formation of left-right asymmetry by posterior tilt of nodal cilia*, *PLoS Biology* **3** (2005), no. 8, 1467–1472.
- [7] N. Okabe, B. Xu, and R. D. Burdine, *Fluid dynamics in zebrafish Kupffer's vesicle*, *Developmental Dynamics* **237** (2008), no. 12, 3602–3612.
- [8] D. J. Smith, A. A. Smith, and J. R. Blake, *Mathematical embryology: the fluid mechanics of nodal cilia*, *Journal of Engineering Mathematics* (2011).
- [9] W. Supatto, S. E. Fraser, and J. Vermot, *An all-optical approach for probing microscopic flows in living embryos*, *Biophysical Journal* **95** (2008), no. 4, 29–31.

## BACTERIA-INSPIRED MICROROBOTS FOR NON-CONTACT MANIPULATION

Kathrin E. Peyer, Li Zhang & Bradley J. Nelson

*Institute of Robotics and Intelligent Systems, ETH Zurich, Tannenstrasse 3, Ch-8092 Zurich*

### INTRODUCTION

Swimming microrobots have the potential to be used for *in vitro* manipulation and investigation of cells or micro-objects and as an *in vivo* diagnostic and therapeutic tool. The development of swimming microrobots faces a number of challenges including the fabrication of micro-agents, wireless power supply, and locomotion methods suitable for a low Reynolds (Re) number regime. The difficulty is enhanced as these challenges can almost never be tackled separately and therefore have to be assessed as a complete microrobotic system. In nature microorganisms have found numerous locomotion methods, such as cilia or flexible beating flagella, suitable for navigation at low Re numbers. The artificial bacterial flagellum (ABF) is a swimming microrobot that mimics the propulsion method of bacteria, such as *E. coli*, by using a rotating helical tail for motion generation (see Fig. 1). An external rotating magnetic field is used as a power supply. The ABF is a microrobot prototype capable of navigation in 3D, creating sufficient propulsive force to overcome its weight in water, and is capable of pushing and rotating micro beads by contact manipulation. A direct contact may, however, be harmful when working with living cells and we will discuss the approach of using local flow fields generated by an ABF to move objects in a non-contact manner.

### MICROROBOTIC SYSTEM

When engineering microrobotic systems, efficiency is an important factor as power supply is difficult and limited. Rotating a helical tail is not very efficient from a fluidic propulsion point of view [1], the definition of efficiency can, however, be misleading when taking into account the magnetic actuation of the microrobots. Evaluating the microrobotic system as a whole, considering both fluid mechanics and magnetic actuation, helical swimming is one of the most promising methods of propulsion for microrobots [2].

#### Locomotion, fabrication and actuation

The linear relationship between the forward and rotational velocity,  $u$  and  $\omega$  respectively, of a helical filament under the influence of an external force  $F$  and torque  $T$  can be represented by a  $2 \times 2$  *propulsion* matrix.

$$\begin{pmatrix} F \\ T \end{pmatrix} = \begin{pmatrix} a & b \\ b & c \end{pmatrix} \begin{pmatrix} u \\ \omega \end{pmatrix} \quad (1)$$

The parameters  $a$ ,  $b$  and  $c$  are functions of geometrical parameters only and can be found by modeling or empirical methods. The rotation and translation of a helical filament are inherently coupled, i.e.  $b \neq 0$ , due to the lack of a shape symmetry. This coupling is exploited by using a torque to rotate the filament, which in turn creates the desired translational motion.



**Figure 1.** Locomotion model of an artificial bacterial flagellum (ABF).

Using an external magnetic field to apply the required torque to the ABF removes the need to



replicate the highly complex molecular rotary motor of real bacteria [3]. The challenge remains in fabricating the helical tail, which is a non-trivial 3D structure, at a micro scale. The first method to successfully fabricate ABFs in a batch process is the self-scrolling technique [4]. The controlled release of internal stresses in the material allows arrays of ribbons to roll-up into helical shapes. The prototypes described here have a helical tail with an overall length of 30 – 100  $\mu\text{m}$ , depending on the number turns, and a diameter of 2.8  $\mu\text{m}$ . The tail is attached to a 200 nm thin and 4.5  $\mu\text{m}$  wide square plate made from a soft-magnetic material.

A magnetic body whose direction of magnetization is deviated from the direction of the external field experiences a magnetic torque which rotates the body until it becomes aligned. In order to create a continuous rotation of the ABF around its helical axis, the external field has to be rotated as well, which is achieved with individually controlled electromagnetic coil pairs placed around the ABF.

### NON-CONTACT MANIPULATION

The ABF can be steered in micrometer precision towards a target and experimental results showing the pushing and rotating of micro beads have been presented in previous publications [4]. The use of real micro-organisms for micromanipulation tasks has already been explored in literature [5] but this approach requires a controlled environment that can sustain microbial life. Micro-robots have, therefore, the potential to be applied in more diverse tasks and conditions. This project explores the flow field created by ABFs and how it can be used to move micro-objects. Figure 2 shows an ABF steered into a vertical position where it has to create a propulsive force to overcome its weight in water. A rotational speed exists at which forces are at an equilibrium and the ABF hovers with zero translational motion. The rotational flow field induced by the ABF can be used to manipulate micro-object without physical contact, which is beneficial when considering the transportation of living cells. Figure 2 shows a spike of dye being transported around the ABF at a safe distance of approximately 20  $\mu\text{m}$ .

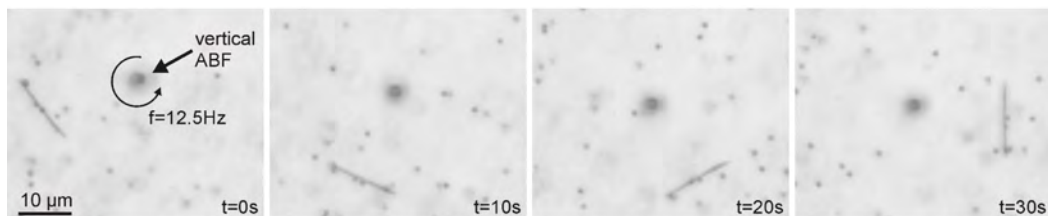


**Figure 2.** Contact-free manipulation of a micro-spike by an ABF-induced flow field. The ABF is vertically orientated and its location and direction of rotation are indicated by arrows.

### CONCLUSIONS

Preliminary results show that current ABF prototypes are capable of local flow generation which can be used for non-contact manipulation of micro-objects. Micro-objects can potentially be transported along more complex motion paths by introducing additional boundaries, which guide or deviate the flow generated by the ABF, or by servoing.

### References

- [1] Purcell E. M.: Life at Low Reynolds Number. *Am. J. Phys.* **45**:3–11, 1977.
- [2] Abbott J. J. et al.: How Should Microrobots Swim?. *Int. J. Robotics Research* July, 2009.
- [3] Berg H. C.: The rotary motor of bacterial flagella. *Annu. Rev. Biochem.* **72**:19–54, 2003.
- [4] Zhang L., Peyer, K. E., Nelson B. J.: Artificial bacterial flagella for micromanipulation. *Lab chip*, **10**:2203–15, 2010.
- [5] Itoh A.: Motion Control of Protozoa for Bio MEMS. *IEEE-ASME T. Mech.*, **5**:181-188, 2000.

## EXPERIMENTAL INVESTIGATION OF THE FLOW INDUCED BY ARTIFICIAL CILIA

J. Hussong<sup>1</sup>, N. Schorr<sup>2</sup>, J. Belardi<sup>2</sup>, O. Prucker<sup>2</sup>, J. R uhe<sup>2</sup> & J. Westerweel<sup>1</sup>

<sup>1</sup> *Laboratory for Aero and Hydrodynamics, Delft University of Technology, Leeghwaterstraat 21, 2628 CA Delft, The Netherlands*

<sup>2</sup> *University of Freiburg-IMTEK, Department of Microsystems Engineering, Laboratory for Chemistry and Physics of Interfaces, Georges-Koehler-Allee 103, 79110 Freiburg, Germany*

### INTRODUCTION

The rapid development of miniaturization in bio-medical analysis and other applications generates a growing need for alternative methods of manipulating fluids on sub-millimeter scales. In nature there exist very efficient ways to mechanically pump fluids in micron sized tubes, such as by the beating of so-called cilia. Cilia are micron sized, wall-attached hair-like cell extensions. Inspired by nature, Cilia-like structures of micrometer scale were successfully produced and actuated by several groups [7, 2, 8, 5] and first fluid manipulation of artificial cilia immersed in water could be shown [10, 3]. Recently, net flows in a micro channel were shown with maximum fluid velocities of almost  $5 \mu\text{m/s}$  by [9] and up to approximately  $9 \mu\text{m/s}$  by [6].

In this paper we report on studies of the flow induced by artificial cilia that produce more than 10 times higher flow rates in a micro channel. The cilia consist of superparamagnetic (spm) micro-beads embedded in a polymer and can be actuated magnetically [1]. We apply an external rotating magnetic field that induces a non-symmetric, planar motion of the cilia. The phase averaged and time resolved flow is quantified by means of phase-locked  $\mu\text{PIV}$  measurements.

### RESULTS

The fluid transport produced by rectangular shaped, magnetically actuated artificial cilia [1] was determined by means of phase-locked Micro Particle Image Velocimetry ( $\mu\text{PIV}$ ) measurements in a closed flow volume. The cilia perform two beat cycles during a full revolution of the magnetic field. A representative vector field of the effective stroke is shown on the left hand side of Fig.1. The resulting median velocities of each vector field are shown in the middle graph of Fig.1 for actuation frequencies up to 20 Hz. The right hand side curve of Fig.1 shows the cilia-induced velocity distribution over the channel height. Since the micro channel was closed at the in- and outlet, the flow induced by the cilia at the lower half of the channel is compensated by a backflow in the upper channel half. We approximate the velocity profile as the sum of a cilia-induced plane Couette flow in positive x-direction and a back pressure-induced plane Poiseuille flow in negative x-direction. From the equation system of the measured velocity profile and its first derivative we derive the pressure gradient  $\nabla p$  and the velocity  $U$  of the Couette flow at the channel bottom as well as the cilia- and the back pressure-induced volume flow rates to  $\dot{V}_p = -16 \pm 3.6 \frac{\mu\text{l}}{\text{min}}$  and  $\dot{V}_c = 13.6 \pm 3.9 \frac{\mu\text{l}}{\text{min}}$ , respectively.

### CONCLUSIONS

The fluid transport produced by rectangular shaped, magnetically actuated artificial cilia [1] was determined by means of phase-locked Micro Particle Image Velocimetry ( $\mu\text{PIV}$ ) measurements in a closed flow volume. The achieved velocities are one order of magnitude higher than in previous studies [6, 9], reaching values that are comparable with other microfluidic transport mechanisms such as electro-osmotic pumping. Analysis of the measured flow data indicate that the present system is capable of achieving volume flow rates of  $\dot{V}_{cilia} = 14 \pm 4 \mu\text{l}/\text{min}$  when no back pressure is built up in the micro channel with a cross section of  $0.5 \times 5 \text{mm}^2$ . This corresponds to an

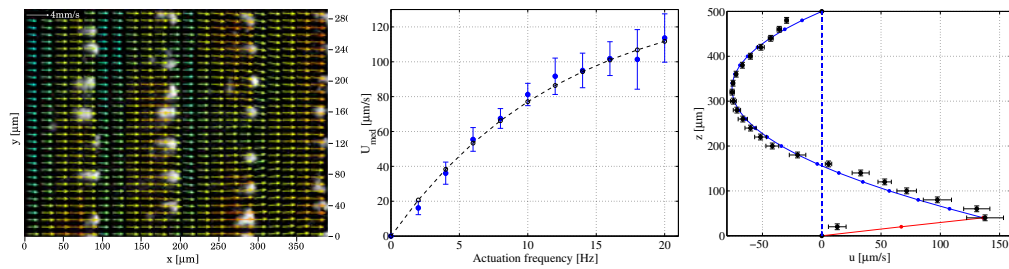


**Figure 1.** Left: Velocity field during the cilia effective stroke (10 Hz actuation). Superimposed is the averaged image data of the cilia. Middle: Median phase averaged fluid velocities are plotted as a function of frequency. Right: Phase averaged velocity distribution over the channel height in a closed channel configuration. The cilia-induced flow is counterbalanced by a pressure driven backflow.

effective pressure gradient of  $6 \pm 1 \text{ Pa/m}$ , which equals a pressure difference of  $0.6 \pm 0.1 \text{ mPa}$  over a distance of  $100 \mu\text{m}$  between two rows of cilia. These results were derived analytically from the measured velocity profile allowing to also compute the accuracy of the calculated pressure drop and volume flow rate. While the cilia produce phase averaged velocities of the order of  $\mathcal{O}(10^2 \mu\text{m/s})$ , time resolved measurements showed that the flow field reverses two times during one actuation cycle inducing instantaneous velocities of up to  $|v| \approx 2 \text{ mm/s}$ . This shows that the flow field is dominated by fluid oscillations and flow rates are expected to increase if the beating motion of the cilia is further improved.

#### ACKNOWLEDGMENT

This work is a part of the European project ARTIC, under Contract No. STRP 033274, and initiated by Jaap den Toonder (Philips). The microfluidic channel and the magnetic actuation system were produced by Bogdan Craus (Philips).

#### References

- [1] BELARDI, J. & SCHORR, N. & PRUCKER, O. & RHE, J. 2011 Artificial Cilia: Generation of Magnetic Actuators in Microfluidic Systems. *Submitted*.
- [2] EVANS, B.A. & SHIELDS, A.R. & LLOYD CARROLL, R. & WASHBURN, S. & FALVO, M.R. & SUPERFINE, R. 2007. Magnetically Actuated Nanorod Arrays as Biomimetic Cilia *NANO LETTERS* **7**, 5, 1428-1434.
- [3] FAHRNI, F. & PRINS, M. & VAN IJZENDOORN, L. 2009 Micro-fluidic actuation using magnetic artificial cilia. *Lab Chip* **9**, 3413-3421.
- [4] KHADERI, S. N. & CRAUS, C. & HUSSONG, J. & SCHORR, N. & BELARDI, J. & WESTERWEEL, J. & PRUCKER, O. & RUEHE, J. & DEN TOONDER, J. M. J. & ONCK, P. R. 2011 Magnetically-actuated artificial cilia for microfluidic propulsion. *Lab Chip submitted*.
- [5] OH, K. & CHUNG, J.-H. & DEVASIA, S. & RILEY, J. J. 2009 Bio-mimetic silicone cilia for microfluidic manipulation. *Lab Chip* **9**, 1561-1566.
- [6] SHIELDS, A.R. & FISER, B.L. & EVANS, B.A. & FALVO, M.R. & WASHBURN, S. & SUPERFINE, R., 2010 Biomimetic cilia arrays generate simultaneous pumping and mixing regimes *PNAS* **107**, 36, 15670-15675.
- [7] SINGH, H. & LAIBINIS, P. E. & HATTON, T. A. 2005 Synthesis of flexible magnetic nanowires of permanently linked core-shell magnetic beads tethered to a glass surface patterned by microcontact printing. *Nano Lett.* **5**, 2149-2154.
- [8] VAN OOSTEN, C.L. & BASTIAANSEN, C.W.M. & BROER, D.J. 2009 Printed artificial cilia from liquid-crystal network actuators modularly driven by light. *Nature Materials* **8**, 677-682.
- [9] VILFAN, M. & POTOCNIK, A. & KAVCIC, B. & OSTERMAN, N. & POBERJAJ, I. & VILFAN, A. & BABIC, D. 2009 Self assembled artificial cilia. *PNAS* **5**, 1844-1847.
- [10] DEN TOONDER, J. & BOS, F. & BROER, D. & FILIPPINI, L. & GILLIES, M. & DE GOEDE, J. & MOL, T. & REIJME, M. & TALEN, W. & WILDERBEEK, H. & KHATAVKAR, V. & ANDERSON, P. 2008 Artificial cilia for active micro-fluidic mixing. *Lab Chip* **8**, 533-541, 4.

## **LOW-REYNOLDS-NUMBER FLOW BETWEEN TWO VESSELS WITH A SHUNT BETWEEN THEM**

Adriana Setchi<sup>1</sup>, Jonathan Mestel<sup>2</sup>, Jennifer Siggers<sup>1</sup> & Kim Parker<sup>1</sup>

<sup>1</sup> *Department of Bioengineering, Imperial College London, SW7 2AZ London*

<sup>2</sup> *Department of Mathematics, Imperial College London, SW7 2AZ London*

### **INTRODUCTION**

There are many shunts in the human circulatory system. This work aims to construct matched Papkovich-Fadle-eigenfunction expansions for the solution of flow between two channels. Such a solution can be applied to model side-to-side anastomoses (surgical connections between blood vessels or segments of gut), or fistulas between arteries and veins (e.g. during hemodialysis). Papkovich-Fadle functions were first used in elastic theory [1]. Many problems have been solved in this manner since then including slow flow over slots [2], cavities [3] or through constrictions [4]. These can be applied to model biological problems such as aneurysms, atherosclerosis or vasoconstrictions.

### **MATHEMATICAL FORMULATION**

This work considers a non-Newtonian and incompressible fluid in a two-dimensional geometry of two similar infinite channels with a shunt between them as shown in Figure 1.

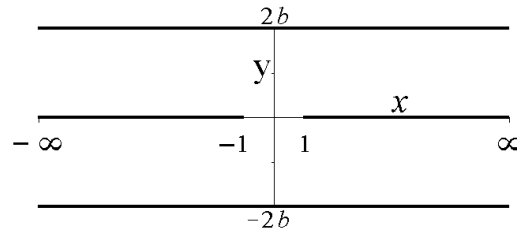


**Figure 1.** Geometry of two channels with a shunt between them

These assumptions make it possible to simplify the Navier-Stokes equations to the system

$$-\nabla p + \mu \nabla^2 \underline{u} = 0 \quad \text{and} \quad \nabla \cdot \underline{u} = 0. \quad (1)$$

By defining a streamfunction  $\Psi(x, y)$  such that  $u = \frac{\partial \Psi}{\partial y}$  and  $v = -\frac{\partial \Psi}{\partial x}$  these simplify further to a single biharmonic equation

$$\nabla^4 \Psi = 0. \quad (2)$$

No-slip boundary conditions  $\left\{ \frac{\partial \Psi}{\partial n} = 0, \Psi = \text{const} \right\}$  are imposed on all solid boundaries. In addition, Poiseuille flow is prescribed at  $x = \pm\infty$ .

Note that the equation is linear and steady. It is possible to construct time-dependent solutions by adding steady solutions instantaneously. This can be done using time-dependent boundary conditions at infinity such as clinical pressure or flux measurements. The next section explains the derivation of the three linearly independent steady solutions for this geometry.

### **STEADY SOLUTIONS**

The biharmonic equation  $\nabla^4 \Psi = 0$  is not uniquely solved using separation of variables. Progress can be made by dividing the geometry into subregions. For each of these the boundary conditions determine the Papkovich-Fadle eigenfunction expansions. Consider one steady solution driven by Poiseuille flow at all channel ends (Figure 2). Due to symmetry,  $\Psi$  is even in  $x$  and odd in  $y$ . The expansions for regions 1 and 2 are chosen to be

$$\Psi_1 = y^2 \left( b - \frac{y}{3} \right) + \sum_{n=1}^{\infty} A_n e_2^n(y) e^{\frac{K_n}{b}(x+1)} + \sum_{n=1}^{\infty} B_n e_1^n(y) e^{\frac{k_n}{b}(x+1)} \quad \text{for } x \in (\infty, -1) \cup y \in (0, 2b) \quad (3)$$

$$\Psi_2 = y^2 \left( b - \frac{y}{3} \right) + \sum_{n=1}^{\infty} C_n e_2^n(y) \frac{\cosh\left(\frac{K_n x}{b}\right)}{\cosh\left(\frac{K_n}{b}\right)} + \sum_{n=1}^{\infty} D_n e_1^n(y) \frac{\cosh\left(\frac{k_n x}{b}\right)}{\cosh\left(\frac{k_n}{b}\right)} + \sum_{n=1}^{\infty} E_n f_2^n(x) \frac{\sinh(K_n(y-b))}{\sinh(K_n b)} + \sum_{n=1}^{\infty} F_n f_2^n(x) \frac{\cosh(K_n(y-b))}{\cosh(K_n b)} \quad \text{for } x \in (-1, 1) \cup y \in (0, 2b), \quad (4)$$

where  $k_n$  and  $K_n$  are the sequence of complex numbers that satisfy  $\sin(2k_n) = 2k_n$  and  $\sin(2K_n) = -2K_n$ .  $f_2^n$  is the even Papkovitch-Fadle eigenfunction in  $x$ , and  $e_1^n$  and  $e_2^n$  are odd and even eigenfunctions in  $y$  for regions 1 and 2. The biorthogonal properties of these expansions are then used to satisfy all boundary and matching conditions. Six equations are derived for the constants  $A_n$ - $F_n$  and after truncating the infinite series an approximation to the solution required is obtained. A plot of the streamlines for  $b = 1$  and a truncation of  $N = 16$  is shown in Figure 3.

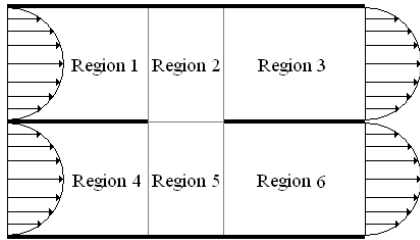


Figure 2. A diagram of the first flow

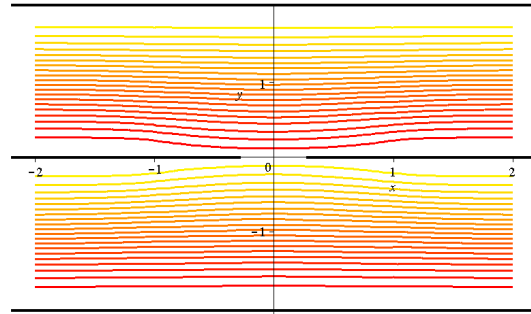


Figure 3. A plot of  $\Re\{\Psi(x, y)\}$  for the first steady flow

Similarly, using different bases in the expansions, two other linearly independent solutions can be derived. Due to symmetry, the easiest other possible choices are shown in the diagrams in Figures 4 and 5. The second flow (Figure 4) is only driven by Poiseuille flow in the top channel. The difference in order of  $\Psi$  below and above requires relatively more nodes for convergence.

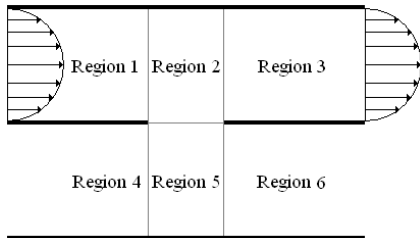


Figure 4. A diagram of the second flow

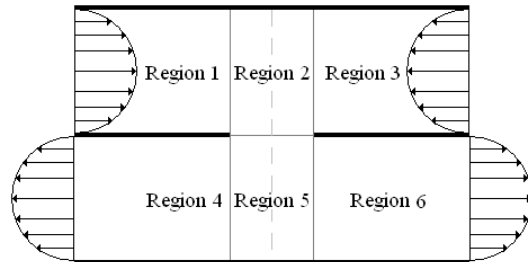


Figure 5. A diagram of the third flow

## CONCLUDING REMARKS

The analysis described in this abstract gives satisfying results for the stream function of different steady flows in two channels with a shunt between them. Although it has limitations, such as simplifying physiological vessels to two-dimensional channels, great insight can be gained from it. The authors hope to couple these results with clinical time-dependent data in the near future to model physiological problems that deal with shunts at low Reynolds numbers.

## References

- [1] Smith R.C.T.: The bending of a semi-infinite strip. *Aust. J. Sci. Res.* **5**:227–237, 1952.
- [2] Trogodn S.A., Joseph D.D.: Matched eigenfunction expansions for slow flow over a slot. *J. Non-Newtonian Fluid Mech.* **10**:185–213, 1982.
- [3] Driesen C.H., Kuerten J.G.M., Stremg M.: Low-Reynolds-number flow over partially covered cavities. *J. Eng. Math.* **34**:3–20, 1998.
- [4] Phillips, T.: Singular matched eigenfunction expansions for stokes flow around a corner. *J. Appl. Math.* **42**:13–26, 1989.

**MATHEMATICAL MODELLING OF HIGH-FREQUENCY FLOW IN CURVED, COMPLIANT ARTERIES**

Sevil Payvandi, Jennifer H. Siggers & Kim H. Parker  
*Department of Bioengineering, Imperial College London, Royal School of Mines Building, South Kensington Campus, SW7 2AZ*

**INTRODUCTION**

Cardiovascular disease, and in particular atherosclerosis, remain the leading cause of death in the western world. Despite the systemic nature of most risk factors, the distribution of atherosclerotic plaques in the cardiovascular system is highly focal, typically occurring in areas of disturbed flow such as curved arteries. The causative mechanisms of atherosclerosis remain unknown, but a correlation between atherosclerosis and wall shear stress has been identified [1]. Vessel compliance has usually been omitted from previous studies, but could influence the haemodynamics in the near-wall region and hence the shear stress. The aim of this research is to understand the effects of compliance on flow in idealised curved arteries at high frequency and small Reynolds number using asymptotic analysis.

**MODEL**

In order to create an idealised model that permits mathematical analysis of flow in a curved artery, we neglect non-planarity, time- and space-varying curvature, and thickness of the arterial wall, and model fully developed, Newtonian flow in a planar, weakly curved pipe. We assume that the flow is driven by a sinusoidally oscillating pressure gradient. Figure 1 displays the nondimensional coordinate system used, where  $a$  is the pipe radius,  $s$  is the distance along the centreline, and  $(r, \theta)$  are polar coordinates in the cross section. Note that  $s = 0$  corresponds to the axial position where the transmural pressure is zero. We make a number of additional

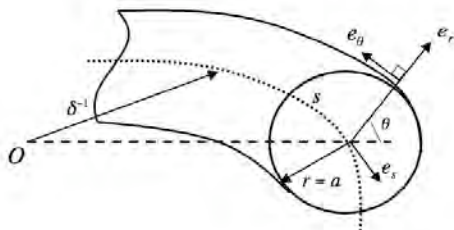


**Figure 1.** Nondimensional coordinate system

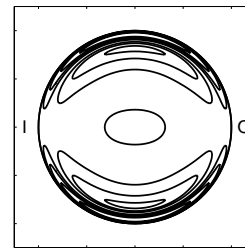


**Figure 2.** In-plane velocity at  $O(\epsilon^0)$ , (“I” denotes the inside of the pipe bend and “O” the outside).

simplifying assumptions; we assume that the dimensionless compliance,  $\epsilon$ , is small, and hence consider only the first deviation from flow in a rigid pipe, and therefore linearise the tube law to obtain a linear pressure–radius relationship. We take the limit of high frequency, characterised by the Womersley number  $\alpha \rightarrow \infty$ , where  $\alpha^2$  equals the ratio of the time for viscous transport of momentum across the pipe divided by the period of oscillation. Thus we extend the work of Lyne [2], who solved this system for a rigid pipe ( $\epsilon = 0$ ), showing that the flow consists of two distinct regions: an inviscid core and a thin Stokes boundary layer, shown in Figure 2, where the symbol “I” on the left-hand side is used to denote the inside of the pipe bend and “O” on the right-hand side is used to denote the outside of the bend. We also assume that the pressure gradient is small enough so that the Reynolds number of the steady component of the secondary flow,  $R_s$ , is small.

## RESULTS

We solve the Navier–Stokes equations separately in the two regions and then match the two solutions in an intermediate region known as the matching region. At  $O(\epsilon^0)$ , Lyne found that the leading solution of the secondary flow is steady and directed inwards; with flow across the centre of the pipe directed from the outside to the inside of the pipe bend. This in turn causes the axial wall shear stress to be higher at the inside of the pipe bend than at the outside. The generation of a steady flow in oscillatory viscous flow is broadly known as steady streaming, and in the case of Lyne is due to the interaction of the oscillatory pressure gradient with the curvature of the pipe. For the case of a compliant curved pipe, an additional mechanism exists whereby the oscillatory pressure gradient interacts with the compliance of the pipe walls, leading to steady streaming in the axial velocity. For both mechanisms, a steady flow is generated in the Stokes layer which does not fall to zero at the edge of the matching region, and instead drives a steady flow in the core. We examine the nature of the steady terms in the axial velocity and the effect of compliance on the steady terms in the streamfunction. The steady terms are important as they generate a sustained effect on the endothelial cells, and also have important consequences for mass transport. In the axial velocity, we find that the steady terms cause the core flow to be spatially dependent, and that the steady flow swaps in sign for upstream and downstream positions, such that the flow in the core ( $|r| < 0.6$ ) is always directed towards  $s = 0$  (Figure 3). In the streamfunction, we find that the  $O(\epsilon)$  steady terms oppose the  $O(\epsilon^0)$  flow towards the inside of the pipe bend, resulting in a reduction in the magnitude of the secondary flow. We also find that compliance results in a reduction in the axial wall shear stress, and affects the spatial distribution of the shear stress during the cycle. In addition, we find that the  $O(\epsilon)$  solution dominates the in-plane velocity leading to axisymmetric profiles of the flow for the majority of the cycle (Figure 4), which is very different to the  $O(\epsilon^0)$  flow seen in Figure 2.

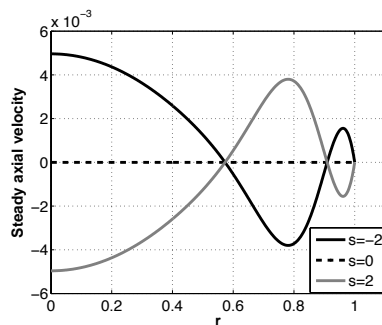


Figure 3. Steady axial velocity

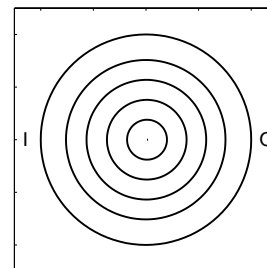


Figure 4. In-plane velocity due to compliance

## CONCLUDING REMARKS

In this study we have considered high-frequency flow in a weakly-curved, compliant pipe at low Reynolds number. The interaction of the unsteady pressure gradient with compliance leads to an additional mechanism of steady streaming, and affects the axial velocity and the streamfunction. Compliance also causes a reduction in the axial wall shear stress, and significantly affects the profile of the in-plane velocity.

## References

- [1] Caro C., Fitz-Gerald J., Schroter R.: Atheroma and arterial wall shear: observation, correlation and proposal of a shear dependent mass transfer mechanism for atherogenesis. *Proc R Soc B* **177**:109–159, 1971.
- [2] Lyne W.: Unsteady Viscous Flow in a Curved Pipe. *J. Fluid Mech* **45**:13–31, 1971.

## FLUID MOTION FOR MICRO-GRAVITY SIMULATIONS IN A RANDOM POSITIONING MACHINE

C. A. D. Leguy<sup>1</sup>, R. Delfos<sup>1</sup>, M.J.B.M. Pourquie<sup>1</sup>, C. Poelma<sup>1</sup>, J. Vreeburg<sup>2</sup>,  
J. Krooneman<sup>3</sup>, J. Westerweel<sup>1</sup> & J.J.W.A. van Loon<sup>4</sup>

<sup>1</sup> *Laboratory for Aero and Hydrodynamics, Delft University of Technology, (NL)*

<sup>2</sup> *Dutch Aerospace Laboratory, (NL)*

<sup>3</sup> *Bioclear, Groningen (NL)*

<sup>4</sup> *DESC OCB-ACTA, VU-University Amsterdam, (NL)*

### INTRODUCTION

To understand the role of gravity in biological systems one may decrease it going into free-fall conditions such as available on various platforms. Unfortunately, these experiments are cumbersome and expensive. Thus, alternative techniques like Random Positioning Machines (RPM), are now widely used to simulate the micro-gravity environment [1]. These instruments generate random movements so that gravitational effects cancel out over time. However, comparative studies performed with the RPM machine were unable to reproduce the clear-cut space flight results. These differences may be explained by undesirable stresses acting on the culture cells. They may be caused by internal flow motion, originating from the instationary motion during random rotation. The aim of this study is to predict fluid flow behaviour, wall shear stresses and suspended cell motion in an RPM container experimentally using particle image velocimetry (PIV) imaging and numerically using 3D and time-dependent numerical modeling.

### METHODS

#### The experimental set-up

A dual-axis rotating frame machine is used to reproduce the motion of a real RPM in a controllable way. A flask filled with water and fluorescent tracer particle ( $13 \mu m$ ) is positioned at the centre, surrounded by a PIV system. A green light dye-laser of 534 nanometer wavelength is used to create a light sheet inside the flask. We use a double-frame camera to record the particles inside the flask while the system is moving. Laser and camera are co-rotating with the flask.

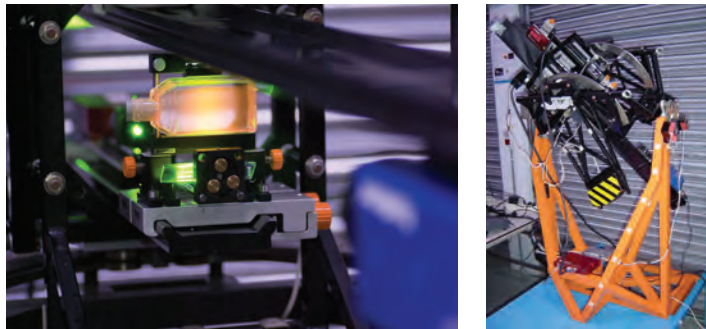


Figure 1. PIV system and the water-filled flask mounted on a two-axis rotating frame

#### The CFD simulations

To be able to reproduce the same experiment numerically, a Direct Numerical Simulation (DNS) model is used. In the DNS code, rotation is simulated by adding extra forces (centrifugal, Coriolis) to the momentum equation. Two-axis instationary rotation, as is employed for the RPM, have been simulated for a regular T25 flask geometry ( $6*4*2$  cm).



## RESULTS

For rotation around a single axis, fluid motion induced by inertia is observed parallel to the wall with good agreement between simulated and measured velocity field. Furthermore, boundary layers can be observed near the bottom. For spin-up about the X and Y axis according to the instationary angular velocity used in an RPM, more complex patterns are obtained in the DNS. A maximum velocities up to 7 cm/s near the wall and a maximum stress at the container wall of 62 mPa are derived.

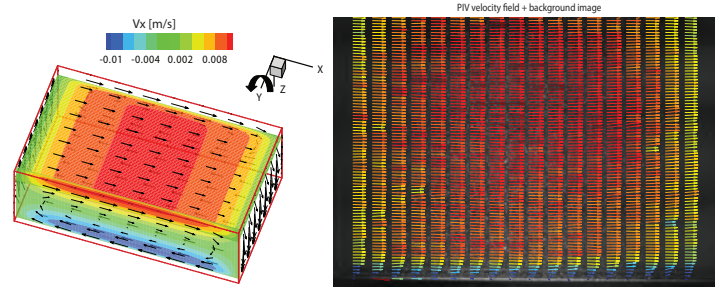


**Figure 2.** Simulated (left) and measured (right) velocity (relative to the container) during spin-up about the Y-axis for a fluid which is initially at rest for an acceleration  $\dot{\Omega}_y = 30^\circ/s^2$  and a maximum angular velocity  $\Omega_y = 60^\circ/s$ . PIV measurements are obtained in the X-Y plane at 5 mm from the wall.

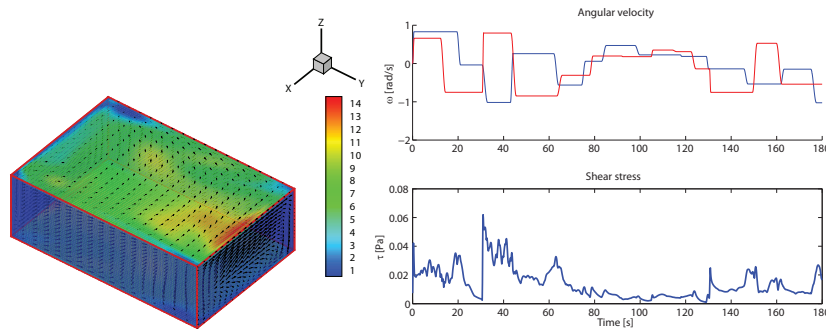


**Figure 3.** Right: Simulated wall shear rate [ $s^{-1}$ ] 17 seconds after spin-up about the X and Y axis according to the instationary angular velocity used in an RPM. Box-size:  $6 \times 4 \times 2$  [cm]. Left: Angular velocity patterns for both axis (top), maximum wall shear stress (bottom).

## CONCLUSION

For simple rotating motion, quantitative agreement between simulated and measured velocity field have been found. Considering motions as are employed for RPM, the numerical study suggests that stresses induced by the fluid are particularly high during changes of rotation velocity, i.e. acceleration, for cells cultured at the flask wall. At the conference, we aim to present a qualitative comparison between experimental and numerical results. Furthermore, numerical estimation of stresses acting on floating cells will be assessed.

## References

- [1] van Loon J.J.W.A.: Some history and use of the Random Positioning Machine, RPM, in gravity related research. *Adv. Space Res* **39**: 1161–1165, 2007.

## A UNIFIED NUMERICAL METHOD FOR FLUID-STRUCTURE INTERACTION APPLIED TO HUMAN COCHLEAR MECHANICS

Frank Böhnke<sup>1</sup>, Daniel Köster<sup>2</sup>

<sup>1</sup> *Dept. of Otolaryngology, TUM, Ismaningerstr. 22, 81664 München, Germany*

<sup>2</sup> *P+Z Engineering GmbH, Munich, Germany*

### INTRODUCTION

One of the main problems with the numerical simulation of the mechanical wave propagation in the cochlea is the coupling of elements representing the orthotropic elastic structure (cochlear partition) and the fluid (lymph). Usually displacements of the structure must be coupled to velocities of the fluid, which is an intrinsic problem.

### NUMERICAL METHOD

Our numerical method is based on the general conservation equations for momentum and mass valid for any continuum. The exact form of the stress tensor in the momentum equation and its dependence on the other unknowns determine whether the continuum will have the characteristics of a fluid or solid.

We introduce pressure as a new variable in the solid, defined as the hydrostatic part of the stress tensor. This is analogous to the description of the stress tensor in fluid mechanics and leads to a very similar systems of equations describing fluid and solid.

As exposed by [1] and [2], we follow a unified discretization approach, with a single Finite-Volume solver working on the combined fluid and solid domain. Using time integration the displacement gradients needed for the definition of the solid stress tensor are transformed into velocity gradients. We extend the formulation described by these authors to include (damped) orthotropic materials, as needed for the description of certain tissues in the cochlea.

The algorithm is implemented using the OpenFOAM® library which is available under General Public License (GPL). Some aspects of this library are given in [3].

### VALIDATION

To demonstrate the correctness of the implemented code, we adapted the “flexible tube” test case described in [1]. The problem represents a straight flexible tube with an inner diameter  $D = 20$  mm, wall thickness  $t = 2$  mm and length  $l = 100$  mm according to the dimensions of a large artery. The fluid in the tube has a dynamic viscosity  $\eta = 0.004$  Pa s, density  $\rho_f = 1000$  kg/m<sup>3</sup> and a bulk modulus  $K_f = 2.2$  GPa. The solid wall material has a Young’s modulus  $E = 1$  MPa, Poisson’s ratio  $\nu = 0.3$  and density  $\rho_s = 1000$  kg/m<sup>3</sup>.

Wave propagation through the pipe is initiated by applying a sudden step change in pressure of 5 kPa on the fluid at one end of the tube. The fluid at the other end is kept at 0 kPa.

As a result, a displacement wave occurs along the tube wall in combination with a pressure wave in the fluid. The predicted wave characteristics are in good agreement with the numerical and theoretical results presented in [1]. Figure 1 shows the radial displacement of the outer wall surface predicted by our algorithm at five selected times.

### APPLICATION TO THE HUMAN INNER EAR

In contrast to the isotropic material properties of the elastic tube the elastic structure (cochlear partition) of the inner ear is anisotropic. Therefore Young’s modulus changes related to a cartesian coordinate system because of the largely curved shape of the cochlear partition. Figure 2 (modified) shows a simplified 2D model of the cochlea following [4] which will be examined in a first step. The shaded area marks the outer boundary (bone) which encloses the lymph.

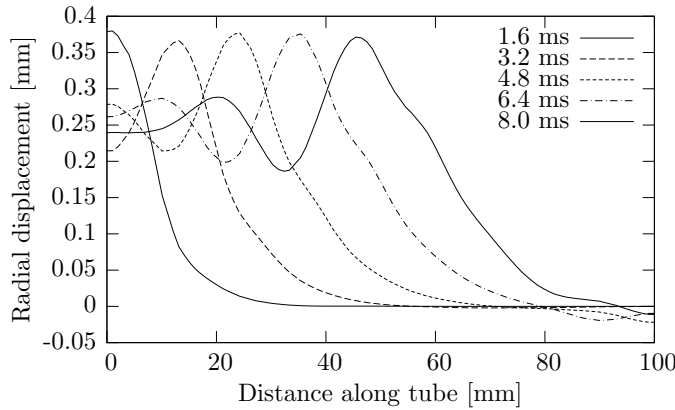


**Figure 1.** Radial displacement of the outer wall surface at times  $t=1.6, 3.2, 4.8, 6.4$  and  $8.0$  ms

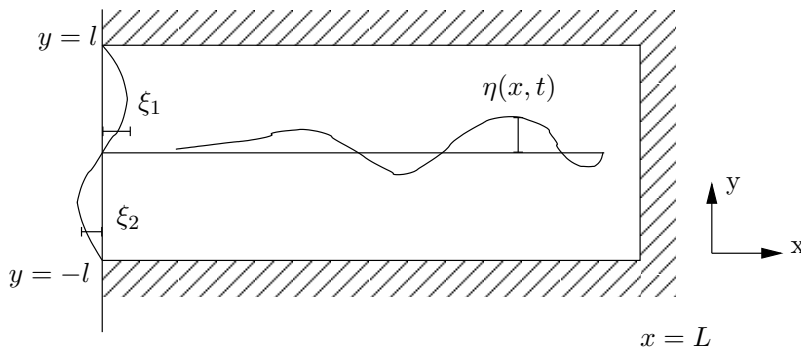


**Figure 2.** Simplified 2D model of the cochlea with exaggerated displacements of thin structures  
 $L = 35$  mm,  $l = 2$  mm

The upper left vertical line represents the oval window and the lower left vertical line the round window, which are fixed at the upper and lower endpoints. The horizontal line marks the cochlear partition including the basilar membrane which carries the sensory cells responsible for acoustic-neural transduction by inner hair cells necessary for hearing sensations. An acoustic field is induced by prescribing an oscillating deformation of the oval window. The round window and the cochlear partition will deform as a reaction.

After concluding the tests of the 2D cochlea model we plan to use the numerical method on 3D geometrical data obtained from  $\mu$ -Computer Tomography ( $\mu$ CT) scans with a spatial resolution of approximately  $6 \mu\text{m}$ .

## References

- [1] Greenshields C. J., Weller H. G.: A unified formulation for continuum mechanics applied to fluid-structure interaction in flexible tubes. *Int. J. Num. Meth. Eng.*, Vol. 64, Issue 12, pp. 1575–1593, 2005.
- [2] Papadakis G.: A novel pressure-velocity formulation and solution method for fluid-structure interaction problems. *J. Comp. Physics*, Vol. 227, pp. 3383–2404, 2008.
- [3] Weller H. G., Tabor G., Jasak H., Fureby C.: A tensorial approach to continuum mechanics using object-oriented techniques. *Computers in Physics*; Vol. 12, pp. 620–631, 1998.
- [4] Lesser M. B., Berkley D. A.: Fluid mechanics of the cochlea. Part I. *J. Fluid Mechanics*, Vol. 51, Part 3, pp. 497–512, 1972.

## VISCOUS AND NONLINEAR FLOW PHENOMENA IN THE COCHLEA

Elisabeth Edom, Dominik Obrist & Leonhard Kleiser  
*Institute of Fluid Dynamics, ETH Zurich, 8092 Zurich, Switzerland*

### INTRODUCTION

Sound signals are transmitted by the middle ear to the cochlea which is part of the inner ear. Here, the vibrations of the stapes, the last of the middle ear ossicles, evoke a traveling wave motion of the cochlear fluids and of the basilar membrane. This leads to the perception of sound. A better understanding of the flow phenomena in the cochlea will give further insight into our sense of hearing.

The cochlear fluid flow is often modeled as inviscid or as governed by a set of linear equations such as the Stokes equations. Also, results are often restricted to harmonic stimulations. In contrast to these approaches, we study the fluid dynamics in the cochlea including viscous, nonlinear, and transient phenomena. This allows us to account for viscous effects which are indicated by low Reynolds numbers, to investigate nonlinear effects (steady streaming) and to address cochlear responses to non-harmonic stimuli such as clicks.

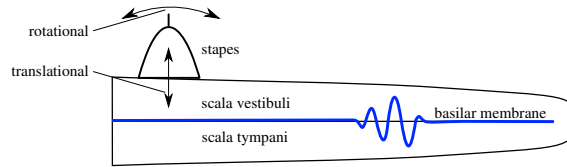


**Figure 1.** Schematic of the uncoiled cochlea.

### GOVERNING EQUATIONS AND COMPUTATIONAL MODELING

The lymphatic fluid in the cochlea is similar to water. Because at all but the highest physiological frequencies the acoustic waves are significantly longer than the length of the cochlea, the flow can be considered incompressible. Therefore, the fluid motion is modeled with the continuity equation

$$\nabla \cdot \mathbf{u} = 0 \quad (1)$$

and the Navier-Stokes equations which read in dimensionless form

$$\frac{\partial \mathbf{u}}{\partial t} + (\mathbf{u} \cdot \nabla) \mathbf{u} = -\nabla p + \frac{1}{Re} \nabla^2 \mathbf{u} \quad (2)$$

where  $\mathbf{u}$  denotes the velocity vector,  $t$  the time, and  $p$  the pressure.  $Re = UL/\nu$  represents the Reynolds number, with the maximum velocity of the stapes motion as the characteristic velocity  $U$ , the length of the stapes footplate as the characteristic length  $L$ , and the kinematic viscosity  $\nu$  of the fluid.

The basilar membrane is modeled as an array of uncoupled, one-dimensional damped oscillators, each governed by

$$m \frac{\partial^2 \eta}{\partial t^2} + r \frac{\partial \eta}{\partial t} + k\eta = -2p \quad (3)$$

where  $\eta$  denotes the displacement of the membrane and  $m$ ,  $r$ , and  $k$  its mechanical properties which change along the cochlear axis.

The above equations are solved with respect to a two-dimensional Cartesian coordinate system in which the complex geometry of the cochlea is idealized to a rectangular box. No-slip boundary conditions are imposed with zero velocity at the bounding walls and with in-/outflow velocities at the position of the stapes footplate.

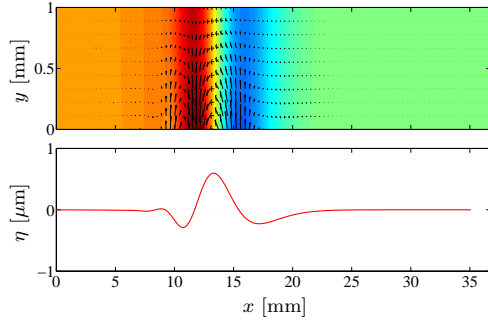


**Figure 2.** Instantaneous pressure field (top, colors), fluid velocities (top, arrows) and basilar membrane displacement (bottom) for a click stimulation (inviscid model for the fluid dynamics).

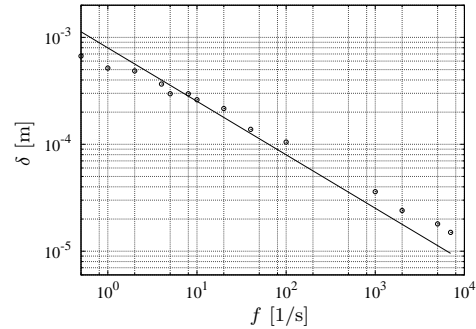


**Figure 3.** Boundary layer thickness  $\delta$  as a function of the frequency  $f$  for rocking stapes stimulation (—  $\delta_s$ ;  $\circ$  simulated).

The computations are carried out with a high-order solver for the incompressible Navier-Stokes equations [1] which is optimized for a massively parallel computation of very large flow problems. The governing equations are discretized with finite differences in space and with an explicit integration scheme in time. The basilar membrane is coupled in an immersed boundary-like approach to the fluid: The fluid velocities act on the structure which in turn exerts a force on the fluid.

## PRELIMINARY RESULTS AND OUTLOOK

Figure 2 shows the basilar membrane displacement for a click stimulation. It has been simulated with a transient potential flow model [2] following [3] and serves as a baseline result for future simulations including viscosity. Especially at low frequencies effects of viscosity are expected to influence the cochlear dynamics: First, the velocity profiles of the viscous and the inviscid case differ considerably due to the formation of boundary layers. Second, in viscous flow phase shifts between the bulk flow rate and the pressure gradient are present.

These properties of the viscous flow field have been investigated in preceding numerical studies in which the motion of the basilar membrane is not included. For stimulation with rotational motion components (“rocking motions”) of the stapes, the flow field is composed of a potential flow region and boundary layers similar to Stokes boundary layers. Figure 3 shows the boundary layer thicknesses of simulated results compared to the analytical solution for the Stokes case,  $\delta_s = C\sqrt{\nu/(2\pi f)}$  (with  $f$  as the frequency and the constant  $C = 2$ ). The phase lag between velocity and pressure is found to tend to  $45^\circ$  in the boundary layers and toward  $90^\circ$  in the potential flow region which is in accordance with analytical solutions.

We will present results for the fluid flow in the cochlea and for the basilar membrane motion under viscous conditions. Furthermore, we will investigate nonlinear effects (steady streaming) of the cochlear fluid dynamics. Also the influence of different stimuli (click stimulation, rotational and translational stapes motion) will be addressed.

**Acknowledgment** This work is partially funded by an ETH research grant.

## References

- [1] Henniger R., Obrist D., Kleiser L.: High-order accurate solution of the incompressible Navier-Stokes equations on massively parallel computers, *J. Comp. Phys.* **229**, 3543–3572, 2010.
- [2] Obrist D.: Transient inviscid flow in a passive linear model of the cochlea, *Proc. Appl. Math. Mech.* **9**, 477–478, 2009.
- [3] Lesser M.B., Berkley D.A.: Fluid mechanics of the cochlea. Part I, *J. Fluid Mech.* **51**, 497–512, 1972.

## COMPARISON OF THE FLOW PATTERNS IN HEALTHY AND PATHOLOGICAL VESTIBULAR SYSTEMS

Francesco Boselli, Dominik Obrist & Leonhard Kleiser  
*Institute of Fluid Dynamics, ETH Zurich, 8092 Zurich, Switzerland*

### INTRODUCTION

The temporal bone hosts bilaterally sensors for angular velocity (semicircular canals, SCCs), as well as sensors for linear acceleration (otolith organs). These structures are filled with endolymph, a fluid with mechanical properties similar to water. The SCCs are three mutually orthogonal slender ducts which span an angle of  $250^\circ$  and converge into a common chamber called utricle (see Figure 1 for the rendering of a single SCC with the utricle). Angular accelerations lead to an endolymph flow which displaces an elastic membrane at the end of each SCC. This membrane is known as the cupula. The cupula displacement triggers the hair cells which generate a neurological signal.

The ampulla (the end region which hosts the cupula) and the utricle have cross-sectional areas which are one order of magnitude bigger than the slender part of the SCCs. In the past, the endolymph flow has been modeled as a Poiseuille-like flow, such that the velocities in the enlarged part of the vestibular system become significantly smaller than in the slender canals. However, we have shown recently that angular accelerations lead to vortices in the utricle and the ampulla with velocities of the same order of magnitude as in the slender canals [1].

It is the objective of this study to investigate how these new features are affected by common diseases such as benign paroxysmal positional vertigo (BPPV) and endolymphatic hydrops. The former is known to be caused by the presence of small calcite particles in the SCC which settle under the influence of gravity and can lead to a positional endolymph flow without any corresponding angular movement of the head [2]. The latter disease (hydrops) is an increase of the endolymphatic pressure which can increase the utricular volume beyond the physiological range. This is of interest, since the utricular walls host the utricular maculae, i.e. the sensitive tissue of one of the two otolith organs.

### METHODS

The endolymph flow is a creeping flow because the Reynolds number  $Re$  is low ( $Re \approx 10^{-2}$ ). It can be modeled by the Stokes equations,

$$-\nabla p(\mathbf{x}) + \mu \nabla^2 \mathbf{u}(\mathbf{x}) = \mathbf{f}(\mathbf{x}, t) \quad \text{and} \quad \nabla \cdot \mathbf{u}(\mathbf{x}) = 0 \quad (1)$$

with no-slip boundary conditions at the wall;  $\mu$  is the viscosity of the fluid,  $t$  is the time,  $p$  and  $\mathbf{u} = (u_1, u_2, u_3)$  are the pressure and the velocity of the fluid, respectively, and  $\mathbf{x} = (x_1, x_2, x_3)$  are the coordinates. The force  $\mathbf{f} = \rho \ddot{\boldsymbol{\alpha}} \times \mathbf{x}$  is the fictitious force induced by the angular acceleration  $\ddot{\boldsymbol{\alpha}}$  of the head, where  $\rho$  is the density of the fluid.

We split the solution without cupula  $\mathbf{u}_\alpha = \mathbf{u}_p + \mathbf{u}_h$  into a homogenous  $\mathbf{u}_h$  and a particular solution  $\mathbf{u}_p$  which can be found analytically. The governing equations are linear and  $\mathbf{u}_h$  can be computed by the multilayer method of fundamental solutions (multilayer MFS) based on Stokeslets which are Green's functions of (1) [3].

The cupula is modeled by a pressure difference  $\Delta P$  across the cupula which is proportional to the endolymph volume displaced during a head maneuver. This pressure difference leads to a Poiseuille flow in the SCC which is superimposed on  $\mathbf{u}_\alpha$  to yield the final solution for a healthy SCC.

BPPV is modeled by introducing free floating particles (canaliths) in the canals. The positional flow  $\mathbf{u}$  induced by the settling canaliths is split according to  $\mathbf{u} = \mathbf{u}_c + \mathbf{u}_w$ . The flow  $\mathbf{u}_c$  is the unbounded Stokes flow induced by a canalith which is modeled by the force coupling method [4]. The flow  $\mathbf{u}_w$  represents the influence of the canal walls and is computed by multilayer MFS

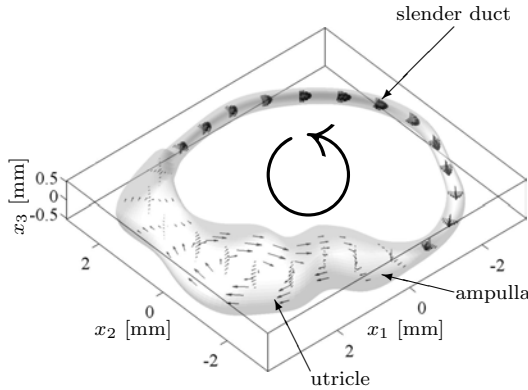


**Figure 1.** Arrows indicate the instantaneous flow field in a healthy horizontal SCC and utricle.

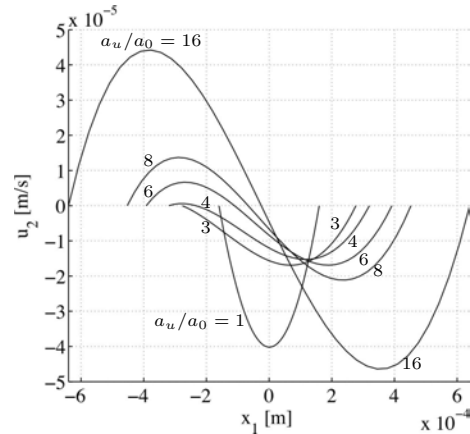


**Figure 2.** Axial velocity  $u_2$  in the utricle for different ratios of the utricular ( $a_u$ ) and SCC ( $a_0$ ) cross-sectional areas ( $a_u/a_0 = 1, 3, 4, 6, 8, 16$ ).

for the boundary conditions  $\mathbf{u}_w|_{\partial\Omega} = -\mathbf{u}_c|_{\partial\Omega}$  such that  $\mathbf{u}$  satisfies (1) with no-slip boundary conditions at the wall  $\partial\Omega$ .

Endolymphatic hydrops conditions are modeled here by increasing the cross-sectional area of the utricle.

## RESULTS

We apply our model to a single SCC connected with the utricle (Figure 1). In the slender part of the SCC, the flow induced by an angular acceleration is well approximated by a Poiseuille flow, while the flow in the larger utricular-ampullari space shows an S-shape profile typical of a vortex. Interestingly, the wall shear stresses induced by this vortex are strongest at the location of the sensory epithelia in the utricle and in the ampulla. This is a consequence of the observed vortex and the elliptic cross section of the utricle.

For BPPV, the settling canaliths lead to a pathological Poiseuille flow in the whole domain. The flow velocities and the wall shear stresses in the proximity of the ampullari hair cells are significantly smaller than the ones observed for a physiological S-shape profile of equal flow rate. The hydrops condition (enlarged utricle) increases the velocities of the observed vortex, and, consequently, the shear-stresses in the proximity of the utricular macula (Figure 2).

## CONCLUDING REMARKS

Our numerical approach allows us to analyze flow patterns in the ampulla and the utricle which cannot be predicted by the analytical models available in the literature. We have shown that these flow patterns change under the pathological conditions of BPPV or endolymphatic hydrops. Our results suggest that the ampulla anatomy is such that the mechanotransduction is more favored by physiological flows than by positional flows, e.g. induced by settling canaliths. Under hydrops conditions, the observed vortex in the utricle is stronger and may alter the macula response.

**Acknowledgement.** This work was partially supported by the Swiss National Science Foundation (SNF # 200021-116575).

## References

- [1] F. Boselli and D. Obrist and L. Kleiser: Numerical simulation of the flow in semicircular canals with the method of fundamental solutions. *Proc. Appl. Math. Mech.* **9**:485–486, 2009.
- [2] D. Obrist and S. Hegemann: Fluid-particle dynamics in canalithiasis. *J. Roy. Soc. Interface* **5**:1215–1229, 2008.
- [3] F. Boselli and D. Obrist and L. Kleiser: Multilayer MFS for Stokes problems. In: *Recent Studies in Meshless & Other Novel Computational Methods*. Tech Science Press, 71–86, 2010.
- [4] M. R. Maxey and B. K. Patel: Localized force representations for particles sedimenting in Stokes flow. *Int. J. Multiph. Flow* **27**:1603–1626, 2001.

## DYNAMICS OF THE VITREOUS HUMOUR AND STRESS ON THE RETINA GENERATED DURING EYE ROTATIONS

J. Meskauskas<sup>1</sup>, R. Repetto<sup>2</sup> & J.H. Siggers<sup>3</sup>

<sup>1</sup> *Department of Engineering of Structures, Water and Soil, University of L'Aquila, Strada provinciale per Monticchio, loc. Monticchio, 67100 L'Aquila*

<sup>2</sup> *Department of Civil, Environmental and Architectural Engineering, University of Genoa, Via Montallegro 1, 16145, Genova, Italy*

<sup>3</sup> *Department of Bioengineering, Imperial College London, London SW7 2AZ, UK*

### INTRODUCTION

The vitreous humour occupies the vitreous chamber, which is an approximately spherical cavity whose volume represents the majority of that of the eye. It is a transparent viscoelastic fluid whose properties have been studied by several authors [1, 2, 3]. During eye rotations, flow in the vitreous produces stresses on the retina that may play a role in the development of vitreoretinal diseases such as retinal detachment, a common condition leading to a high risk of loss of sight.

We study the motion of the vitreous humour induced by eye rotations and the corresponding stress distribution on the retina. We model the vitreous chamber as a rigid domain filled with a viscoelastic fluid.

### MOTION OF A VISCOELASTIC FLUID IN A SPHERE

We describe the cavity as a sphere of radius  $R_0$  and study the relaxation behaviour of a viscoelastic fluid, i.e. the transient flow that would be observed in the stationary sphere starting from non-stationary initial conditions in the fluid. We assume the displacements and velocities of the fluid particles are small, allowing us to neglect nonlinear terms in the equations of motion. This allows us to consider the velocity and pressure fields as a sum of terms of the form  $\mathbf{u} = \mathbf{u}_\lambda(\mathbf{x})e^{\lambda t} + c.c.$  and  $p = p_\lambda(\mathbf{x})e^{\lambda t} + c.c.$ , respectively, where  $\lambda \in \mathbb{C}$  is the growth rate. By expanding  $\mathbf{u}_\lambda$  and  $p_\lambda$  as a superposition of spherical harmonic functions, enforcing the no-slip boundary condition at the wall, regularity at the origin and seeking a non-trivial solution we find the eigenvalues and eigenfunctions of the system. We consider different rheological models of the vitreous from the literature, and invariably find the existence of complex eigenvalues, whose imaginary parts represent natural frequencies of oscillation of the system, and whose real parts are all negative, indicating that the motion decays over time. For all rheological models considered we find that the natural frequency associated with the least damped modes approximately ranges between 10 and 30 rad/s, which is in the physiological range.

In further work, we consider the fluid motion driven by small-amplitude azimuthal torsional oscillations of the domain with angular amplitude  $\epsilon$  and frequency  $\omega_0$ , which represent saccades of the eyeball. We compute the time-averaged total kinetic energy of the system  $\overline{\mathcal{K}}^*$  (normalised by the kinetic energy of a rigid sphere with the same density as the fluid) and show that it assumes large values (significantly greater than one) when the system is forced at resonant frequencies. This is shown in figure 1a where  $\overline{\mathcal{K}}^*$  is plotted versus the forcing frequency  $\omega_0$ . For frequencies close to a natural frequency, it is possible for the velocity away from the boundary to be larger than the velocity at the boundary, see figure 1b.

### EFFECT OF THE DEPARTURE OF THE GEOMETRY FROM THE SPHERICAL SHAPE

We also study the effect of a weak departure of the shape of the domain from a sphere. We do this by describing the shape of the domain in spherical coordinates as  $r = R_0(1 + \delta R(\theta, \phi))$ , where  $\delta \ll 1$  and  $R$  is an order-one function specifying the shape of the domain, and expanding our variables in terms of the small parameter  $\delta$ . We focus both on myopic eyes, which are elongated



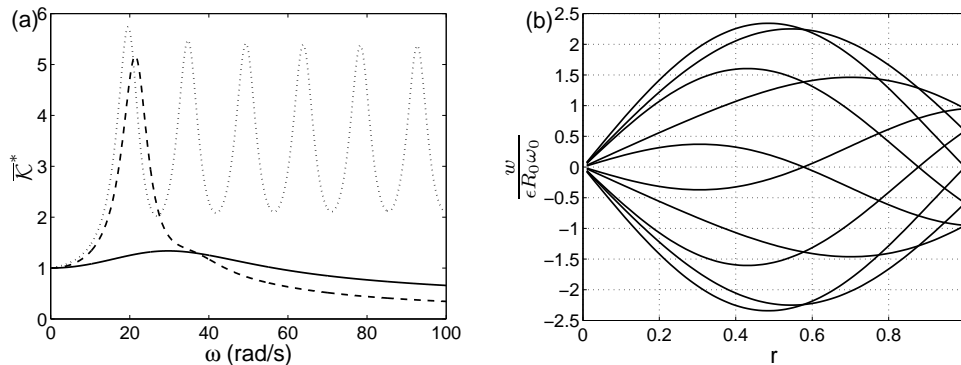


**Figure 1.** (a) Plots of the normalised kinetic energy  $\bar{\mathcal{K}}^*$  against frequency for different rheological properties of the vitreous. Solid curve: model based on measurements in [2]; dashed curve: model based on measurements in [3]; dotted curve: model based on measurements in [1]. (b) Azimuthal velocity profile with  $\omega_0$  set to the natural frequency using the model based on the measurements in [3]. The relevant nondimensional parameter is the complex Womersley number,  $\alpha_c = \sqrt{i\rho\omega_0^2 R_0^2 / \tilde{G}} = 3.50 + 2.48i$ , where  $\rho$  is the fluid density and  $\tilde{G}$  the complex modulus of the fluid.

in the antero–posterior direction, and on eyes subjected to scleral buckling, a surgical procedure whose aim is to induce a deformation in the shape of the sclera in order to facilitate sealing a retinal break. We study how the geometry of the domain influences the stress distribution on the retina.

## DISCUSSION AND CONCLUSION

We have used experimentally measured values of rheological properties to describe the behaviour of the vitreous humour. The system admits natural frequencies of oscillation that can be resonantly excited. Close to resonance there can be large wall shear stresses at the retina, which might be relevant for the occurrence of retinal detachment. Our findings are also relevant for the identification of optimal characteristics for vitreous replacement fluids. A common suggestion is that replacements should be viscoelastic, with a large enough elastic component to avoid excessive flow within the vitreous chamber. However, the possibility of resonance should be taken into account since, according to our model, a large elastic component leads to a larger number of resonant modes, and the associated frequencies can be in the physiological range.

We also show that the stress distribution on the retina is strongly affected by the shape of the domain. In particular, for myopic eyes the elongated eye shape induces a significant increase of the shear stress on the retina in the posterior segment of the eye. This might provide a mechanical explanation of the more frequent occurrence of posterior vitreous detachment and retinal detachment in these patients.

The authors are grateful for the support of the “British-Italian Partnership Programme” by MIUR-CRUI/British Council, which enabled this work to be carried out.

## References

- [1] Lee B., Litt M., Buchsbaum G.: Rheology of the vitreous body. Part I: Viscoelasticity of human vitreous. *Biorheology* **29**:521-533, 1992.
- [2] Nickerson C. S., Park J., Kornfield J. A., Karageozian H.: Rheological properties of the vitreous and the role of hyaluronic acid. *Journal of Biomechanics* **41** (9):1840-6, 2008.
- [3] Swindle K., Hamilton P., Ravi N.: In situ formation of hydrogels as vitreous substitutes: Viscoelastic comparison to porcine vitreous. *Journal of Biomedical Materials Research - Part A* **87A** (3):656-665, 2008.

## EXPERIMENTAL INVESTIGATION OF PARTICLE-LADEN FLOWS IN AN IN-VITRO MODEL OF A SINGLE ALVEOLUS

D. Borer<sup>1</sup>, T. Rösgen<sup>1</sup>

<sup>1</sup> *Institute of Fluid dynamics, ETH Zürich, Sonneggstrasse 3, 8092 Zürich*

### INTRODUCTION

In the past decades research into the role of fluid dynamics on the transport of nano- to micrometer sized particles in the pulmonary acinar region has steadily increased. New insights into the flow structure deep inside the lung have led to a revised understanding of the complex processes that take part in particle-laden flows at these small scales despite the low Reynolds number. The motivation lies in understanding the mechanisms of particle deposition in healthy as well as diseased lungs, to investigate the impact of pollutants and the efficiency of administering therapeutic drugs via absorption into the systemic circulation [1]. Also the possibility of external localized modification of the deposition process will be investigated.

In this work we will present an experimental model of an idealized alveolus comparable in size with a real alveolus. The study will address the possibility of using a commercial 3D-Lithography system in combination with  $\mu$ PIV to conduct research of alveolar flows in a direct fashion.

### RESEARCH APPROACH

To date experimental work has been done using scaled models, where fluid specific dimensionless numbers have been matched to the physical situation. Simple models investigated the flow features in rigid structures, for example where a rigid duct is used with alveoli represented by ring-like cavities around the central duct [5]. Other experiments incorporated the breathing motion by means of elastic cavities. Tippe [2] investigated an expanding elastic torus on a duct, showing the importance of the wall boundary conditions on the streamlines and therefore the particle paths. Chhabra [3], [4] used an anisotropic expanding 5/6 spherical membrane (diameter 24 mm) as a model of a respiratory bronchiole, the gravitational effects were investigated by numerically solving the particle transport equations in the measured flow field.

In the numerical field influential work has been carried out by Henry [6] with CFD simulations of an axial-symmetric alveolated duct. Here the main assumption for breathing motion is homogeneous spatial expansion with a convective flow in the duct. The results showed a stagnation saddle point associated with the recirculating flow. This has been linked to chaotic mixing and an increase in the overall mixing of particles in the alveolus and duct.

### SCALING CONSIDERATIONS

The simplest model for a single alveolus is a spherical cap on a airway duct with a half-opening angle of  $60^\circ$  (e.g. used in [2]). The alveolar diameters vary from around  $200 \mu\text{m}$  at the transitional bronchioles to around  $400 \mu\text{m}$  at the alveolar sacs [7]. The air flow is characterized by low Reynolds and Womersley number, the more so deeper into the lung due to the decrease in airway velocity.

The particle size plays an important role in deposition site and dominating physics. Particles with diameters larger than  $10 \mu\text{m}$  inertial impaction and gravitational settling dominate and deposition occurs mainly in the upper airways. Particles with diameters below  $0.5 \mu\text{m}$  diffusion is dominant and deposition takes place over multiple breathing cycles in the lower airways and acinar region. Particles in the range  $0.5\text{-}10 \mu\text{m}$  are in a transitional region with the lowest total deposition efficiency for the whole lung. In Figure 1 the timescales for

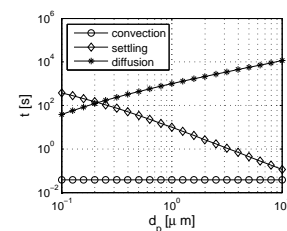


**Figure 1.** Timescales at acinar generation 5 (alveolus diameter of  $300 \mu\text{m}$ , sedentary breathing)

convection in the duct, diffusion and gravitational settling for varying particle sizes are shown. Although diffusion is the slowest process for large and medium particles, the influence in a complex flow, as in alveolar flows, is unclear. Matching all physical effects in a scaled model is difficult to achieve if Brownian motion is to be taken into account as well.

## EXPERIMENTAL APPROACH

A commercial 3D nano lithography system is being used to fabricate an alveolus-like cavity in a micro channel with the true physical length scales. The process is based on 2-photon polymerization allowing to write volumetric structures inside a bulk photoresist. The system can achieve resolutions of up to 150 nm with suitable materials and optics. The model representing the alveolus is written into the side channel of a microfluidic cross channel with a cross section of 300x300  $\mu\text{m}$ . The main channel represents the alveolar duct, the side channels allow for fluidic access, for example to manipulate the structural membrane. Figure 2 shows a first iteration of the model with a relatively stiff alveolar wall.

Mono disperse particles of desired size (from 0.5  $\mu\text{m}$  to 8  $\mu\text{m}$ ) act as tracers for the flow analysis with  $\mu\text{PIV}$ . The aim is to analyze and identify local deposition sites by fluorescent imaging. The intention is to investigate deposition mechanisms in dependency on flow behaviour and local topology. In a further step the potential of externally forced acoustic streaming on the deposition rate will be investigated. Acoustic streaming has proven to be an attractive forcing mechanism for microflows in general because of its remote action, local applicability and independence of viscosity (outside the acoustic boundary layer). Fluorescent labeling of representative aerosol particles and droplets will be used both to provide visual flow markers and to measure particle accumulation rates via integrated light emission.

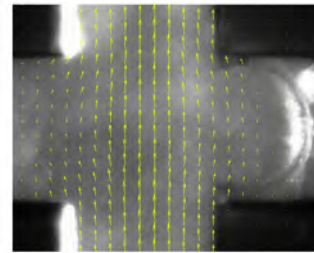


**Figure 2.** Image of micro channel with alveolus in right side channel, vectors depict the flow field.

## OUTLOOK

This approach guarantees the correct scaling of gravitational settling and diffusion effects by utilizing a controllable and reproducible design of small scale geometries. This is considered useful for subsequent validation of the results with numerical simulations. The versatility of the 3D manufacturing process also allows for more complicated and realistic geometries such as those derived from microtomographic scans of real tissue samples for future studies. Also, the potential impact of different forcing mechanisms can be studied directly.

## References

- [1] Patton J.S., Byron P.R.: Inhaling medicines: delivering drugs to the body through the lungs. *Nat. Rev. Drug Disc.* **6**:67-74 (2007).
- [2] Tippe A., Tsuda A.: Recirculating flow in an expanding alveolar model: experimental evidence of flow-induced mixing of aerosols in the pulmonary acinus. *J. Aerosol Sci.*, **31**:979986, (1999).
- [3] Chhabra S., Prasad A.K.: Flow and Particle Dispersion in a Pulmonary AlveolusPart I: Velocity Measurements and Convective Particle Transport. *J. Biomech. Eng.* **132**:051009 (2010).
- [4] Chhabra S., Prasad A.K.: Flow and Particle Dispersion in a Pulmonary AlveolusPart II: effect of gravity on particle transport. *J. Biomech. Eng.* **132**:051010 (2010).
- [5] van Ertbruggen C. et al.: Validation of CFD predictions of flow in a 3D alveolated bend with experimental data. *J. Biomech.*, Volume 41, Issue 2, (2008).
- [6] Henry F.S., Butler J.P., Tsuda A.: Kinematically irreversible acinar flow: a departure from classical dispersive aerosol transport theories. *J. of App. Physi.* **92**:835845 (2002).
- [7] Haefeli-Bleuer B., Weibel E.R.: Morphometry of the human pulmonary acinus. *Anat. Rec.*, **220**:401414 (1988).

## UNSTEADY SURFACTANT-LADEN LIQUID PLUG PROPAGATION: A MODEL FOR SURFACTANT REPLACEMENT THERAPY

Ufuk Olgac & Metin Muradoglu

*Department of Mechanical Engineering, Koc University, Rumeli Feneri Yolu, Sariyer, 34450, Istanbul, Turkey*

### INTRODUCTION

Prematurely born neonates can develop respiratory distress syndrome (RDS) as their lungs are not mature enough to produce sufficient amounts of surfactants. Surfactants reduce the surface tension on the thin layer of liquid that coats the inner surface of the airways and the alveoli; and therefore, reduce the work required to expand the lungs with each breath. Surfactant replacement therapy (SRT) is a standart treatment for premature neonates suffering from RDS. In SRT, liquid with exogenous surfactant is instilled in the trachea and form a liquid plug, which subsequently propagates through the trachea by inspiration and spreads the exogenous surfactant to the airways. The efficacy of the treatment depends on various parameters such as the size of the liquid plug, inspiration frequency and the physical properties of the exogenous surfactant. We performed unsteady simulations of surfactant-laden liquid plug propagation in order to comprehend and improve the dynamics of the treatment.

### METHODS & RESULTS

The finite-difference/front-tracking method for computations of interfacial flows with soluble surfactants, developed by Muradoglu & Tryggvason (2008) [1], is used in this study. This method is designed to solve the evolution equations of the interfacial and bulk surfactant concentrations together with the incompressible Navier-Stokes equations. In this method, the interface is represented by connected Lagrangian marker points moving with the local flow velocity interpolated from the neighboring stationary regular Cartesian Eulerian grid. The flow equations and the bulk surfactant concentration equation are solved on the Eulerian grid, whereas the evolution equation of the surfactant concentration on the interface is solved on the Lagrangian grid. Interfacial surface tension is related to the surfactant concentration at the interface through a non-linear equation of state. Surface tension forces at the interface are computed on the Lagrangian grid and distributed over the neighboring Eulerian grid cells as body forces in a conservative manner using Peskin's distribution function [1].

Relevant dimensional and non-dimensional parameters for liquid plug propagation in a neonatal lung are as follows: We assume that the neonatal lung may be modeled as starting from generation 7 ( $n = 7$ ) and the distal generations of an adult lung  $7 \leq n \leq 18$ . Using the physical properties of the exogenous surfactant Survanta ( $\rho = 940 \text{ kg/m}^3$ ,  $\mu = 0.042 \text{ Pa}\cdot\text{s}$ ,  $\sigma = 0.025 \text{ N/m}$ ) [2], the range of non-dimensional parameters  $Re = \rho UR/\mu$ ,  $Ca = \mu U/\sigma$ , and  $\lambda = Re/Ca$  in a neonatal lung for generations  $1 \leq n \leq 12$  are  $0.1 \leq Re \leq 40$ ,  $0.02 \leq Ca \leq 2$  and  $5 \leq \lambda \leq 20$ . Fully covered with surfactant, the surface tension,  $\sigma$ , on the interface should assume the surface tension of the surfactant,  $\sigma = 0.025 \text{ N/m}$ . We assume that the air-liquid interface is initially surfactant-free, and using the nonlinear equation of state, we calculate the surface tension of the clean interface,  $\sigma_s$ , to be  $0.5 \text{ N/m}$ . Using this value of surface tension for the initially clean interface, we perform our simulations in a neonatal trachea ( $n = 7$ ), for  $Re = 40$ ,  $Ca = 0.1$ , and  $\lambda = 400$ . The remaining non-dimensional parameters governing the surfactant dynamics -Biot number,  $Bi$ , Damkohler number,  $Da$ , the ratio of absorption to desorption rates, Peclet number in the bulk and on the interface,  $Pe_c$  and  $Pe_s$ , respectively- are estimated with the physical properties of Survanta. The instilled plug initially contains  $2 \text{ mg}$  of surfactant with the critical micelle concentration,  $C_{CMC}$ , and the liquid lining the airway is surfactant-free. Both the leading and trailing film thicknesses are initially estimated with the predictions of Halpern and Gaver (1994) [3]. At the inlet, analytical solution for a fully developed velocity profile is prescribed.

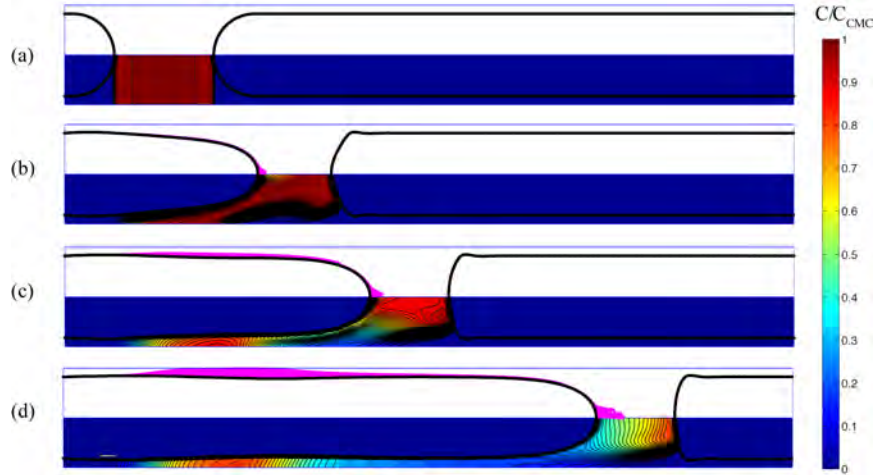


**Figure 1.** Propagation of the instilled liquid plug at various non-dimensional times: (a)  $t^* = 0.0$ , (b)  $t^* = 1.6$ , (c)  $t^* = 3.2$ , (d)  $t^* = 6.4$ . The upper half shows the interfacial surfactant concentration with a bar-plot (not-to-scale) and the lower half shows the non-dimensional bulk surfactant concentration.

Figure 1 shows the bulk and the interfacial surfactant concentrations as the instilled liquid plug propagates downstream through the trachea. We observe that part of the initially instilled surfactant is subsequently captured in the trailing film, whereas a second part is accumulated at the leading meniscus of the plug (See Fig. 1d). We further observe that the surfactant distribution on the interface is not homogeneous. The surfactant absorbed on the trailing film reduces the surface tension on the interface and increases the liquid film thickness. Therefore, the durability of the liquid plug depends on the surfactant dynamics in the bulk and on the interface. The particular characteristics of the bulk and the interfacial surfactant distribution depend on the physical properties of the surfactant such as viscosity, surface tension, diffusion coefficient, and the adsorption and desorption rates, as well as the inspiration frequency, i.e., velocity of the liquid plug. We, therefore performed further computations for a wide range of non-dimensional parameters in order to improve the efficacy of the therapy.

## CONCLUSIONS

Unsteady surfactant-laden liquid plug propagation is computationally studied using a finite-difference/front-tracking method and proposed as a model for surfactant replacement therapy. Computations are performed in a representation of a neonatal trachea for a wide range of non-dimensional parameters and optimal treatment conditions are investigated.

## Acknowledgement

The first author (UO) is supported by the Scientific and Technological Research Council of Turkey (TUBITAK) through BIDEB.

## References

- [1] Muradoglu M., Tryggvason G.: A Front-Tracking Method for Computation of Interfacial Flows with Soluble Surfactants. *J. Comput. Phys.* **227**:2238–2262, 2008.
- [2] Fujioka H., Grotberg J.B.: The Steady Propagation of a Surfactant-Laden Liquid Plug in a Two-Dimensional Channel. *Phys. Fluids* **17**:082102, 2005.
- [3] Halpern D., Gaver D.P.: Boundary-Element Analysis of the Time-Dependent Motion of a Semiinfinite Bubble in a Channel. *J. Comput. Phys.* **115**:366–375, 1994.

## EFFECTS OF SURFACTANT ON MOTION OF A LARGE BUBBLE IN A CAPILLARY TUBE

Metin Muradoglu, Gokalp Gursel & Ufuk Olgac

*Department of Mechanical Engineering, Koc University, Rumelifeneri Yolu, Sariyer, 34450 Istanbul, Turkey*

### INTRODUCTION

The motion of a large bubble moving through a capillary tube in the presence of both insoluble and soluble surfactants is studied computationally using the finite-difference/front-tracking method [1] as a model for propagation of an air finger into the liquid plugs that form in pulmonary airways. It is well known that pulmonary surfactant plays a vital role both in preventing the formation of liquid plug and in reducing the work required to expand the lungs with each breath [2]. Emphasis is placed here on the effects of surfactant on the liquid film thickness between the bubble and tube wall. The numerical method is designed to solve the evolution equations of the interfacial and bulk surfactant concentrations coupled with the incompressible Navier Stokes equations. A non-linear equation of state is used to relate interfacial surface tension to surfactant concentration at the interface. The method is validated for simple test cases and the computational results are found to be in a good agreement with the analytical solutions. The film thickness is first computed for the clean bubble case and the results are compared with the lubrication theory in the limit of small capillary numbers, i.e.,  $Ca \ll 1$ . Finally the method is used to simulate the effects of insoluble and soluble surfactants on the film thickness for a wide range of governing non-dimensional numbers.

### RESULTS & DISCUSSIONS

We consider a straight cylindrical capillary tube of radius  $R$  and assume that the flow is axisymmetric. The computational domain is  $R$  in radial direction and  $L$  in the axial direction. A constant flow rate is specified at the inlet assuming a fully developed Poiseuille-Hagen flow. The bubble is initially located at the channel centerline close to the inlet with an approximate shape consisting of hemispherical head and tail, and a cylindrical middle part. Computations are performed for clean interface and the results are compared with the Taylor's law [3] in Fig. 1 to show the accuracy of the numerical method. As can be seen in this figure, an excellent agreement is obtained between the present results and the Taylor's law.

After validation of the method for the clean case, extensive computations are performed to examine the effects of insoluble and soluble surfactant on the liquid film thickness between the gas bubble and channel wall. To demonstrate the effects of the surfactant, the effective capillary number is kept constant in all clean, insoluble and soluble surfactant cases. The effective capillary number is defined as  $Ca_{\text{eff}} = \mu U / \sigma_{\text{eff}}$  where  $\mu$  is the liquid viscosity,  $U$  is the average velocity in the channel and  $\sigma_{\text{eff}}$  is the effective surface tension coefficient computed from the equation of state using the average surfactant concentration at the interface. Since the average surfactant concentration cannot be specified at the beginning for the soluble surfactant case, the computations are first performed for the soluble case and the average surfactant concentration is computed when a steady state is reached. Then this average surfactant concentration is used to compute the effective surface tension coefficient to be employed for clean case and also as the initial condition for the insoluble case. Figure 2a shows the film thicknesses computed for clean, insoluble and soluble surfactant cases with the effective capillary number of  $Ca_{\text{eff}} = 0.0125$ . As can be seen in this figure, the film thickness generally increases with the addition of surfactant and it is slightly higher in the insoluble case than the soluble case, which can be explained by the difference between the surfactant distributions plotted in Fig2b. This figure shows that the surfactant concentration at the leading edge of the bubble is larger in the soluble case due to continuous supply of surfactant from the bulk fluid. Finally the surfactant distribution and streamlines are plotted in the steady state in Fig. 3 for all three cases. It is clear that surfactant

significantly alters the flow field in the vicinity of the bubble.

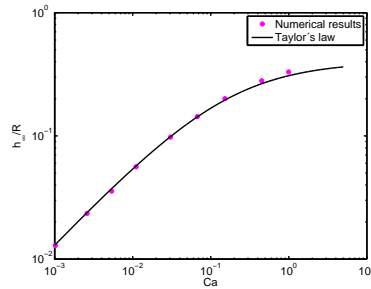


**Figure 1.** Film thickness for the clean bubble case. Solid line is Taylor's law [3] and symbols are the present results.

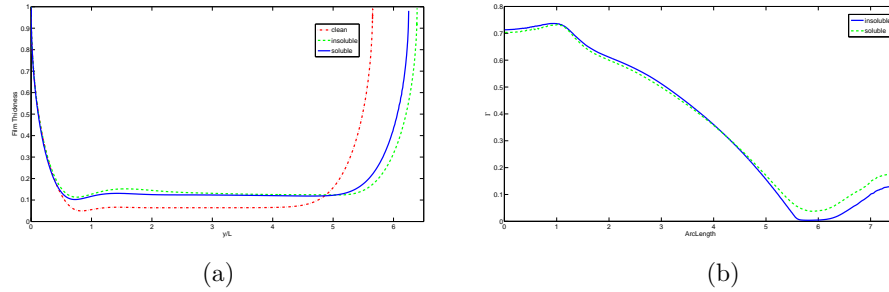


**Figure 2.** The film thicknesses computed for clean, insoluble and soluble cases (left figure) and the surfactant concentration distribution at the interface in the steady state for insoluble and soluble cases (right figure)

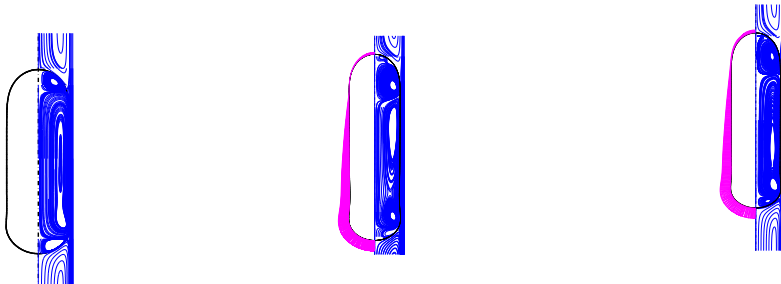


**Figure 3.** The streamlines (right portion) and interfacial surfactant distribution (right portion) for clean (left), insoluble (middle) and soluble (right) cases.

## ACKNOWLEDGEMENTS

This work is supported by TUBITAK with Grant No. 108M238.

## References

- [1] Muradoglu M., Tryggvason G.: A front-tracking method for computation of interfacial flows with soluble surfactants. *J. Comput. Phys.*: 227(4):2238-2262, 2008.
- [2] Grothberg JB.: Respiratory Fluid Mechanics and Transport Processes. *Annu. Rev. Biomed. Eng.* **3**:421-457, 2001.
- [3] Aussillous P., Quere D.: Quick deposition of a fluid on the wall of a tube. *Phys. Fluids*: 12, 23672371, 2000.

## MULTISCALE ANALYSIS OF FLUID FLOW IN LYMPHATIC CAPILLARIES

Tiina Roose<sup>1</sup>, Melody Swartz<sup>2</sup>

<sup>1</sup> *Bioengineering, School of Engineering Sciences, University of Southampton, Highfield, University Road, SO17 1BJ Southampton, UK*

<sup>2</sup> *Institute of Bioengineering, Ecole Polytechnique Federale Lausanne*

### INTRODUCTION

Understanding lymphatic function has come to the forefront of the research agenda in recent years largely because of its relevance to cancer metastasis, lymphedema, and immunology. In this paper we develop a model that describes lymphatic drainage from the tissue compartment into lymphatic capillaries using homogenization methods (Pavliotis&Stuart 2008). This allows tissue-scale lymphatic flow to be integrated with the details of lymphatic capillary microstructure enabling us to compare different possible lymphatic capillary microstructures, assess their relative efficacy, and gain insight into the functionality of lymphatic anatomy. We find that in the most common lymphatic capillary permeability limit, the limiting resistance for fluid drainage is that from the interstitium into the capillaries rather than the fluid transport within the capillaries. We also find that between hexagonal, square and parallel configurations of lymphatic capillaries, the hexagonal structure is the more uniform structure for interstitial and capillary fluid transport than the square and parallel tube configuration. Thus, by using homogenization theory, one can assess how lymphatic microstructure influences the macroscale fluid drainage by the lymphatics. We conclude that the hexagonal network of dermal lymphatic capillaries appears to be optimized for uniform capillary flow and drainage.

### METHODS

We consider the tissue being modeled to consist of the lymphatic capillary domain  $\Omega^C$  and the interstitial domain  $\Omega^I$  assuming that there are no other structures within it; in this way we introduce all the fluid sources from the blood vessel capillaries as pressure gradients in boundary conditions to our problem. We develop our theory starting with the specific microstructure, e.g., the network shown on Figure 1. The microscale unit (Fig. 1b) corresponds to the macroscale network in Figure 1a, for example.

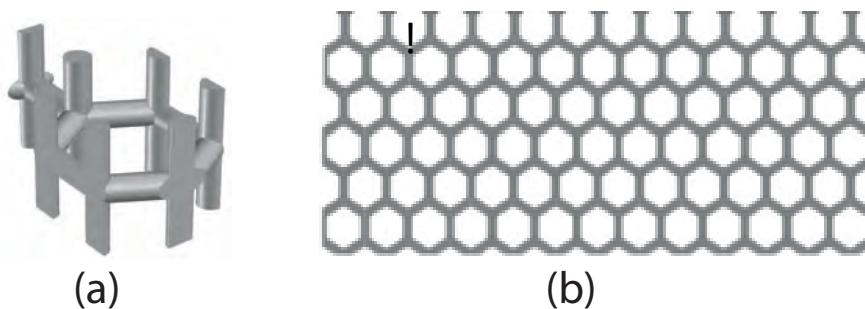


**Figure 1.** (a) Lymphatic capillary microstructure. (b) Lymphatic capillary macrostructure.

First we describe a model that is valid on both the unit cell scale (Fig. 1a) as well as the network scale (Fig. 1b). Then we use multiscale homogenization theory to derive a simpler model valid on the macroscale that still retains all the necessary information about the microscale. We consider the fluid flow in the interstitium to be described by the Darcys law, and the fluid flow



inside the lymphatic capillaries to be described by Stokes flow. The transfer of fluid from the interstitium into the lymphatic capillaries is controlled by the pressure difference between the two domains and by the lymphatic capillary permeability.

The size of the typical unit cell is  $l = 500$  microns. However, we are typically interested in how large number of these structures function in tissues of the size  $L = 5$  cm. Thus, the aspect ratio of the microstructure to the macrostructure is  $\epsilon = l/L \approx 0.1$ . This suggest us to look for a multiple scale expansion solution to the coupled Darcy and Stokes flow problem. Thus, we assume that in addition to microscopic space variable  $\mathbf{x}$ , the solution also depends on macroscopic space variable  $\mathbf{y}$ . The two space variables are related by  $\mathbf{y} = \epsilon\mathbf{x}$ , and hence also  $\nabla = \nabla_x + \epsilon\nabla_y$ . By conducting the multiple scale expansion we find that at the leading order the fluid pressure on the tissue depends on the macroscopic variable only. However, the higher order terms imply that the fluid flow inside the lymphatic capillary network and in the interstitium is on average described by  $\nabla \cdot (\mathbf{K}_{eff} \cdot \nabla p^I) = \alpha\rho(p^I - p^C)$ ,  $\nabla \cdot (\mathbf{E}_{eff} \cdot \nabla p^C) = 0$ , where  $p^I$  and  $p^C$  are pressures in interstitium and capillaries, respectively.  $\alpha$  is the permeability of lymphatic vessels, and  $\rho$  is the density of lymphatic fluid. The effective macroscale interstitial permeability is given by  $\mathbf{K}_{eff} = \frac{l^2}{\mu V} \int_{\Omega^C} \xi_i^j dV$ , where  $\mu$  is the fluid viscosity,  $V$  is the volume of the microscale unit element, and  $\xi_i^j$  is the solution to the microscale cell problem given by  $\nabla_x \cdot \xi^j = 0$ ,  $\nabla_x \pi^j = \nabla_x^2 \xi^j + \mathbf{e}_j$  with  $\xi^j = 0$  on capillary surface.

The effective macroscale intersitital permeability is given by  $\mathbf{E}_{eff} = \frac{k}{\mu} \left( \frac{V_I}{V} + \frac{1}{V} \int_{\partial\Omega} \omega_j n_j dS \right)$ , where  $k$  is the interstitial hydraulic conductivity in absence of lymphatic vessels,  $V_I/V$  is the volume fraction of the interstitium in the tissue, and  $\omega_j$  is the solution to microscale problem  $\nabla_x^2 \omega_j = 0$  and  $\mathbf{n} \cdot \nabla_x \omega_j = \mathbf{n} \cdot \mathbf{e}_j$  on lymphatic capillary surfaces. Thus, by undertaking multiscale homogenisation study we can determine how microstructure explicitly influences the macroscopic fluid flow within lymphatics and in particular we can compare the different microstructures. We used this to analyse square, parallel tube, and various combinations of these with hexagonal microstructure.

### Concluding Remarks

Multiscale homogenisation is a powerful technique that enables us to compare how different lymphatic capillary microstructures influence fluid drainage in the tissues on the macroscale. Using this method we can conclude that the overall interstitial permeability decreases only by couple of percent depending on the exact microstructure. However, capillary permeability is heavily dependent on the exact microstructure and in general its dependence is stronger than that of interstitial permeability. When comparing different geometric configurations it becomes apparent that whilst the hexagonal and parallel tube configurations are very comparable in the dominant flow direction, the square grid microstructure is an outlier in as much that the reduction in permeability does not correlate with the interstitial volume fraction as strongly as in the case of other microstructures considered.

### References

- [1] Pavliotis G.A., Stuart A.M.: Multiscale Methods. Averaging and Homogenisation. Springer, 2008.

## BLOOD FLOW AND DEFORMATION OF LIVER TISSUE DURING PORTAL HYPERTENSION

Jennifer Siggers<sup>1</sup>, Andrea Bonfiglio<sup>2</sup>, Kritsada Leunchavaphongse<sup>1</sup> & Rodolfo Repetto<sup>2</sup>

<sup>1</sup> Department of Bioengineering, Imperial College London, London SW7 2AZ

<sup>2</sup> Department of Civil, Environmental and Architectural Engineering, University of Genoa, Via Montallegro 1, 16145, Genova, Italy

### INTRODUCTION AND MOTIVATION

Blood supply to the liver comes from two major vessels: the hepatic artery and the hepatic vein. These vessels bifurcate repeatedly in successive generations to the terminal arteries and terminal portal veins, which lie together in portal tracts. Blood is drained from the liver through the hepatic veins, which, inside the liver, also bifurcates through successive generations to the central veins. On the scale of the microcirculation, the liver is composed of lobules, which are small units of tissue whose shape is approximately a uniform prism, see Figure 1. The cross-section of the prism is approximately a polygon with typically 5 to 7 vertices, at each of which there is a portal tract (thus the portal tracts run along the parallel edges of the prism), and a central vein approximately at the centre (thus the central vein runs roughly along the axis of the prism). Blood flows out of the portal tracts into small side branches called sinusoids, and the vessels from the portal vein and those from the artery soon merge with one another. However, it is thought that only a limited amount of mixing occurs between the portal venous and arterial blood, since, at a given merger, for most of the time blood flows from the portal vein, but there are occasional bursts of blood from the artery (during which the flow from the vein stops). The sinusoids are tortuous and interconnected and they carry the blood across the lobule and into to the central veins

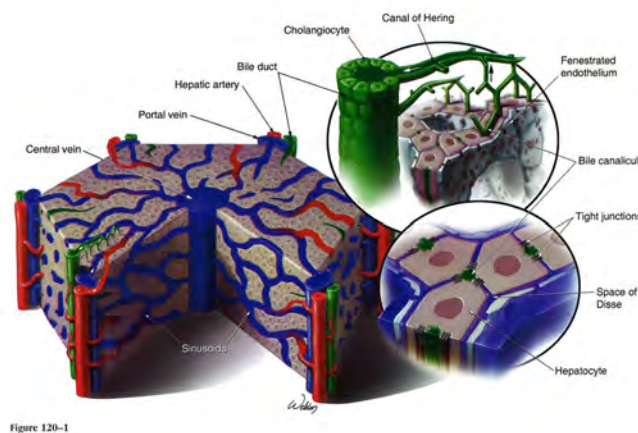


Figure 120-1

Figure 1. Sketch of a lobule, from [2].

Small-for-size liver syndrome is a serious condition that occurs when the liver has to carry too much blood flow (flux per unit mass of liver tissue). It may occur after a liver resection (removal of a diseased or damaged part of the liver) or after split-liver transplantation. It can lead to high pressures in the hepatic portal vein, which in turn damage the tissue. The aim of this work is therefore to find the blood flow and pressure distributions during portal hypertension, which could lead to better treatment.

There are relatively few previous mathematical models of blood flow in the liver, and even fewer of the microcirculation. However, Ricken *et al.* [3] developed a poroelastic model of the hepatic microcirculation, which they used to investigate the remodelling of the sinusoidal bed that occurs after vessel damage during liver surgery.

## MATHEMATICAL MODEL

We develop a model of blood flow in the sinusoids to investigate conditions when the portal tract pressure is high. We exploit the typical architecture of the liver, but idealise it by representing the lobules as regular hexagonal prisms with a portal tract centred on each of the parallel edges and a central vein running along the axis of the prisms, see figure 1. We assume that the lobules are sufficiently long that end effects can be neglected and that the flow is two-dimensional. During portal hypertension the sinusoidal pressure will also be high, which could lead to deformation of the tissue, and therefore we model the tissue as a Biot poroelastic medium. Instead of using the zero-pressure configuration as the reference for the solid, we note that the microcirculation is pressurised throughout life, and hence assume that, under conditions of normal pressure, the permeability of the medium is spatially uniform. The use of Darcy's law assumes quasi-steady conditions, and therefore the model may not be accurate during bursts.

We also perform two further tests to justify our modelling assumptions. (i) Detailed images of the sinusoids suggest that they tend to be preferentially orientated in the directions from the portal tracts towards the nearest central veins, and thus we develop an anisotropic porous medium model of the tissue. (ii) Darcy's law assumes that the fluid in the vessels is Newtonian, which is not well justified on the scale of the sinusoids. We therefore use the Walburn–Schneck model for blood rheology [4]. For both of these modifications, the results are quantitatively very similar to the results obtained without the modifications, and therefore we do not include them in our results.

## RESULTS AND DISCUSSION

With a rigid model of the solid, we can treat the vessels as point sources and point sinks in the plane, allowing us to find the flow and pressure in the form of an infinite series solution. We can also use a conformal mapping technique to map one sixth of the hexagonal cross-section to the upper half of the complex plane. Finding the solution in the upper half plane and applying the reverse transformation allows computation of the flow and pressure.

With the compliant model, we predict the tissue deformation, blood flow and pressure distribution within the lobules. The results suggest the tissue can deform significantly under conditions of portal hypertension, resulting in a large spatial variation in the permeability across a lobule. A rigid model of the tissue would lead to a prediction of linear growth in the flux of blood across the lobule as the portal pressure is raised. However, the addition of compliance leads to a significantly faster rate of flux increase with portal pressure, and the rate of increase also grows with increasing pressure.

## ACKNOWLEDGEMENTS

The collaboration between the authors has been funded within the framework of the “British–Italian Partnership Programme” by MIUR-CRUI/British Council. The authors are grateful to Dr Stefano Di Domenico, S. Martino Hospital, Genoa for drawing their attention to the problem and for many useful discussions. Prof. Charles Michel, Department of Bioengineering, Imperial College London also provided many significant suggestions.

## References

- [1] A. Bonfiglio, K. Leungchavaphongse, R. Repetto & J. H. Siggers. Mathematical Modeling of the circulation in the liver lobule. *ASME J. Biomech. Eng.* **132**, 111011 (2010)
- [2] R. A. Polin, W. W. Fox & S. H. Abman. *Fetal and neonatal physiology*, Saunders PA (2004)
- [3] T. Ricken, U. Dahmen & O. Dirsch. A biphasic model for sinusoidal liver perfusion remodeling after outflow obstruction. *Biomech. Model. Mechanobiol.* **9**(4), 435–450 (2010)
- [4] F. J. Walburn, & D. J. Schneck. A Constitutive Equation for Whole Human Blood, *Biorheology*, **133**, pp. 201210 (1976)

## MATHEMATICAL MODEL OF BLOOD AND INTERSTITIAL FLUID FLOW IN THE LIVER

Kritsada Leungchavaphongse<sup>1</sup>, Jennifer Siggers<sup>1</sup> & Rodolfo Repetto<sup>2</sup>

<sup>1</sup> *Department of Bioengineering, Imperial College London, London SW7 2AZ, UK*

<sup>2</sup> *Department of Civil, Environmental and Architectural Engineering, University of Genoa, Via Montallegro 1, 16145 Genoa, Italy*

### INTRODUCTION

The flow of blood and interstitial fluid in the human liver is highly specialised. The liver is supplied by two main vessels: the portal vein and the hepatic artery, which branch repeatedly over many generations to supply the lobules, the functional units of the liver. Lobules are approximately prism-shaped with a hexagonal cross-section. Portal tracts run along the parallel edges and contain three vessels: a branch of the hepatic portal vein, a branch of the hepatic artery, and a bile duct. A centrilobular vein runs along the axis of the prism. Blood is distributed in the lobule through a network of small fenestrated vessels called sinusoids. The majority of blood leaves the lobule via the centrilobular vein and passes into the network of veins, which join at successive bifurcations, ending in the hepatic veins, which drain into the inferior vena cava. However, some plasma in the sinusoids leaks through the wall fenestrations into the interstitial space. There are two outflow pathways for the interstitial fluid: direct and active uptake by the lymphatic ducts, which are situated at regular intervals throughout the lobules, and a slow flow across the liver and eventually out into the peritoneal cavity. Since the lower surface of the liver is covered by Glisson's capsule, the latter outflow pathway only occurs across the open upper surface. The volume flux of the interstitial fluid is much smaller than blood flux. However, during conditions of high blood pressure the flow can be significant [1], and hypertension in the liver often occurs after a partial resection or a split-liver transplant.

There is a relatively small amount of modelling work in this area, especially on the scale of the microcirculation. Studies include that by Ricken *et al.* [4], in which a poroelastic model was developed to study the remodelling of blood vessels that occurs after damage to the liver, and the model by Bonfiglio *et al.* [2], who also developed a poroelastic model, and used it to study the flux through the liver under conditions of high pressure. In this study, we develop a new model to investigate lymph flow using a multiscale model that accounts for variations both on the scale of a single lobule and variations on the scale of the whole liver.

### MATHEMATICAL MODEL

We denote the pressures in the sinusoids and in the interstitial space as  $p_s$  and  $p_i$ , respectively. Both blood and interstitial fluid flow in a very complicated network of interconnected channels that cannot be modelled individually even on the scale of a single lobule. Therefore, we assume that the flows of both fluids are governed by the Darcy equation, and treat both the sinusoidal space and the interstitium as a rigid and isotropic porous medium. Therefore, flow is governed by the equations

$$\mathbf{v}_s = -\frac{k_s}{\mu_s} \nabla p_s, \quad \mathbf{v}_i = -\frac{k_i}{\mu_i} \nabla p_i, \quad (1)$$

where the subscripts 's' and 'i' refer to the sinusoids and interstitium, respectively,  $\mathbf{v}$  is the Darcy flux,  $k$  the permeability of the porous medium and  $\mu$  the dynamic viscosity. Fluid is assumed to leak from the sinusoids to the interstitial space at a rate  $Q_w$  per unit volume, which is proportional to the pressure difference  $p_s - p_i$ . Furthermore, the lymph is assumed to be actively removed from the interstitial space through lymph vessels, at a rate  $Q_L$  dependent on the pressure in the interstitium. For simplicity, we assume  $Q_L = \alpha + \beta p_i$ , where  $\alpha$  and  $\beta$  are constants [3]. Thus mass conservation implies

$$\nabla \cdot \mathbf{v}_s + Q_w = 0, \quad \nabla \cdot \mathbf{v}_i - Q_w + Q_L = 0. \quad (2)$$

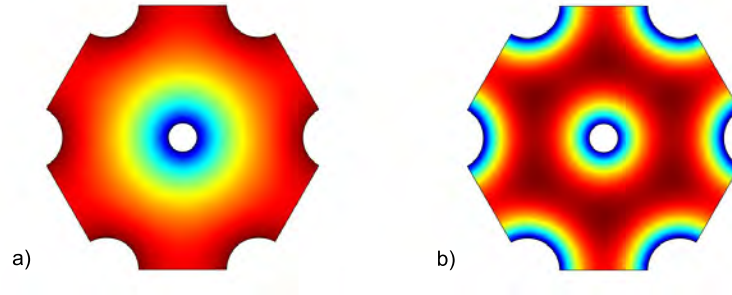


**Figure 1.** Spatial distribution of (a)  $p_{s0}$  and (b)  $p_{i0}$  in a single lobule. Each figure is scaled individually from high pressure (red) to low pressure (blue).

At the portal tracts and the centrilobular veins we prescribe the flux of blood. We assume that there is no blood flow across the boundary since sinusoids do not connect lobules to one another, which implies  $\partial p_s / \partial n = 0$  along the sides of the lobules. Finally, we assume that both the interstitial pressure  $p_i$  and its normal derivative  $\partial p_i / \partial n$  are continuous across the lobule sides. We also wish to impose conditions at the boundary of the whole liver. The outer wall of the liver is separated into two distinct regions: the lower part that is covered by Glisson's capsule, and the upper part that is permeable to the peritoneal cavity. No interstitial fluid may cross the lower boundary, but fluid is assumed to cross the upper boundary at a rate that we assume proportional to the pressure difference between the interstitial space and the peritoneal cavity. Therefore, we impose

$$\frac{\partial p_i}{\partial n} = A(p_i - p_{\text{ext}}) \text{ on the upper surface, } \frac{\partial p_i}{\partial n} = 0 \text{ on the other surfaces,} \quad (3)$$

where  $p_{\text{ext}}$  is the peritoneal pressure, which is prescribed. Finally, we assume there is no blood flux anywhere from the liver surface, giving  $\partial p_s / \partial n = 0$  on the whole surface.

To solve the problem we adopt the following decomposition

$$p_s = p_{s0} + p_{s1}, \quad p_i = p_{i0} + p_{i1}, \quad (4)$$

where  $p_{s0}$  and  $p_{i0}$  represent the solution of the problem in an infinite lattice of lobules without net flux of lymph through each lobule. The distribution of  $p_{s0}$  and  $p_{i0}$  within a single lobule is obtained numerically and is shown in figure 1.

In order to determine the flux of lymph through the whole liver we work in terms of spatially averaged quantities (averaged over an arbitrary template surface with size comparable or larger than the area of the lobule). This allows us to disregard the boundary conditions between lobules and solve the problem in the whole liver.

The authors thank Prof. Charles Michel, Department of Bioengineering, Imperial College London for many useful suggestions on the model.

## References

- [1] V.Arroyo Pathophysiology, diagnosis, and treatment of ascites in cirrhosis *Ann. Hepatol.* **1**(2), 72–9 (2002)
- [2] A. Bonfiglio, K. Leungchavaphongse, R. Repetto & J. H. Siggers. Mathematical Modeling of the circulation in the liver lobule. *ASME J. Biomech. Eng.* **132**, 111011 (2010)
- [3] J. R. Elk, R. E. Drake, J. P. Williams, J. C. Gabel & G. A. Laine. Lymphatic function in the liver after hepatic venous pressure elevation. *Am. J. Physiol.* **254**, G748–52 (1988)
- [4] T. Ricken, U. Dahmen & O. Dirsch. A biphasic model for sinusoidal liver perfusion remodeling after outflow obstruction. *Biomech. Model. Mechanobiol.* **9**(4), 435–450 (2010)

# Index

- Barthès-Biesel, D., **29**  
Belardi, J., 51  
Bianchi, E., **33**  
Blake, J. R., 43, 47  
Bonfiglio, A., 75  
Borer, D., **67**  
Boschetti, F., 33  
Boselli, F., **63**  
Brandt, L., **39**, 41  
Buck, A., 21  
Böhnke, F., **59**
- Chernyavsky, I. L., 27  
Chu, T.-X., 29  
Coupier, G., **23**
- Delfos, R., 57  
Doyeux, V., 23  
Dryden, I. L., 27  
Dubini, G., 33  
Dupire, J., 11
- Edom, E., **61**
- Fonta, C., 25
- Gadêlha, H., 45  
Gaffney, E. A., 45  
Guibert, R., **25**
- Hierck, B. P., 37  
Hill, A. A., 27  
Hu, X., 29  
Hussong, J., **51**
- Ismail, M., 23
- Jenny, P., 21  
Jensen, O. E., **27**  
Johnson, T. D., **43**, 47
- Kirkman-Brown, J., 45  
Kleiser, L., 61, 63  
Kloosterman, A., **37**  
Klöppel, T., **31**  
Krooneman, J., 57  
Kurtcuoglu, V., 35
- Köster, D., 59
- Lambert, R. A., **41**  
Lauga, E., **15**, 39  
Leach, L., 27  
Leguy, C. A. D., **57**  
Leunchavaphongse, K., 75, **77**  
Loghin, D., 43  
Lukes, V., 19
- Meskauskas, J., **65**  
Mestel, J., 53  
Muradoglu, M., 69, **71**
- Nelson, B. J., **16**, 49
- Obrist, D., 21, 61, 63  
Olgac, U., **69**, 71
- Parker, K. H., 53, 55  
Payvandi, S., **55**  
Peponas, S., 23  
Peyer, K. E., **49**  
Plouraboué, F., 25  
Podgorski, T., 23  
Poelma, C., 37, 57  
Poulikakos, D., 35  
Pourquie, M. J. B. M., 57  
Prucker, O., 51
- Reichold, J., **21**  
Repetto, R., 65, 75, 77  
Rohan, E., **19**  
Roose, T., **73**  
Rösgen, T., 67  
Rühe, J., 51
- Salsac, A.-V., 29  
Schorr, N., 51  
Secomb, T. W., **9**  
Setchi, A., **53**  
Siggers, J., 53, 55, 65, **75**, 77  
Smith, A. A., **47**  
Smith, D. J., 43, **45**, 47  
Socol, M., 11  
Swartz, M., **17**, 73

---

van Loon, J. J. W. A., 57  
Viallat, A., **11**  
Vreeburg, J., 57

Wall, W. A A., 31  
Wan Abdullah, W. R., 27  
Weber, B., 21  
Westerweel, J., 37, 51, 57  
Wiedemair, W., **35**

Zhang, L., 49  
Zhu, L., 39